

Computational Modeling of the Lumbar Spine: Active Musculature and Intra-abdominal
Pressure in Compressive Loading

by

Courtney Aileen Cox

Department of Biomedical Engineering
Duke University

Date: _____

Approved:

Cameron Bass, Advisor

Barry Myers

Roger Nightingale

Frank Pintar

Sergio Mendoza-Lattes

Dissertation submitted in partial fulfillment of
the requirements for the degree of Doctor
of Philosophy in the Department of
Biomedical Engineering in the Graduate School
of Duke University

2020

ABSTRACT

Computational Modeling of the Lumbar Spine: Active Musculature and Intra-abdominal Pressure in Compressive Loading

by

Courtney Aileen Cox

Department of Biomedical Engineering
Duke University

Date: _____

Approved:

Cameron Bass, Advisor

Barry Myers

Roger Nightingale

Frank Pintar

Sergio Mendoza-Lattes

An abstract of a dissertation submitted in partial fulfillment of the requirements for the degree of Doctor of Philosophy in the Department of Biomedical Engineering in the Graduate School of Duke University

2020

Copyright by
Courtney Aileen Cox
2020

Abstract

A current area of interest in lumbar injury is vertical impact loading. This includes effects of underbody blast (UBB), high speed planing boat impacts, and helicopter crashes. Lumbar spine fractures occur in 18% of all wounded in action injuries and 26% of soldiers killed in action exposed to UBB. Further, the US military has moving towards including women in all combat roles, including as the Special Forces beginning in January 2016. Volunteer and cadaveric data exist which suggest that male and female injury risk is not the same for equal stresses or loads. Dynamic injury mechanisms and thresholds have been extensively studied in the cervical spine, but not for the lumbar spine. While many lumbar models are available, no previously developed model is appropriate for high-rate vertical impact loading with intra-abdominal pressure and active musculature. So, the primary objective of this dissertation was to create a biofidelic hybrid multibody/finite element model to compare male and female response and assess the importance of active musculature and intra-abdominal pressure during single accelerative loading impacts (3-15g).

A 50th percentile male model was created using data from literature, experimental data, and medical imaging data. Scaling relationships for the 50th and 85th percentile female were derived, and an 85th percentile female model developed. The 85th percentile female model is mass-matched to the 50th percentile male model. An 11%

increase in ischium breadth in the 85th female changes the line of action for muscles inserting on the pelvis. These changes resulted in a female model having increased axial loads over a male model when matched for mass.

The 50th percentile male osteoligamentous model was validated against developed strain energy-force corridors and T12/L1 injury risk functions. A 50th percentile risk of spinal fracture of 5237 N was reported. During failure loading (as seen from experimental tests), the osteoligamentous spine model predicts a 41% risk of failure. While the model slightly underpredicts the risk of injury, the peak compressive load in T12/L1 lies within the 95th percentile confidence intervals for the 50th percentile risk of injury.

In this dissertation, it was hypothesized that men and women do not have the same risk of injury on an effective stress basis. This hypothesis was supported by comparing mass-matched male and female hybrid multibody/finite element models during an underbody blast loading condition. Based on the comparison between the 85th percentile female model to the 50th percentile male model predicts higher axial loads due to changes in musculature. It was also hypothesized that the use of active musculature decreases injury tolerance in compressive loading. This hypothesis was supported by comparing model intervertebral axial loads to both experimental (underbody blast) and epidemiological (electroconvulsive therapy) loading conditions. This research demonstrates higher muscle activations increase risk of lumbar spine injury in vertical

impact loading. A tensed activation state contributes 48 percent of the compressive load estimated to fracture the lumbar spine during underbody blast. While this corresponds to a low risk of injury (<10%), this could exacerbate risk of injury during additional compressive loading.

By better understanding the female lumbar spine response, new safety measures can be developed. This work could inform the design of new protective personal equipment, or guide permissible exposure limits and risk of injury.

Dedication

For my sisters, Alex and Mackenzie Cox. They show me daily that strength comes in many forms and remind me to value strengths other than that of the lumbar spine. I hope they will one day realize how they are strong, inspiring, wonderful, loving women in their own rights.

Contents

Abstract	iv
List of Tables	xii
List of Figures	xiii
Acknowledgements	xvii
1 Introduction	1
1.1 Lumbar spine injury in men and women	1
1.2 Anatomy	2
1.2.1 Osteoligamentous lumbar spine	3
1.2.2 Musculature	3
1.2.3 Torso mass	4
1.2.4 Intra-abdominal pressure	5
1.3 Predicting injury	6
1.4 Existing lumbar spine models	7
1.4.1 Commercially available models	8
1.4.2 Finite element models	9
1.4.3 Multibody models	11
2 Multibody model creation	15
2.1 Model geometry development	16
2.1.1 Image acquisition	16
2.1.2 Image segmentation and vertebral property determination	18

2.1.3 Male model mesh generation	22
2.2 Osteoligamentous spine	24
2.2.1 Torso.....	24
2.2.2 Vertebrae.....	25
2.3 Joints.....	26
2.4 Muscles	29
2.5 Intra-abdominal pressure.....	33
2.6 Development of a mass-matched female model.....	35
2.7 Conclusions	39
2.8 Limitations.....	39
3 Active musculature optimizations against gravitational loading.....	41
3.1 Introduction.....	41
3.2 Methods	43
3.2.1 Optimization details.....	43
3.2.2 Underbody blast failure tests and injury risk curve development.....	46
3.3 Results	47
3.4 Discussion and Limitations.....	55
3.5 Conclusion.....	56
4 Sensitivity analysis of the male model.....	58
4.1 Introduction.....	58
4.2 Methods	58
4.2.1 Sensitivity analysis methods.....	58

4.2.2 Model simulation methods	62
4.3 Results	63
4.4 Discussion and limitations	68
4.5 Conclusions	69
5 Computational modeling of underbody blast	71
5.1 Introduction.....	71
5.2 Methods	73
5.2.1 Experimental data collection	73
5.2.2 Osteoligamentous model validation and active musculature simulations.....	73
5.3 Results	79
5.3.1 Validation	79
5.3.2 Muscle activations and sex comparisons	87
5.4 Discussion and limitations	89
5.5 Conclusions	91
6 Sex Effects and injury risk for muscle tetanus	93
6.1 Spinal injury risk from muscle tetanus.....	93
6.2 Scaling men and women for date of study	96
6.3 Muscle and spinal characteristics.....	99
6.4 Weibayes analysis.....	104
6.5 Conclusions	107
6.6 Limitations.....	108
7 Conclusions and contributions to science	109

References 113

Biography 128

List of Tables

Table 1 Segmental and upper torso body masses from NASA STD 3001.....	5
Table 2 Segment mass as percentage of whole body mass and center of mass location as a percentage of segment length for men and women (adapted from [21])	5
Table 3. Finite element models' material properties (from Driescharf 2014)	11
Table 4 Basic information of current multibody and finite element models.....	13
Table 5. Musculoskeletal model properties.....	15
Table 6. Inertial properties of the male lumbar spine, determined via segmentation of MRI and CT scans.	22
Table 7. Passive muscle properties from Hedenstierna and Halldin 2008 for *MAT_OGDEN_RUBBER LS-DYNA material card.	33
Table 8. Scale factors for 85th percentile female and 50th percentile female with respect to 50th percentile male dimensions.....	38
Table 9. Active lumbar muscles relaxed optimized activation levels.....	48
Table 10. Active lumbar muscles tensed optimized activation levels	50
Table 11. Sensitivity analysis variables and input ranges by category.	61
Table 12. Studies of spinal fracture from convulsive therapy and grand mal epileptic seizures.	94
Table 13. Demographic characteristics of mid-size female and males in 1939 and 2014	102
Table 14. Breakdown of thoracic and lumbar injuries by sex.....	106
Table 15. Weibull coefficients for the statistical models by sex and year.	106

List of Figures

Figure 1. Segmentation of vertebral bodies and individual muscles in an MRI slice (left) and CT slice (right).	18
Figure 2. Full segmentation of lumbar spine, sacrum, and pelvis before 2D mesh generation in Avizo.	19
Figure 3. Front and side view of segmented bony and muscular anatomy.	20
Figure 4. Sagittal cross-section of the L5 vertebral body including both cortical shell mesh (pink), and solid trabecular mesh (purple) for vertebra inertia calculations.	21
Figure 5. Side view (left), front view (center), and top view (right) of the solid mesh constructed from segmentation of abdominal CT scan.	23
Figure 6. Lumbar model with upper torso mass indicated.	25
Figure 7. Compressive joint stiffness properties from Brinckmann (1988) for male and female segments less than 50 years of age.	26
Figure 8. Calibrated compression (positive) and tension (negative) axial stiffness curves for the lumbar model.	28
Figure 9. Lumbar spine bending response adapted from Adams 1980, 1991, and 1994.	29
Figure 10. Developed lumbar spine model including anatomically correct muscle attachments.	31
Figure 11. Abdominal volume solid mesh	34
Figure 12. Injury risk curve for fracture force at T12/L1 from UBB failure tests (Bass, unpublished data)	47
Figure 13. Relaxed muscle activations indicate slight contraction of the extensor muscles to maintain an upright torso.	48
Figure 14. Sensitivity of the posterior torso CG displacement to relaxed muscle activations.	49

Figure 15 Tensed muscle activations for 11 different muscles all exceed 70 percent activation, and there is co-contraction of flexors and extensors	50
Figure 16. Optimization history for the maximum compressive force in Newtons in T12/L1 joint	51
Figure 17. Sensitivity of the posterior torso CG displacement to tensed muscle activations	52
Figure 18. Percent increase in intra-abdominal pressure by joint level over the 30 ms of tensed muscle activation.	54
Figure 19. Box and whisker plot of intra-abdominal pressure after tensed activation state. Whiskers represent the 25 th and 75 th percentile, and the central red dash marks the median. Intra-abdominal pressure does not differ by joint level.....	54
Figure 20. Model transverse cut planes at joint centers of rotation. Left- T12L1, middle- L4L5, right- L5S1. Solid elements in full color, with shell parts outlined.....	55
Figure 21. Experimental axial displacement for subfailure test (Duke, unpublished data)	63
Figure 22. Coefficients of correlation for intra-abdominal pressure at the T12/L1 joint level with 95% confidence intervals in red.....	64
Figure 23. Coefficients of correlation for intra-abdominal pressure at the L5/S1 joint level with 95% confidence intervals in red	65
Figure 24. Peak spinal compressive force has a stronger correlation with peak intra-abdominal pressure at more superior joint levels.	66
Figure 25. Spine axial (left), bending (middle), and shear (right) stiffness scale factors were of the parameters having the greatest overall effect	67
Figure 26. Experimental axial displacement for subfailure test (Duke, unpublished data) (left), and experimental setup (right).	74
Figure 27. T12/L1 axial force corridor for 200 N/ms underbody blast loading (Duke, unpublished data).	75
Figure 28. Strain energy as a function of force for 29 cadaveric lumbar failure tests.....	76

Figure 29. Compression energy with respect to force	77
Figure 30. Injury risk curve for 50th percentile male, 50th percentile female, and 85th percentile female.	78
Figure 31. Compressive forces in the lumbar spine for an approximately 3 mm sacral impact	80
Figure 32. Axial force displacement curves of the intervertebral joints during subfailure underbody blast.	81
Figure 33. Model simulation strain energy response compared to experimental corridors shows the lumbar model can be used for modeling failure	82
Figure 34. Underbody blast failure simulation axial compressive force by joint level.	83
Figure 35. There is a phase lag between the shear responses of the intervertebral joints.	84
Figure 36. Bending moments at the joints' CORs for the lumbar spine are small during vertical impact.	85
Figure 37. Experimental underbody blast moment response.....	86
Figure 38. Full lumbar model with active muscles decrease the axial compressive load of the lumbar spine.....	87
Figure 39. Tensed activations (dashed) result in substantially higher axial forces in the lumbar spine compared to tensed (solid) activations.	88
Figure 40. Comparison of male (solid) and female (dashed) models of matched mass and including active musculature.	89
Figure 41. Percentage spinal fractures in patients.....	95
Figure 42. Location of spinal fractures by region in patients.....	96
Figure 43. Stature of 18-year-old men and women by age from 1939-2014.....	98
Figure 44. Body mass of 18-year-old men and women by age from 1940-2010	99
Figure 45. Percentage change in PCSA and vertebral body cross sectional area (VBCSA) by year in young men.....	103

Figure 46. Percentage change in PCSA and vertebral body cross sectional area (VBCSA) by year in young women.	104
Figure 47. Ratio of VBSA/VBCSA for men and women compared with relative risk from thoracic spinal fractures scaled to 1945 values.	107

Acknowledgements

Innumerable people have helped me with this science and also surviving it. I appreciate them all. While my name is listed as the author of this dissertation, it would not have been possible without the love and support of so many others. In no way did I complete this dissertation alone. It was a labor of love from many individuals, and I will not be able to thank them all properly. Both within the scientific community and without, all of those mentioned here have contributed significantly during my journey during graduate school.

My parents, Buddy and Denise Cox, have given constant love and support. They have always believed in me, and encouraged me to believe in myself. I would not have the stubbornness, enthusiasm, or motivation needed to get through graduate school without them.

My sisters, Alex and Mackenzie Cox, have also been great pillars of support during my time in graduate school. They consistently support me following my own path, even though it is sometimes very different from theirs.

Dr. Cameron Bass has been the biggest supporter of my research since I arrived at Duke. He challenges me to discover my own scientific interests, and encourages me to gain experience in many different aspects of research. Because of his guidance, I have gained experience in experimental and computational research in areas from automotive head and neck injuries to lumbar spine blast injuries included in this dissertation. His

never-ending enthusiasm for biomechanics constantly encourages my own love of science and engineering.

The rest of my committee: Dr. Barry Myers, Dr. Frank Pintar, Dr. Sergio Mendoza-Lattes, and Dr. Roger Nightingale have encouraged me to think about research from various viewpoints. I constantly consider the importance of my research and why I am making the decisions I make due to their influence. They have influenced how I ponder the importance of methodology, clinical significance, “real world” motivation, and alternative ways to investigate the same research topic.

Brian Bigler has been the primary graduate student to support me on this journey. Even after our projects split paths, he was always available for moral support or scientific discussions. Thank you for sharing my interest in modeling, and understanding the necessity of rubber duck debugging.

Concetta Morino was brought into this project very late in my dissertation, but has made significant contributions to my efforts here. She was involved in my efforts to develop a female model, and with muscle tetanus research. Thank you for your patience and willingness to work with a frantic PhD candidate nearing graduation.

While this dissertation focuses on computational modeling, experimental efforts were also necessary. I must thank my teammates that assisted and led experimental efforts. Thank you to my experimental teammates, including Allison Schmidt, Jay Shridharani, Maria Ortiz-Paparoni, and Brian Bigler and Jason Kait.

Baowei Jiang, thanks for all your time with the imaging study included in this dissertation. I am grateful to have had the opportunity to mentor you.

Rachel Lance is a wonderful friend, scientist, and human being. I am so grateful for her support these last few years. From helping with literature searches to dog sitting, she is always willing to reach out and help in whatever way she can. I am very thankful for her presence in my life, and her support in finishing this dissertation.

To my Durham dance community, including Heather Atkins, Chelsea Fizer, Jose Velasquez, Nicki Miller, Zanetta Chang, Erika Vinson, Ay-Jaye Nelson and so many others: I do not think you will ever know how much of my success here belongs to you. Thank you for keeping me both grounded and moving. Thank you for helping me to grow as a dancer, and an individual, and to encourage me to be involved in my community. So many of you have invested your time in helping a quiet engineer become a more confident, expressive dancer and in turn, scientist.

I have been fortunate to share my time as a graduate student with many other bright individuals. To my other fellow graduate students in the Injury Biomechanics Lab, past and current: I am grateful for the many scientific conversations that take place over coffee or spontaneously in offices. Thank you for all your support, and willingness to assist with projects other than your own.

The Whitaker Foundation and the Royal British Legion Centre for Blast Injury Studies at Imperial College, including Dr. Spyros Masouros, afforded me my first

opportunity to investigate lumbar spine modeling, and to think about research outside my own lab. I am very grateful.

1 Introduction

The current study explored computational approaches suitable for modeling lumbar spine response and injury across gender, while also being applicable for high rate, vertical loading environments.

1.1 Lumbar spine injury in men and women

Many studies have shown sex-based differences in lumbar spine strength and injury risk. For example, the vertebral breaking strength is lower in females, unadjusted for stress [1 2]. A population-based epidemiologic research study of Rochester, NY indicated a higher incidence of vertebral fractures in women compared to men [3]. Also, women had more severe fractures following moderate trauma, while men had more fractures following severe trauma [3]. Brinckmann, et al. [4] found the compressive strength of function spinal units (FSUs) to be dependent on bone mineral density and endplate area.

While it is expected for female spines to break at lower loads due to size differences, there are likely other factors which contribute to differences in biomechanical response. Schmidt et al. found that even after accounting for loading area, females were still at higher risk of injury than males [5]. Based on this study, it should be concluded that female spines are not simply smaller male spines. Other anatomical differences such as mass distribution, muscle mass, muscle recruitment,

muscle insertion points and lines of action, and intra-abdominal volume between males and females likely contribute to injury risk.

While osteoligamentous studies of the lumbar spine yield information regarding vertebral body and vertebral disc failure [6], they do not contain active musculature which contributes additional loads and moments on the spinal column [7]. This makes determination of *in vivo* injury risk difficult to obtain. Since experimental studies of injurious loading of the *in vivo* human lumbar spine are for obvious reasons not achievable, researchers turn to computational models. These models can be tested in a range of loading scenarios and muscle activations to determine injury risk and produce biofidelic kinematics [8]. Such models have regularly been applied for the cervical spine and demonstrate the necessity of including active musculature [9].

1.2 Anatomy

In order to develop a lumbar spine model, it is critical that the correct anatomical features are represented. While a complete description of the lumbar anatomy is beyond the scope of this work, the salient features are summarized here, including the osteoligamentous lumbar spine, relevant musculature, the upper torso mass, and intra-abdominal pressure. Where appropriate, differences between males and females are described.

1.2.1 Osteoligamentous lumbar spine

The lumbar spine has five vertebral bodies and is bounded by the thoracic spine superiorly, and the sacral spine inferiorly. In adults the natural posture is lordotic, with a posterior center of curvature. The lumbar vertebrae are joined by intervertebral discs, composed of an annulus fibrosis and nucleus pulposus. The disc provides range of motion and represents the primary kinematic degrees of freedom for the osteoligamentous lumbar spine. The disc is often assumed to be incompressible [10] and viscoelastic [11] or poroelastic [12] to incorporate rate-dependent effects. Other structures connecting the vertebrae include ligaments such as the anterior longitudinal ligament, posterior longitudinal ligament, ligamenta flava, supraspinous ligament, and joint capsules at the facets.

When accounting for geometric differences between sexes, female spines do not scale the same in all three axes when compared to male spines. For example, the cross sectional area of female vertebral bodies is 25% smaller than the male area when matched for vertebral body height [13]. Male vertebral body dimensions are larger than female dimensions when matched for age, stature, and mass [13].

1.2.2 Musculature

The musculature surrounding the lumbar spine aids in support of the spinal column and upper torso mass. Muscles that contribute to lumbar spine kinetics and kinematics include the abdominal wall muscles (i.e. quadratus lumborum, rectus

abdominis, external and internal oblique) and the erector spinae muscles on the dorsal spine (i.e. longissimus, iliocostalis, and multifidus). Muscle cross-sectional area differs between males and females (e.g. [14]). In addition to size differences, the relative proportion of muscle mass to segmental mass differs by sex. For males, upper body muscle mass relative to body mass is 42.9%, while for females, upper body muscle mass is 39.7% [15].

Active musculature may play a role in sex-based differences in lumbar injury risk. Dewald et al. and Easton and Sommers demonstrated compression fractures in the spine as a complication of convulsive seizures due to electroconvulsive therapy, and showed the incidence of female spines fractures was significantly less than the incidence of fractures in male spines [16 17]. This is hypothesized to be due to larger muscle mass in the males, as well as different lines of action for muscle loading. Compressive fractures in the vertebral bodies were found in thoracic spine, most commonly in the fourth through sixth vertebrae [16].

1.2.3 Torso mass

The torso mass influences the inertial response of the lumbar spine [18]. The body mass distribution is different between males and females., and this difference is larger in the upper body than the lower body [15]. Janssen et al. compared healthy adult men (n=268) to women (n=200), with ages from 18-88 years. Both skeletal mass and muscular mass were determined from MRI. McConville et al. reports segmental body

masses from 31 male subjects [19], and is the basis for the NASA Standard 3001, which details human needs for space flight. Segmental body masses for the American Male Crewmember are given in Table 1.

Table 1 Segmental and upper torso body masses from NASA STD 3001

Segment	5th percentile (kg)	50th percentile (kg)	95th percentile (kg)
Head	4.260	4.40	4.550
Neck	0.930	1.100	1.270
Thorax	20.420	26.110	31.760
Summed upper torso mass	25.61	31.61	37.58

The upper torso mass for females can be scaled from male data using body weight and stature. Segmental body mass percentages and center of mass locations are given in Table 2.

Table 2 Segment mass as percentage of whole body mass and center of mass location as a percentage of segment length for men and women (adapted from [21])

Segment	Mass (%)		Longitudinal CM Location (%)	
	Female	Male	Female	Male
Head	6.68	6.94	58.94	59.76
Upper torso	15.45	15.96	20.77	29.99
Middle torso	14.65	16.33	45.12	45.02

1.2.4 Intra-abdominal pressure

Increased muscle activations cause an increase in muscle forces, and therefore increased intra-abdominal pressure. Grenier and McGill investigated different abdominal muscle activation strategies computationally and found that they cause

changes in spine stability and pre-compression [22]. Thus, an intra-abdominal pressure component should be included in a computational model that contains active musculature, but has not been developed to date. Mean intra-abdominal pressure ranges from 0.027-2.16 kPa, with a mean of 867 Pa when sexes are combined [23]. This same study did not determine intra-abdominal pressure to be significantly different between males and females.

1.3 Predicting injury

Schmidt et al. recently updated the ISO 2631-5 criterion [5], which predicts bodily injury due to repeated loading, including the lumbar spine. The ISO 2631-5 criterion, R , is calculated based on maximum stress in a cycle, number of cycles, ultimate strength, and static stress. It informs the injury risk due to repeated exposure to mechanical shocks. The modified R value provides probability of failure for both males and females.

The Federal Aviation Administration Standard 14 CFR Part 25 Subpart 562 for aircraft airworthiness standards includes occupant safety testing in emergency landing dynamic conditions. For a minimum acceleration of 14 g's in less than 80 ms, with a change in velocity (Δv) of at least 10.7 m/s, the peak compressive load measured at the junction of the pelvis and the lumbar spine cannot exceed 6672 N in a 50th percentile male anthropomorphic test device (ATD) meeting 49 CFR part 572 Subpart B.

One injury criterion used in the cervical spine is the N_{ij} criterion. Designed for use with the Hybrid III, N_{ij} is used to predict severe injury (AIS 3+) and is based on simple beam theory concepts. Injury is predicted based on a combination of axial force and sagittal bending moment.

$$N_{ij} = \frac{F_z}{F_{z_{crit}}} + \frac{M_y}{M_{y_{crit}}}$$

N_{ij} does not predict injury based on stress, but has different critical values for a 50th percentile male and 5th percentile female. For the Hybrid III 50th percentile male, the compression critical value is 6806 N (FMVSS 208). For the 5th percentile female, this critical value is 3880 N. Thus, an injury will occur at lower loads for the 5th female compared to the 50th male.

1.4 Existing lumbar spine models

A search of existing lumbar models was performed to assess their validity and applicability for the current study. This search had two primary objectives. The first was to determine if there were any commercially available models that were presently viable or that could be minimally modified. The second was to explore if any other research groups had already created a model for this purpose. If potentially viable models exist, were appropriate parameters used to create the target model, and was validation performed across a range of applicable loading conditions? Both finite element and multibody dynamic models were investigated. Candidate models were then restricted to multibody models, as the simplified construction has significant advantages in terms of

computational cost for dynamic loading conditions, where kinematics are of particular importance.

A total of 15 lumbar or whole body models containing a lumbar spine were found. Models are listed in Table 4, and indicate five potential multibody models. In addition, out of all 15 models, only the MADYMo model provided any vertical impact validation. Most models are used for quasistatic applications, with the remainder used for automotive applications.

1.4.1 Commercially available models

Models that are commercially available include the GHBMC, THUMS, MADYMo, and LifeMod/ADAMS models. GHBMC and THUMS are finite element models, while MADYMO, LifeMod/ADAMS, and AnyBody Modeling Systems are multibody models. GHBMC, THUMS, and MADYMo are used for automotive applications.

MADYMo presents the sources of its validation in a quality report [27]. For impact, a vertical sled test from volunteer experiments is used [28]. Peak sled acceleration is 6-10 g, which is lower than peaks seen by high speed planing watercrafts. However, this study may be used for model development or validation. MADYMo, as a numerical solver, implements multibody, finite element, and computational fluid dynamics methods. It can also be coupled with LS-DYNA.

The Global Human Body Model Consortium (GHBMC) is comprised of several automotive companies, with sponsors including the National Highway Traffic Safety Administration (NHTSA). As such, it is developed primarily for automotive applications, but states it is also for “real world injury conditions.” The whole body model, including the lumbar spine, is a finite element model with 2.2 M elements (M50 Occupant Version 4.4) [29].

The Total Human Model for Safety (THUMS) is developed by Toyota and LSTC. However, it “is limited to civilian use, and may under no circumstances be used in military applications [30].” Because of this restriction, THUMS was no longer investigated as a possible model.

LifeModeler’s human modeling software, LifeMod, can be integrated with other models. This includes MSC.Adams and LifeModeler’s LumbarSim. However, LifeMod does not give any information on data used to create and validate the model. Therefore, it is unclear for what applications it is useful. Similarly, another modeling software, AnyBody Modeling Systems, does not provide validation data or material properties. AnyBody does list aerospace and defense as modeling applications.

1.4.2 Finite element models

A total of nine finite element models were investigated. Eight of these were compiled and tested in a study of existing models by Dreischarf et al [31]. The material properties for these models are summarized in

Table 3. None of these were created for high rate loading, or vertical loading. In this study, all models were run in static loading, pure bending, and compression at low rates.

Table 3. Finite element models' material properties (from Driescharf 2014)

Component	Kim and Park	Puttlitz and Labus	Chen and Wang	Little and Adam	Schmidt and Wilke	Shirazi-Adl	Rohlmann and Zander	Goel and Kiapour
Cortical bone	E=12000 MPa v=0.3	E11=8000 MPa E22=8000 MPa E33=12000 MPa v1=0.4 v2=0.34 v3=0.3	E1=22000 MPa E2=11300 MPa v1=0.484 v2=0.203	E=11300 MPa v=0.2	E1=22000 MPa E2=11300 MPa v1=0.484 v2=0.203	Rigid	E=10000 MPa v=0.3	E=12000 MPa v=0.3
Cancellous bone	E=100 MPa v=0.2	Based on CT images	E1=200 MPa E2=140 MPa v1=0.45 v2=0.315	E=140 MPa v=0.2	E1=200 MPa E2=140 MPa v1=0.45 v2=0.315	Rigid	E1=200 MPa E2=140 MPa v1=0.45 v2=0.315	E=100 MPa v=0.2
Annulus bulk ground substance	Hyper-elastic Mooney-Rivlin c1=0.18 c2=0.045	Hyperelastic Yeoh c10=0.0146 c20=-0.0189 c30=0.041	Hyperelastic Mooney-Rivlin c1=0.42 c2=0.105	Hyper-elastic Mooney-Rivlin c1=0.7 c2=0.2	c1=0.56 c2=0.14	Linear hypo-elastic E=4.2 MPa v=0.45	Hyper-elastic Neo-Hookean c1=0.3448 c2=0.3	Hyper-elastic Neo-Hookean c1=0.3448 c2=0.3
Nucleus pulposus	Incomp fluid-filled cavity	E=1.0 MPa v=0.49	Incompressible fluid	Incomp fluid	Incomp fluid-filled cavity	Incomp fluid	Incomp fluid-filled cavity	Incom fluid

1.4.3 Multibody models

Among multibody models, MSC.ADAMS can be used separately from LifeMOD to model the human. For example, Abouhossein et al. used MSC.ADAMS to create a rigid body model of the lumbar spine [32]. They replaced the MSC.ADAMS material properties with material properties derived from studies such as Pintar, et al. [33] and de Jager [34]. This study investigated low frequency, low amplitude oscillations and static equilibrium.

In another study reported using a multibody model, Yoshimura et al. investigated seated human body exposure to vibration (4.3-13.9 Hz)[35]. This model is two-dimensional, and contains 10 degrees of freedom, eight in rotation and two in translation. The model proposed in this dissertation is a three-dimensional model, and will simulate loading rates with frequencies much higher than investigated in Yoshimura, et al. [35].

De Zee et al. used AnyBody modeling software [36]. While the details of the model are not presented (see commercial models section), this paper does include lumbar muscles. Validation is determined from comparing moments and range of motions through physiological ranges.

No models were found that were used for vertical impact loading and contained active musculature.

Table 4 Basic information of current multibody and finite element models

Model	Source	Type	Use
GHBMC		FE	Automotive, "real world injury conditions"
THUMS		FE	Automotive
MADYMO		Multibody	Automotive, vertical impact, intermediate impact directions, rollover
LifeMod/ADAMS		Multibody	
Kim/Park	Dreischarf 2014/Park 2013	FE	Static loading, pure bending, compression
Puttlitz/Labus	Dreischarf 2014 (but found model paper later)	FE	Static loading, pure bending, compression
Chen/Whang	Dreischarf 2014/Liu 2011	FE	Static loading, pure bending, compression
Little/Adam	Dreischarf 2014/Little 2008	FE	Static loading, pure bending, compression
Schmidt/Wilke	Dreischarf 2014/Schmidt 2012	FE	Static loading, pure bending, compression
Shirazi-Adl	Dreischarf 2014/Shirazi-Adl 1994	FE	Static loading, pure bending, compression
Rohlman/Zander	Dreischarf 2014/Rohlmann 2006	FE	Static loading, pure bending, compression
Goel/Kiapour	Dreischarf 2014/Kiapour 2012	FE	Static loading, pure bending, compression
Yoshimura	Yoshimura 2005	Multibody	Vibration (4.3-13.9 Hz)
Zee (generic detailed rigid-body)	Zee 2007	Text based, multibody	
Abouhossein	Abouhossein 2011	Multibody	equilibrium, 0.05 Hz w/ mag. Of 0-13 Nm in flexion and 0-15 Nm in extension

Based on the conducted search of the available academic and commercial computational models for lumbar kinematics and injury, none were deemed suitable for the present study. Therefore, this dissertation extended the current literature to incorporate high rate and vertical kinematic inputs. The developed model is validated against a number of physiologic scenarios, including electroshock, high rate compression, and torso stabilization against gravitational loading. It includes both active and passive musculature and a novel representation of the abdomen to account for physiologic inertia during these loading events.

2 Multibody model creation

A 50th percentile male lumbar multibody model was developed following the same general methodology as the Duke Adult Male Head/Neck Model (see [37 38]) and included both active musculature and the osteoligamentous spine. All model simulations were performed using the simulation software LS-DYNA (LSTC, Livermore, CA).

Where available, model properties were taken from literature. General musculoskeletal properties will remain the same as in the cervical model (Table 5). If other model parameters were needed that are not found in literature, they were scaled from the cervical model (e.g. shear stiffness found in the literature is not tested at sufficiently high rates for the current study [39]), or determined via medical imaging data (e.g. vertebral inertia).

Table 5. Musculoskeletal model properties

	Property	Source
Bone Density	2.0 g/cm ³	[40]
Cortical Bone Thickness	0.591 mm	[41]
Cortical Bone Porosity	13.8%	[42]
Trabecular Bone Porosity	87.2%	[43]
Muscle max isometric stress	0.50 MPa	[44]
Muscle activation state time constant	15 ms	[45]
Muscle deactivation state time constant	40 ms	[45]

2.1 Model geometry development

2.1.1 Image acquisition

In order to generate biofidelic anatomy for the proposed multibody models, an imaging study was proposed. Experience with cervical models suggests that muscle insertion locations and lines of action affect model response [46]. Comparable literature for the lumbar spine suitable for finite element model development does, to the author's knowledge, not exist. The purpose of this study is to quantify anthropometric properties of the muscular and osteoligamentous anatomy of the male and female lumbar spine. With accurate mechanical and geometric data of lumbar muscles, sex-specific computational models of the lumbar spine can be developed. As the computational models in this study are simulating seated loading conditions, MRI images from a seated MRI were preferred, but ultimately were not available. Instead, ten MRI or CT scans were obtained from supine subjects. These were bounded by the ANSUR II mean \pm 1 standard deviation (SD) for stature and mass. This is 176 +/- 7 cm for men and 162 +/- 6.5 cm for women [47]. Mass criteria was 78.5 kg +/- 11.1 kg for men and 62.01 kg +/- 8.35 kg for women [47]. The age inclusion criteria was 18-50 years old.

A retrospective review was performed with IRB approval of previously obtained acquisitions that included the lumbar spine in men and women of various stature and weight groups. These scans may have been obtained for a variety of purposes during clinical treatment of the patient. Scans with extreme pathology or abnormal findings

were omitted. A representative at Duke Department of Orthopaedic Surgery (the Data Collector) obtained the needed scans from the archives by starting at the present (time of IRB approval) and sequentially going backwards in time. All patient identifiers (name, medical record number, etc.) were removed when the analyses were performed except age and gender, which are necessary for proper data and response normalization. These scans were de-identified by the Duke Radiology Multi-D Lab.

This retrospective study resulted in 4 MRI and 6 abdominal CT scans being procured under the IRB with Duke University. Of these ten scans, three of the subjects were women and seven were men. One of the female scans was unusable for this project due to technical reasons, and a total of nine scans were segmented. MRIs provided greater spatial resolution, but did not capture the needed musculature. Abdominal CTs were more likely to be associated with an acute injury, but provided full visualization of abdominal musculature (Figure 1).

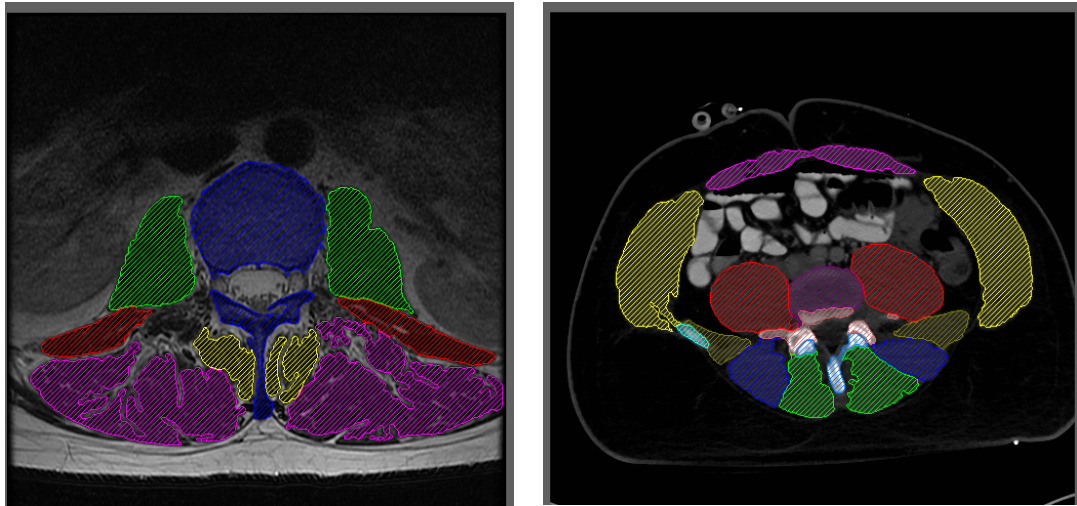


Figure 1. Segmentation of vertebral bodies and individual muscles in an MRI slice (left) and CT slice (right). CT scans allowed for full segmentation of musculature for lumbar modeling.

2.1.2 Image segmentation and vertebral property determination

In order to obtain accurate and biofidelic geometric estimates for the lumbar spine and surrounding musculature, voxel-based segmentation of the acquired medical images was performed. Muscles were segmented at the mid intervertebral disc from joint levels T9/T10 through L5/S1 as well as at their endpoints (Figure 2 and Figure 3).

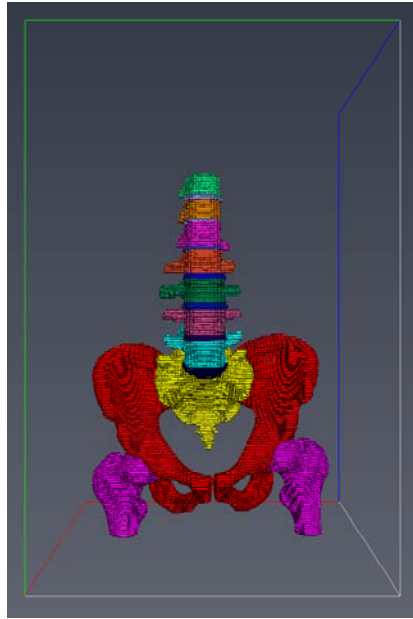


Figure 2. Full segmentation of lumbar spine, sacrum, and pelvis before 2D mesh generation in Avizo. Both vertebral bodies and intervertebral discs were fully segmented to ensure a continuous mesh.

Vertebral bodies and intervertebral discs were segmented along the length of the spine from T9 through the sacrum (Figure 3). Spinal muscles segmented were the multifidus, psoas, erector spinae, latissimus dorsi and quadratus lumborum. In addition, abdominal muscles segmented included the rectus abdominus, and the internal and external oblique. The obliques were segmented together as there was difficulty in distinguishing between the muscles during segmentation.

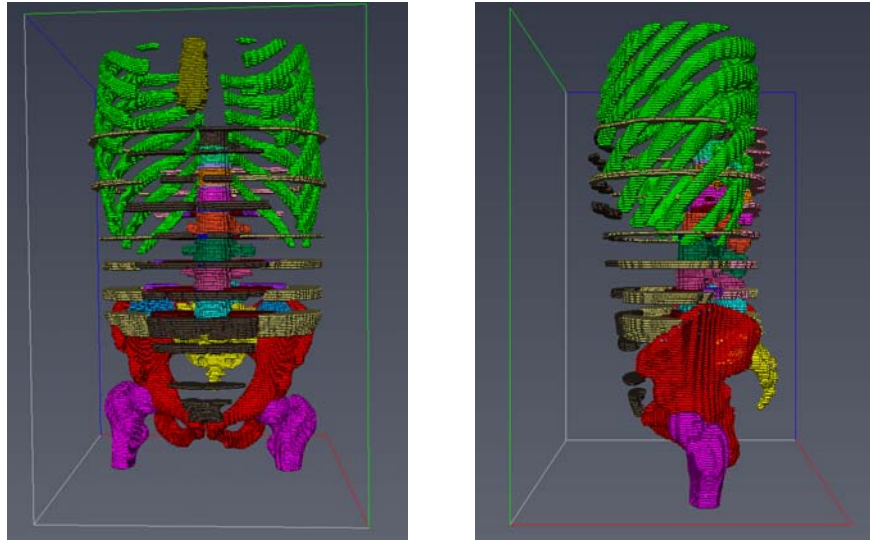


Figure 3. Front and side view of segmented bony and muscular anatomy. Muscles are segmented at the intervertebral discs, origins, and insertions. The obliques (in grey) were grouped together instead of modeling separately with poor boundaries.

Segmentation and 2D mesh generation was performed with Avizo. There were slight differences between segmentation methodology for the MRI and CT scans. The MRI scans required manual segmentation of vertebral bodies. However, CT scans provided a higher level of contrast for bones, and a masking tool was used to segment automatically as a first step. This was followed with manual segmentation to ensure proper boundaries, and to eliminate holes and islands within the mesh.

In order to convert voxel segmentation to usable finite element model constituents, LS-Prepost was used for 3D solid mesh generation from the shell surface meshes output from Avizo. The shell elements were used to model cortical bone, while the 3D solid mesh was used to model trabecular bone (Figure 4).

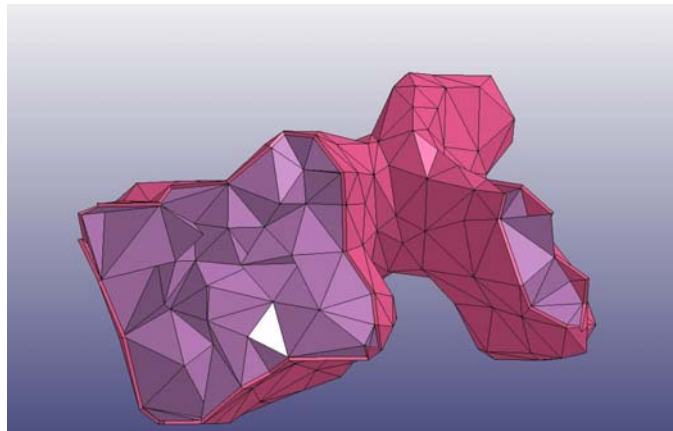


Figure 4. Sagittal cross-section of the L5 vertebral body including both cortical shell mesh (pink), and solid trabecular mesh (purple) for vertebra inertia calculations.

Combining the two parts resulted in better estimates for mass and inertial properties for vertebral bodies (Table 6) than using averaged properties. Both vertebral mass and inertia increase as the spine is traversed from superior to inferior ends. Inertial values are needed to properly define the *PART_INERTIA card chosen to model the rigid body vertebrae.

Table 6. Inertial properties of the male lumbar spine, determined via segmentation of MRI and CT scans.

Mean Values							
	lxx (kg m ²)	lxy (kg m ²)	lxz (kg m ²)	lyy (kg m ²)	lyz (kg m ²)	lzz (kg m ²)	mass (kg)
T11	2.97E-05	-1.98E-08	-2.62E-07	1.88E-05	2.83E-06	3.48E-05	5.31E-02
T12	4.25E-05	-5.45E-07	2.97E-07	3.11E-05	5.68E-06	4.83E-05	1.05E-01
L1	5.34E-05	-9.51E-07	1.79E-07	3.56E-05	7.97E-06	5.95E-05	1.15E-01
L2	6.50E-05	-1.85E-06	1.47E-07	4.04E-05	9.08E-06	7.19E-05	1.25E-01
L3	7.14E-05	-2.32E-06	3.27E-07	4.30E-05	8.30E-06	8.07E-05	1.30E-01
L4	7.14E-05	-1.72E-06	-1.13E-07	4.54E-05	5.32E-06	8.63E-05	1.35E-01
L5	6.07E-05	-1.46E-06	-1.32E-06	4.73E-05	-2.36E-06	7.95E-05	1.33E-01
Sacrum	6.53E-04	-5.24E-06	1.57E-07	6.81E-04	2.32E-04	7.15E-04	5.07E-01
Standard Deviation							
	lxx (kg m ²)	lxy (kg m ²)	lxz (kg m ²)	lyy (kg m ²)	lyz (kg m ²)	lzz (kg m ²)	mass (kg)
T11	2.44E-05	7.28E-08	2.74E-07	1.64E-05	1.44E-06	2.93E-05	5.62E-02
T12	1.69E-05	7.52E-07	4.77E-07	1.43E-05	1.69E-06	2.04E-05	3.18E-02
L1	2.17E-05	1.23E-06	9.60E-07	1.38E-05	2.68E-06	2.47E-05	3.17E-02
L2	2.52E-05	2.89E-06	9.56E-07	1.59E-05	3.30E-06	2.99E-05	3.33E-02
L3	2.53E-05	3.42E-06	1.86E-06	1.31E-05	3.99E-06	2.89E-05	2.69E-02
L4	2.72E-05	3.20E-06	1.99E-06	1.44E-05	4.46E-06	3.33E-05	3.16E-02
L5	2.24E-05	1.76E-06	1.95E-06	1.52E-05	6.19E-06	2.64E-05	3.10E-02
Sacrum	3.77E-04	1.14E-05	1.04E-05	3.38E-04	1.47E-04	3.57E-04	1.75E-01

2.1.3 Male model mesh generation

One of the male abdominal CT scans was selected to develop the finite element mesh for the 50th percentile male model. Linear interpolation was used to generate a continuous segmentation of muscles between the intervertebral discs from the previous segmentation step (Figure 3). In addition, the pelvic floor, pelvis, and diaphragm were segmented for boundary considerations. The resulting finite element mesh is shown in

Figure 5. The abdominal cavity is bounded superiorly by the diaphragm (brown), anteriorly by the abdominal muscles (green and yellow), inferiorly by the pelvis (red) and pelvic floor (orange), and posteriorly by spinal musculature and osteoligamentous spine.

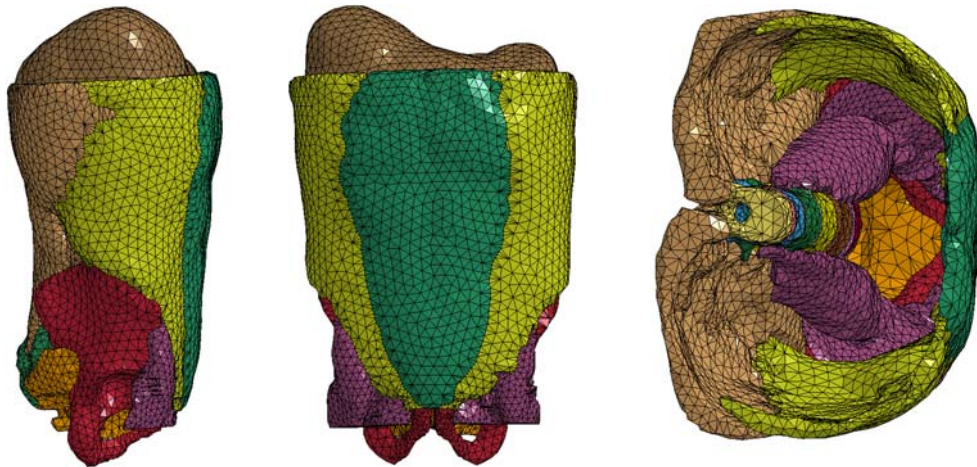


Figure 5. Side view (left), front view (center), and top view (right) of the solid mesh constructed from segmentation of abdominal CT scan. The top view has the diaphragm removed for a view of the interior of the model, as well as the mesh continuity.

Solid, three dimensional elements were generated from the segmentation surface meshes. While solid and surface meshes were used to generate inertial vertebral properties, only the surface mesh was necessary for rigid body modeling in the resulting multibody model. Similarly, the pelvis and sacrum were modeled as shell surfaces. The use of a surface mesh in Avizo allowed for a continuous mesh between all parts once imported into LS-Prepost for solid mesh generation. Therefore, contact boundary conditions or constraints were not necessary to keep the abdominal muscles and spine together during model simulations.

2.2 Osteoligamentous spine

The osteoligamentous model contains seven vertebral bodies (T11-L5), sacrum, pelvis, and seven intervertebral joints (T11/T12-L5/S1). In order to account for the upper torso, an additional node was tied to T11 which provides the necessary mass of 18.94 kg. Joints are modeled using six-degree-of-freedom beam elements. Vertebral bodies are rigid and linked by the intervertebral joints. The use of rigid bodies reduces the mass of each body to its center of gravity and treats the rigid body mesh as a set of dependent nodes [48]. As such, the shell elements used to model the vertebrae, sacrum, and pelvis are used for contact interaction only.

2.2.1 Torso

The upper torso mass was modeled as a point mass fixed in space at the upper torso center of gravity. The center of gravity and mass characteristics of the upper torso were calculated from the relative mass percentages of the head, upper torso, and upper arm from Zatsiorsky [49]. A 70 kg male was chosen, resulting in an upper torso mass of 18.94 kg at a position 2.7 cm anterior to and 45 cm superior to the sacrum CG (the spatial origin of the model). The mass was constrained to the T11 vertebral body. The location of the upper torso mass node relative to the rest of the lumbar model is shown in Figure 6.

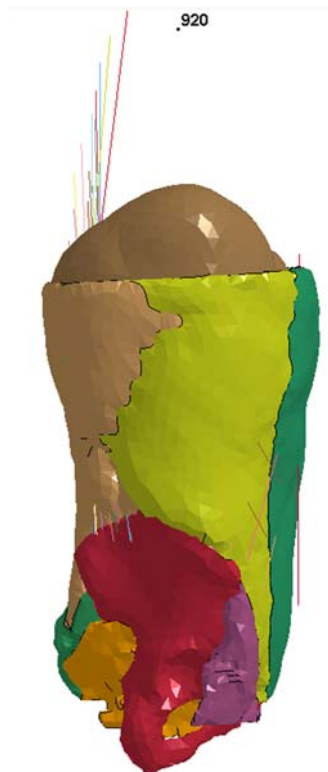


Figure 6. Lumbar model with upper torso mass indicated by black node 920 near top of image. The upper torso mass is constrained to move with the T11 vertebral body.

2.2.2 Vertebrae

Lumbar vertebrae were modeled as individual rigid bodies. Bony rigid bodies include six vertebral bodies (T11 to L5), as well as the sacrum and pelvis. Inertial properties for the lumbar vertebrae were determined via segmentation (Section 2.1.2). Vertebral masses were averaged from nine cadaveric lumbar spines. The resulting masses from cadaveric data and moments of inertia from imaging analysis are given in Table 6 above. Vertebral body centers of gravity were adapted from Stokes and Gardner-Morse [50].

2.3 Joints

Intervertebral discs, ligaments, and facets were lumped together into single-joint properties. Six-degree-of-freedom beam joints were used to model viscoelastic joint properties. Joint centers of rotation were modeled as the midpoint between the vertebral bodies given in Stokes and Gardner-Morse [50].

Compression properties are from Brinckmann [4]. Brinckmann was chosen for compression data as there exists data for both male and female joint segments, and sex-specific models could be produced with this data. There are 31 functional spinal units that met the previously established inclusion criteria and were below 50 years old [4] (Figure 7).

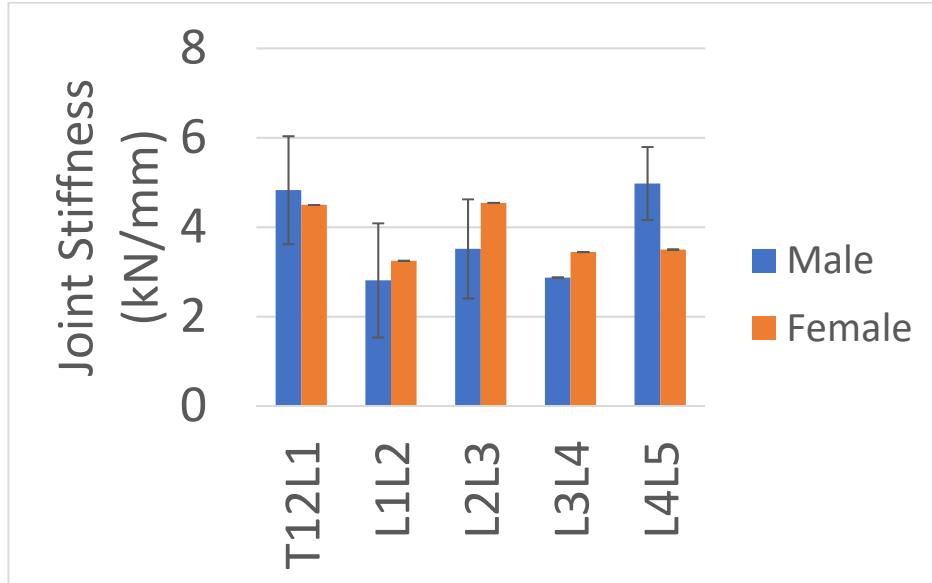


Figure 7. Compressive joint stiffness properties from Brinckmann (1988) for male and female segments less than 50 years of age. The male subjects also include standard deviations.

Tension properties are scaled based on lumbar endplate area from the Duke cervical model [51]. As compression is of more interest than tension for this study, scaling cervical tension data should not negatively impact the results. First, the L3L4 joint force displacement curve to fracture from Brinckmann [52] was scaled by peak force and peak displacement for each joint level. Then, the low rate UBB osteoligamentous test (Chapter 5, Section 2) was simulated with the Brinckmann properties. However, as these are low-rate compression properties, high-rate underbody blast data from experimental tests were used to calibrate the model. The peak force from the experimental test was divided by the peak force from the Brinckmann curve model simulation to find a compression stiffness scale factor. This resulted in a scale factor of approximately two in axial stiffness properties to account for the high rate loading conditions of interest in this study. This calibration results in the compression/tension curves seen in Figure 8.

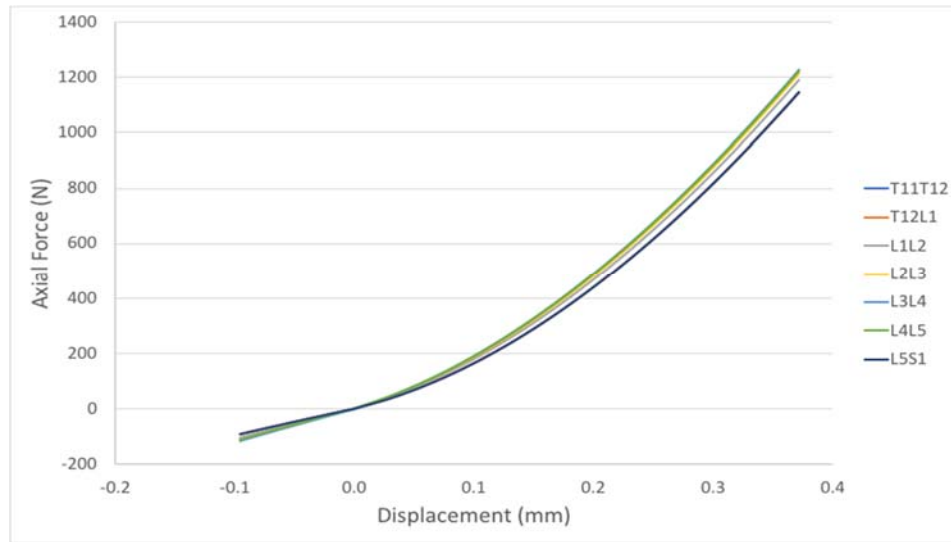


Figure 8. Calibrated compression (positive) and tension (negative) axial stiffness curves for the lumbar model. L5S1 is slightly softer than the upper lumbar spine.

Anterior and posterior shear properties are scaled from cervical model [53] using endplate areas. Joint-specific bending stiffness (Figure 9) are from Adams [54-56]. The bending response of the L5/S1 joint is qualitatively different from the upper lumbar spine joints. For injurious loading of the lumbar spine, capturing this difference in response is likely critical for accurate reproduction of biofidelic angular displacements.

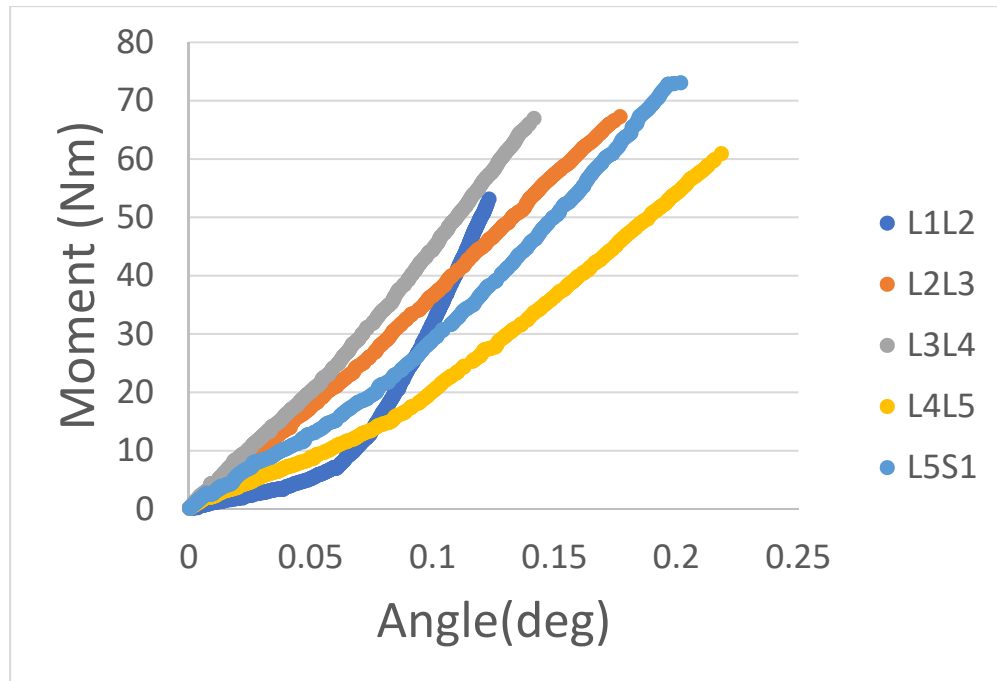


Figure 9. Lumbar spine bending response adapted from Adams 1980, 1991, and 1994. The L5/S1 joint indicates qualitatively different behavior than the rest of the spine.

Shell finite elements with a null material model were used to geometrically model the intervertebral discs. These elements do not contribute to joint stiffness, but allow a surface for contact with the abdominal pressure part. This ensures the abdominal pressure part does not penetrate the posterior of the model during loading, and prevents stress concentrations which might result from mesh distortion in these regions.

2.4 Muscles

Muscle anatomy for rectus abdominis, external and internal oblique, quadratus lumborum, longissimus, iliocostalis, and multifidus muscles were given in Stokes and

Gardner-Morse and were determined via an analysis of available literature and the Visible Human Project [50]. Stokes and Gardner-Morse separate the muscles into numerous strands to account for varying origin and insertion points. This results in 90 muscle strands for the 11 active muscles. The individual strands are seen relative to the full model in Figure 10. Muscle origin and insertion locations, bony attachments, physiological cross-sectional areas (PCSA), are adapted from Stokes and Gardner-Morse [50]. A view of the lumbar model with active muscles included is shown in Figure 10.

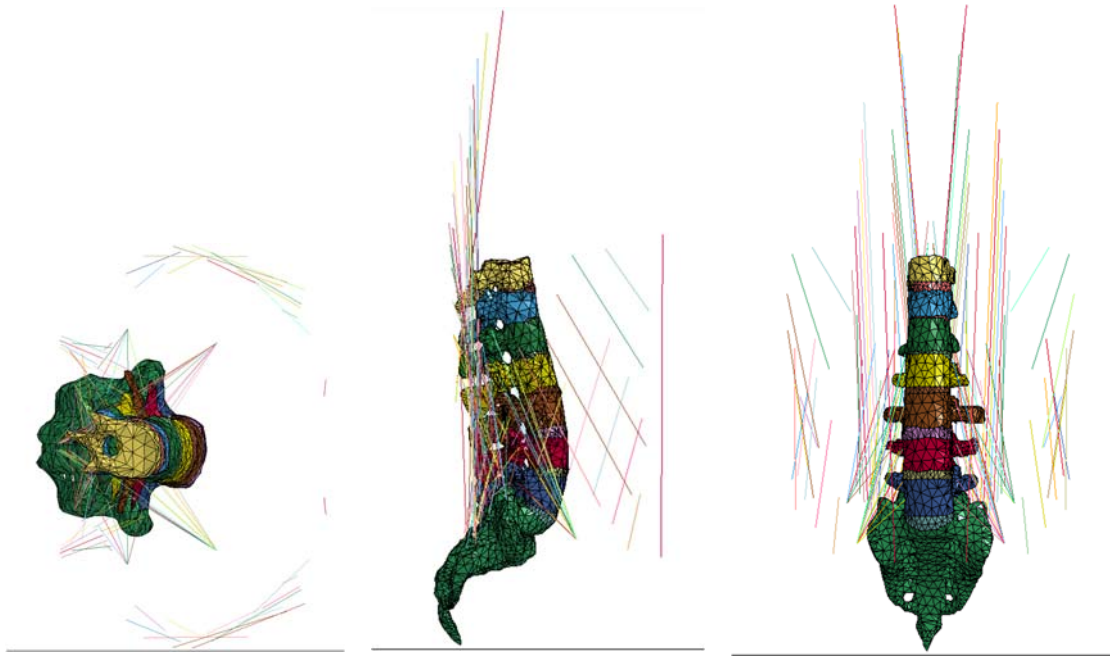


Figure 10. Developed lumbar spine model including anatomically correct muscle attachments from (left) top view (middle) lateral view and (right) frontal view. The solid mesh of the passive muscles and pelvis have been removed to view the spatial relationship of the active beam elements to the osteoligamentous spine.

Muscles superiorly insert on the ribs, and inferiorly from T8 through the sacrum/pelvis, depending on the strand. Since some of the muscles attach outside the lumbar spine, i.e. on the ribs or sacrum and pelvis, it is necessary to include a boundary condition that accommodates these attachments. For muscles that have superior attachments to T12 (other thoracic vertebrae or ribs), nodes at the attachment coordinate are rigidly affixed to the upper torso mass. Therefore, these attachments exist at the correct coordinate in space, but will move with the upper torso mass. This assumes there is no relative motion between the anatomical attachment part and the upper torso

mass (i.e. no movement between ribs and thoracic vertebrae, or between thoracic vertebrae). Similarly, for muscles that have inferior attachments that are on the pelvis, nodes at the attachment coordinate are rigidly affixed to the sacrum. The pelvis of the model was rigidly constrained to the sacrum, which assumes no motion between the two bony parts, and so a sacroiliac joint was not included in the model.

Muscles are modeled using multi-segment sliding contact beam elements [57]. A Hill-type lumped parameter model permits both an active (contractile) component to the muscle. The active component is dependent on a prescribed activation level that varies with time, maximum isometric stress, strain, and strain rate (Table 5). The active element was incorporated in the same manner as a previously published cervical model [9].

The passive component is strain-rate dependent [58] and modeled using solid elements. This differs from the Duke cervical model so that the pressurized abdominal volume is contained during dynamic . It allows the solid abdomen mesh to interact with both the muscles as well as the osteoligamentous spine. The passive muscle properties are the same as those used by the GHBMC model. This material model is an Ogden rubber model by Hedenstierna and Halldin [59] and was used to capture the behavior of passive muscles. Material coefficients for this constitutive model are listed in Table 7.

Table 7. Passive muscle properties from Hedenstierna and Halldin 2008 for *MAT_OGDEN_RUBBER LS-DYNA material card.

Density (kg/m³)	1.06				
Poisson's ratio	0.49				
mu1 (Pa)	13337				
alpha1	14.5				
Gi (Pa)	522e+3	211e+3	375e+3	2.90E+05	8.00E+04
Beta i (s⁻¹)	1020	400	65	30	0.1

2.5 Intra-abdominal pressure

A complex problem in lumbar modeling is handling intra-abdominal pressure. The line of action of abdominal muscles are more complex than the muscles running along the spine, as they curve around a deformable space. This boundary condition can be defined in part by determining the state of intra-abdominal pressure. Intra-abdominal pressure ranges from 0.027-2.16 kPa, with a mean of 933 Pa for men , and was not found to be significantly different between males and females [23].

A finite element airbag mesh was inflated to fill the abdominal cavity bounded by the surrounding muscles and bone. As this stressed geometry can result in severe deformation of the initial mesh, the airbag was re-meshed to improve mesh quality. It was then solid meshed (Figure 11) to include proper mass and inertial response.



Figure 11. Abdominal volume solid mesh which is bound by and contoured to the diaphragm superiorly, pelvis and pelvic floor inferiorly, abdominal muscles anteriorly, and spinal muscles and spine posteriorly. This part is used to initialize the mean intra-abdominal pressure.

The solid mesh was modeled as an elastic solid with the density of a 95% water, 5% air mixture (993.36 kg/m³). To accurately model abdominal compliance, a Young's modulus of 78.96 kPa and a Poisson's ratio of 0.33 were implemented with *MAT_ELASTIC card for the abdominal solid. This results in a 0.657% volume change for the initial abdominal volume of 8.67 E-3 m³ during the application of mean intra-abdominal pressure. The shell mesh was attached to the solid mesh for applying mean intra-abdominal pressure. This was modeled in LS-DYNA using *LOAD_SHELL_SET, which allows the application of pressure to finite element shells. First, a baseline

abdominal pressure was used for passive muscles. The model was first equilibrated by applying mean intra-abdominal pressure of 933 Pa to the shell elements on the exterior of the abdomen over a time period to reach steady state pressure. After equilibration, active musculature and dynamic loading conditions could be simulated.

2.6 Development of a mass-matched female model

In order to obtain female results from the male model, a scaled model matching the 50th percentile male mass was needed. Scale factors in Table 8 were developed to most closely match a female of similar mass. All scale factors are reported as the ratio of the mean female value with respect to the male value. For example, the 85th female scale factor for height can be determined by

$$85^{th} SF_{height} = \frac{\overline{height\ 85^{th}\ female}}{\overline{height\ 50^{th}\ male}} = \frac{170.2\ cm}{177.0\ cm} = 0.961 \quad (1)$$

For future female model development and scaling, dimensions and ratios for a 50th percentile female were also included.

According to CDC growth charts, a 50th percentile male at age 20 is about 70 kg. This value was held constant for the iso-mass female model. Values from the female growth chart were interpolated to determine that a 70 kg female is approximately in the 85th percentile of females. An 85th percentile female corresponds to a height of 170.2 cm [60].

Trunk musculature regression models developed in [61] were used to calculate PCSA dimensions for the 50th male, 50th female, and 85th female. Because there were

multiple regression models for various trunk muscles, the final selected models used for this analysis depended on if a muscle group had available models for both sexes, and if the model depended on a variable that could be obtained for 50th male, 50th female, and 85th female such as weight, height, or BMI. BMI values for the three demographics were calculated using the height and weight data for that specific percentile rather than using the CDC percentile data for BMI.

Mean endplate area data for males and female was obtained from [4] for T12/L1 down to L4/L5. Assuming a normal distribution, sum of the mean and one standard deviation approximately corresponds to an 84th percentile. Therefore, the 85th percentile female was estimated this way. Other vertebral dimensions, such as length and width were calculated using the stature percentile data from [60] and plugging them in the stature-dependent regression models developed in [62].

Using the relationship for compression stiffness, $k = EA/L$, assuming Young's Modulus (E) remains constant between males and females, mean endplate areas from [4] and the relevant vertebral lengths calculated from [62] were used to develop compression stiffness scaling ratios. In Table 8, the values for compression stiffness are in terms of E . Female and male mean bending stiffness data was obtained from [54 63 64]. Again, a sum of the female mean and one standard deviation was used to obtain an estimate for the 85th percentile female. Additional dimensions for the torso were found

from the U.S. Army's 2012 Anthropometric Survey which explicitly included 85th female percentile data [65].

Finally, pelvic dimensions were particularly important because of the distinct genetic pelvis differences between males and females. Beyond the scaling ratios, certain pelvic dimensions, such as the sacral breadth and ischium breadth, allowed for more accurate lines of action for muscle activation. Mean data for ilium height, iliac breadth, sacral breadth, and ischium breadth were obtained from [66] and mean inlet diameter, a depth dimension, was obtained from [67] using a weighted average between white and black populations. All pelvic dimensions for the 85th percentile female were estimated from the given means and standard deviations.

Table 8. Scale factors for 85th percentile female and 50th percentile female with respect to 50th percentile male dimensions

	Dimension			Ratios		Source
	50 th M	50 th F	85 th F	85f/50m	50f/50m	
HEIGHT (cm)	177.0	163.4	170.2	0.961	0.923	[60]
PCSA (cm²)						[61]
--Avg of erector spinae	22.62	16.62	20.88	0.923	0.735	
--R. erector spinae	22.78	16.69	21.41	0.939	0.733	
--L. erector spinae	22.45	16.24	21.05	0.938	0.723	
--Avg of rectus abdominis	7.12	6.64	7.65	1.074	0.932	
--R. rectus abdominis	7.78	6.42	7.40	0.951	0.826	
--L. rectus abdominis	7.66	6.74	7.82	1.021	0.880	
ENDPLATE CSA (cm²)						[4]
--T12/L1	14.0	12.2	14.38	1.027	0.871	
--L1/L2	16.0	12.4	14.16	0.885	0.775	
--L2/L3	17.0	14.1	15.56	0.916	0.829	
--L3/4	17.5	13.7	15.67	0.895	0.783	
--L4/L5	17.3	15.4	17.34	1.002	0.890	
VERTEBRAL PROPERTIES (cm)						[62]
--length (L2-L4)	10.63	10.01	10.45	0.983	0.942	
--width (L2-L4)	4.01	3.77	3.89	0.970	0.940	
COMPRESSION STIFFNESS (k=EA/L)						[4 62]
--T12/L1	1.32 E	1.22 E	1.38 E	1.045	0.925	
--L1/L2	1.51 E	1.24 E	1.36 E	0.900	0.823	
--L2/L3	1.60 E	1.41 E	1.49 E	0.931	0.881	
--L3/4	1.65 E	1.37 E	1.50 E	0.911	0.831	
--L4/L5	1.63 E	1.54 E	1.66 E	1.020	0.945	
BENDING STIFFNESS (Nm/deg)						[54 63 64]
--Adams 1991	7.23	4.99	7.53	1.041	0.690	
--Adams 1980	7.99	5.83	8.50	1.064	0.730	
--Adams 1994	5.19	4.33	5.28	1.017	0.834	
--Combined Adams Data	6.77	4.94	7.16	1.058	0.730	
TORSO DIMENSIONS (cm)						[65]
--bicristal breadth	27.5	27.3	29.6	1.076	0.993	
--hip breadth	34.4	35.3	38.0	1.105	1.026	
--hip breadth, sitting	37.8	39.7	43.2	1.143	1.050	
--sitting height	91.8	85.7	89.1	0.971	0.934	
PELVIC DIMENSIONS (cm)						[66 67]
--ilium height	13.45	12.48	13.22	0.983	0.928	
--max iliac breadth	27.97	27.77	29.20	1.044	0.993	

--max sacral breadth	11.52	11.53	12.12	1.052	1.001	
--max ischium breadth	9.29	10.32	12.03	1.295	1.111	
--inlet diameter	9.9	11.1	12.2	1.232	1.121	

Changes in pelvis dimensions caused changes in insertion points, and therefore, lines of actions for muscles inserting on the pelvis.

2.7 Conclusions

A biofidelic model of the lumbar spine was developed based on high quality medical imaging and segmented reconstructions of the salient anatomy. The resulting model is a hybrid formulation containing a multibody osteoligamentous spine, beam-type active musculature, solid passive musculature, and solid intra-abdominal volume. Previously developed models have neglected to include the intra-abdominal cavity, which provides support for the surrounding musculature and is hypothesized to impact the resulting kinematics during high-rate dynamics.

2.8 Limitations

The developed model faithfully reproduces the anatomical complexity of the human spine. It incorporates validated methods for modeling both the osteoligamentous spine and supporting musculature. Nevertheless, the model possesses several limitations which could be improved by future work.

First, linear tetrahedral solid meshes, such as that used to generate the passive musculature, are well known to generate nonphysical results in some cases and are

generally regarded as too stiff [68]. In order to be sure that this does not occur for any loading scenarios which might be applied, future work would include replacement with a hexahedral solid mesh. For complex geometries and interfaces between multiple parts such as is encountered here, this represents a significant and nontrivial undertaking and is beyond the scope of the current work.

While the use of a multibody framework for the osteoligamentous spine provides significant savings in terms of computational cost, it precludes the direct determination of deformation and stresses within the vertebral bodies. While the loads at the joints provide some information about the internal mechanics and dynamics, the ability to localize regions of high stress within each body might be of use for comparing with experimental studies of lumbar vertebral fracture.

Finally, the use of a lumped mass as the superior torso is an obvious simplification. Since the model is designed for high-rate compression this is likely a reasonable assumption given the uniaxial nature of the input, it eliminates any degrees of freedom between the inferior thoracic spine and the upper torso center of mass. Whether or not such a simplification changes the resulting kinematics or osteoligamentous forces remains an open question. However, one primary advantage of using a lumped mass torso is the speed of computation when compared with a full finite element torso.

3 Active musculature optimizations against gravitational loading

3.1 Introduction

Previous work with realistic computational head and neck models has found they are unstable under gravitational loading in the absence of activated cervical muscles [69]. Also, differences in initial muscle activation can affect model kinetics during dynamic loading [69 70]. Our group has found that multiple muscle segments increase the realism of kinematic and kinetic response [57]. Vasavada et al. found that females had significantly more slender necks, but greater head mass per unit muscle area when subjects were matched for height and neck length [71]. This may indicate a difference in muscle activations between males and females to maintain head stability. Similar behavior may occur in the lumbar spine, where upper torso masses differ between males and females[49]. Cervical spine model simulations have found that active musculature affects not only model kinematic response, but model forces, and may play a dramatic role in failure response. For example, tensed muscle response may contribute 40% or more of the compressive tolerance of the adult and pediatric neck [69].

This dissertation hypothesizes that the use of active musculature improves model kinematic response to volunteer data. To investigate this hypothesis, muscle activation states were determined for the lumbar multibody models under gravitational loading. Additionally, no models were found that were used for vertical impact loading

and contained active musculature, therefore muscle optimizations were necessary for the lumbar model developed in this dissertation.

While there are many lumbar models that include active musculature, only a few have examined gravitational loading[72 73]. Hwang, et al. [74] includes gravitational moments of body segments as model inputs, as well as active muscles, but their active muscles are based on EMG data from surface electrodes in experimental tests, as opposed to the optimized activations investigated here. Others either did not include gravitational loading, or did not mention if it was included[36 75-80]. Panjabi [81] includes both gravitational preloads, as well as active musculature, but sets all activation levels equal. Han, et al. [82] includes intra-abdominal pressure, but not active musculature.

Chancey, et al. [70] details a methodology of determining both a tensed and relaxed muscle activation scheme for use in cervical models. This methodology has been successful in additional cervical spine models (pediatric six and ten year old) [69], and thus was chosen for the general methodology in the lumbar model muscle optimization. During compressive loading of the time range seen in under body blast events, there is not enough time for muscles to have time dependent responses to the event. However, muscle activation states prior to the event will persist over the entire event and affect spinal loading.

The primary objective of this chapter was to follow the methodology reported by Chancey, et al. [70] and [69] to determine relaxed and tensed muscle activation states for the 50th percentile male model. These activation states can then be applied to more complex and dynamic scenarios, such as underbody blast. It is expected that the activation optimizations for males and females will differ due to geometric differences in the osteoligamentous spine, and PCSA differences in the muscles.

3.2 Methods

3.2.1 Optimization details

Two muscle activation schemes were investigated. The first was a relaxed state which models an unaware, or unbraced subject. The relaxed state cost function was used by Dibb et al. [69]. This activation scheme seeks to minimize muscle fatigue (Eq. 2) while keeping the lumbar spine stable. Muscle fatigue is defined as the sum of squares of the ratio of muscle force to the maximal muscle force [83].

$$\min f(\alpha) = \sum_{i=1}^{11} \left(\frac{F_i}{F_{max,i}} \right)^2 = \sum_{i=1}^{11} \alpha^2 \quad (2)$$

Muscles were constrained to positive forces. The optimization rejects models if the upper torso mass displaces more than 3 mm in the AP direction, or if the T12/L1 joint force exceeds a 50th percentile risk of fracture of 5237 N. The sacrum was held fixed, and the remaining vertebrae were constrained to only move in the sagittal plane. By enforcing these optimization tolerances, the optimization keeps the spine upright under

gravitational loading. Initial activation levels were set to 0.15 and bounded between 0.001 and 0.25.

The second state is a tensed state which seeks to model a maximally braced subject. This activation scheme maximizes total muscle force (Eq. 3) while keeping the spine stable and uninjured.

$$\max f(\alpha) = \sum_{i=1}^{11} F_i \quad (3)$$

Again, muscles were constrained to only positive forces. The optimization rejects models if the upper torso mass displaces more than 3 mm in the AP direction, or if the T12/L1 joint force exceeds the 50th percentile risk of fracture of 5237 N (detailed below, Figure 12).

Like the relaxed activation scheme, these torso displacement optimization tolerances are adapted from Dibb et al. [69]. The sacrum was held fixed, and the remaining lumbar vertebrae were constrained to only allow sagittal plane motion. By enforcing these optimization tolerances, the optimization will keep the spine upright under gravitational loading and ensure muscular contraction will not result in spinal injury during gravitational loading. Initial activation levels were set to 0.01 and bound between 0.001 and 1.00.

Activation levels, $0 \leq \alpha \leq 1$, of each of the 11 muscle pairs were varied using Latin Hypercube point selection for 20 experiments per iteration. There was a maximum of 10 iterations for the tensed state, and 20 iterations for the relaxed state. All constraints were

set to soft, which allows constraint violations if needed. Optimizations completed when design change tolerance, objective function tolerance and metamodel accuracy reached 0.01. Metamodel sampling settings included fitting the lumbar spine model responses to a polynomial metamodel with linear order. The optimization algorithm is a hybrid algorithm with Adaptive Simulated Annealing (ASA) with a switch to Leap Frog Optimizer (LFOP). Time history outputs included force histories for each of the 90 muscle strands, as well as the T12/L1 joint force history, and torso kinematics.

The 11 active muscle pairs were separated into 90 different muscle strands to account for different origins and insertions along the length of the muscle (see Chapter 2.4 and Figure 10). Gravity was simulated in LS-DYNA through a constant 9.81 m/s^2 load in the superior to inferior direction applied to the entire model. The stability of the model was quantified using the maximal torso center of gravity translational and rotational displacement, and comparing the 50th percentile risk of injury in T12/L1. Prior to muscle activations, the abdomen was pressurized to a mean intra-abdominal pressure of 933 Pa [84] to reach steady-state pressure during gravitational loading. Thus, the only variable that changed during this simulation was the activation levels of the muscles. Simulations ran for 30 ms, which allowed for a muscle response to reach its peak load, as the muscle activation state time constant is 15 ms [45].

3.2.2 Underbody blast failure tests and injury risk curve development

An injury risk curve for lumbar spinal fracture from axial loading (Figure 12) was generated from underbody blast failure tests for a nominal posture plus or minus a standard deviation of the posture (Duke unpublished data). These experimental tests are whole spine osteoligamentous compression tests meant to simulate underbody blast. The lumbar spine from 29 cadavers were potted in a fixed-fixed end condition in a posture representative of a seated soldier [85]. The caudal end was loaded via displacement control to nominal loading rates of 200, 400, and 600 N/ms, and then failure. The force at failure for these 29 lumbar spine experiments were used to create a survival plot from T12/L1 axial force at fracture using a Weibull fit.

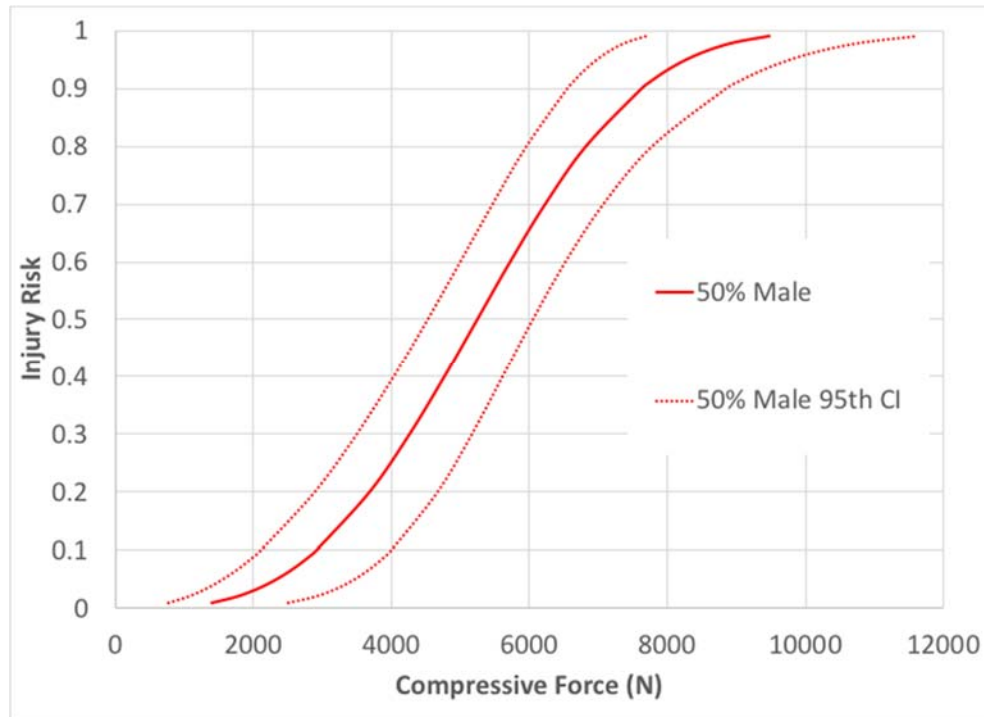


Figure 12. Injury risk curve for fracture force at T12/L1 from UBB failure tests (Bass, unpublished data)

3.3 Results

The relaxed optimization converged after 17 full iterations with no constraint violations on the converged solution. Figure 13 and Table 9 show the converged activation levels for the 11 active muscle pairs. All activation levels are well below ten percent, resulting in axial forces of less than 15 N per muscle.

Table 9. Active lumbar muscles relaxed optimized activation levels

Muscle	Variable name	Activation Level
External oblique	EXTOBLACT	1.00E-03
Internal oblique	INTOBLACT	1.00E-03
Rectus abdominus	RECTABDACT	1.00E-03
Thoracic Multifidus	THMULTACT	1.00E-03
Lumbar Multifidus	LUMULTACT	6.14E-03
Longissimus pars Lumborum	LOPLUACT	2.42E-03
Iliocostalis pars Lumborum	ILPLUACT	3.58E-03
Longissimus pars Thoracis	LOPTHACT	1.90E-02
Iliocostalis pars Thoracis	ILPTHACT	6.94E-03
Psoas	PSOASACT	1.00E-03
Quadratus Lumborum	QULUMACT	3.76E-03

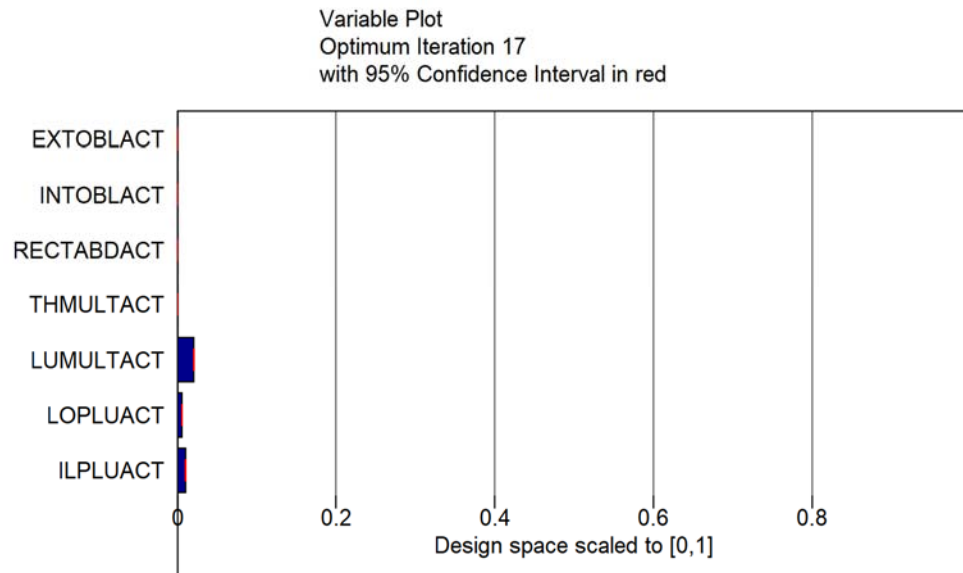


Figure 13. Relaxed muscle activations indicate slight contraction of the extensor muscles to maintain an upright torso

While all muscle activation levels were low, there was higher contraction of the extensor muscles in keep the torso upright. This effect is expected because of the

moment of the upper torso about the location of the spine. The posterior displacement of the torso CG was most sensitive (metamodel sensitivity using linear ANOVA) to the external oblique, rectus abdominus, and thoracic multifidus activation levels (Figure 14). External oblique sensitivity was 283% larger than the rectus abdominus sensitivity, and 318% larger than the thoracic multifidus sensitivity.

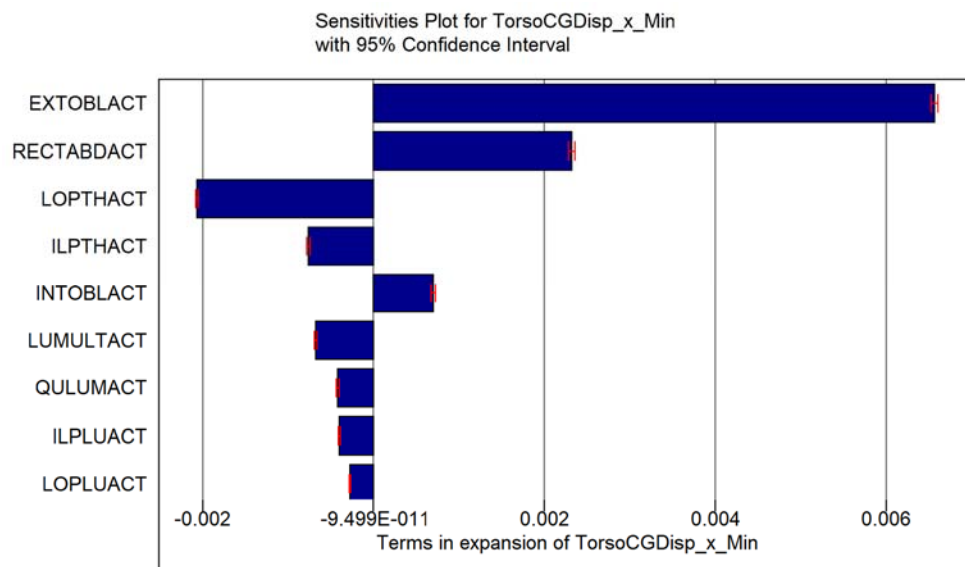


Figure 14. Sensitivity of the posterior torso CG displacement to relaxed muscle activations. Descriptions for variable names are found in Table 9.

Unlike the relaxed activation, the tensed activation produced co-contraction of flexors and extensors at very high activation levels (Table 10 and Figure 15). All activation levels were between 75 and 100 percent. The lumbar multifidus, iliocostalis pars lumborum, and quadratus lumborum all optimized to a maximum activation level of 1. The iliocostalis pars thoracis had the lowest activation level at 76%. All abdominal muscles activated to levels above 90 percent.

Table 10. Active lumbar muscles tensed optimized activation levels

Muscle	Variable name	Activation Level
External oblique	EXTOBLACT	9.48E-01
Internal oblique	INTOBLACT	9.85E-01
Rectus abdominus	RECTABDACT	9.37E-01
Thoracic Multifidus	THMULTACT	8.94E-01
Lumbar Multifidus	LUMULTACT	1.00E+00
Longissimus pars Lumborum	LOPLUACT	9.52E-01
Iliocostalis pars Lumborum	ILPLUACT	1.00E+00
Longissimus pars Thoracis	LOPTHACT	9.79E-01
Iliocostalis pars Thoracis	ILPTHACT	7.63E-01
Psoas	PSOASACT	9.39E-01
Quadratus Lumborum	QULUMACT	1.00E+00

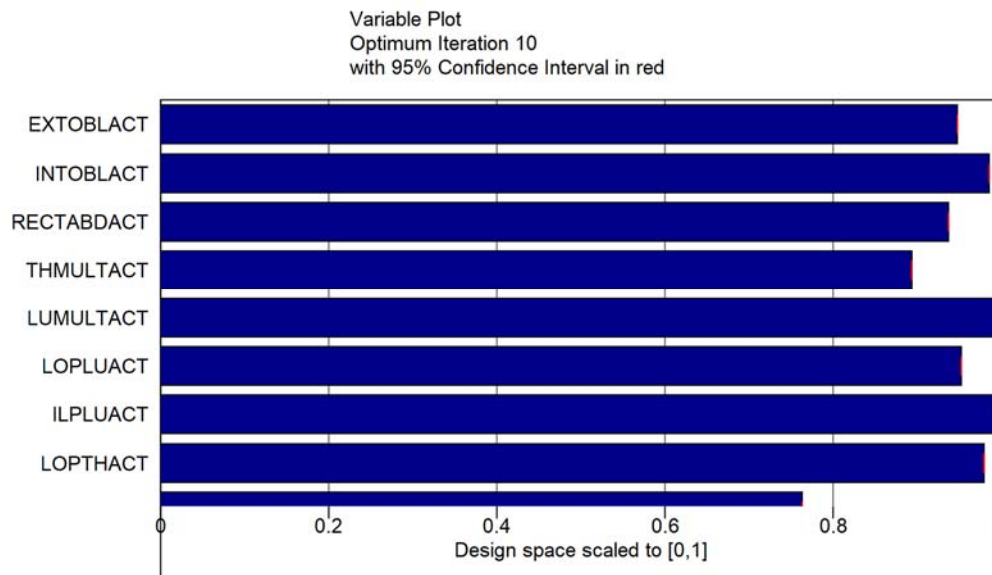


Figure 15 Tensed muscle activations for 11 different muscles all exceed 70 percent activation, and there is co-contraction of flexors and extensors

The compressive force in T12/L1 reached 2623 N (Figure 16), which corresponds to a seven percent risk of failure (Figure 12). Activation levels for the tensed state resulted in axial forces of 50 to 600 N per muscle. The optimization quickly reached a

steady-state value for the T12/L1 axial force. However, computed infeasibilities of early iterations kept the model from converging until 10 iterations had passed. The tenth iteration resulted in a computed feasible solution.

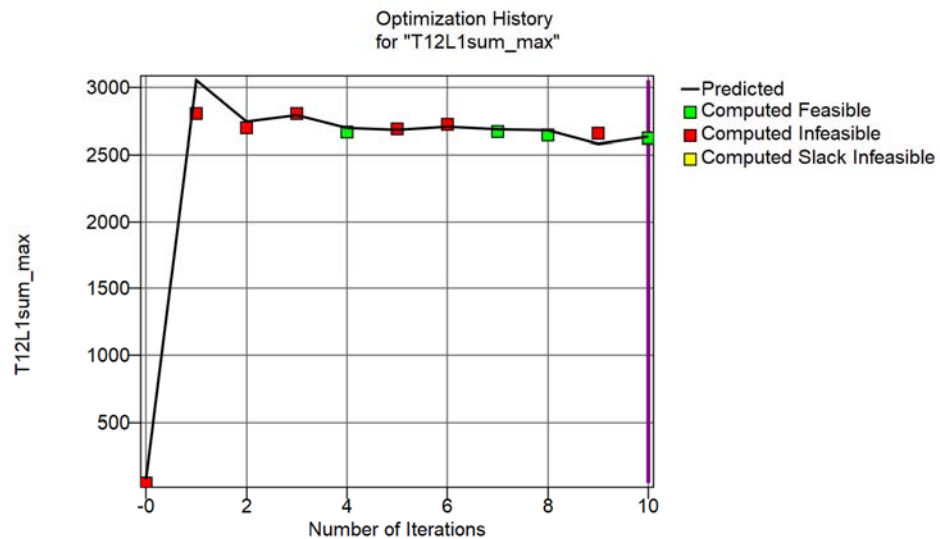


Figure 16. Optimization history for the maximum compressive force in Newtons in T12/L1 joint

Like the relaxed state, the tensed state showed posterior torso CG displacement to be most sensitive (metamodel sensitivity, linear ANOVA) to the activation levels of the external oblique, longissimus pars thoracis, and rectus abdominus. Here, the external oblique sensitivity is 65.5% greater than the longissimus pars thoracis sensitivity, and 178% greater than the rectus abdominus sensitivity. Therefore, while there are large co-contractions of all muscles in the tensed state, the external oblique had the primary influence on torso CG posterior displacement. While activation levels only

varied 24% across all muscles, kinematic sensitivities indicate these relatively smaller variances have a large effect on torso kinematics.

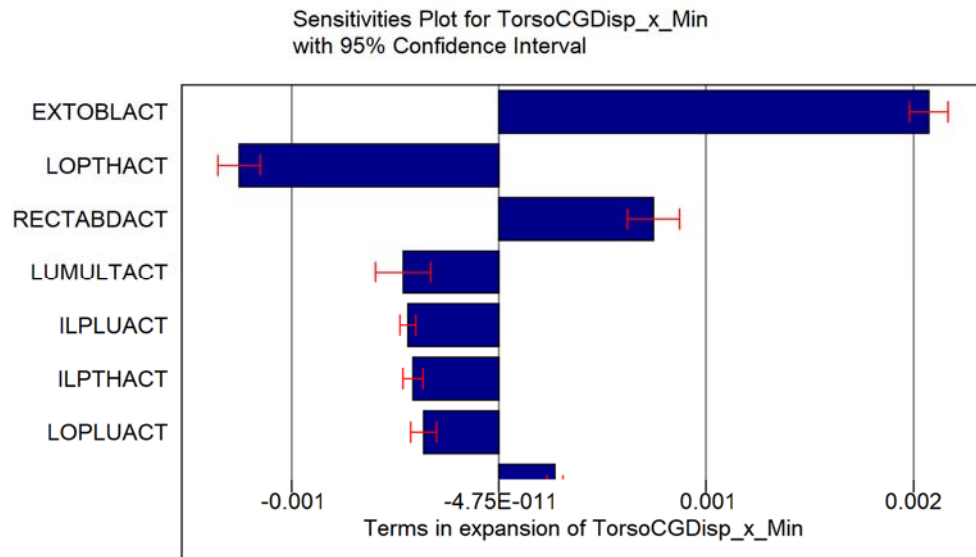


Figure 17. Sensitivity of the posterior torso CG displacement to tensed muscle activations

Intra-abdominal pressure was determined by outputting the pressure from the abdominal solid elements within 1 mm of the joint cutplane. This is 114 solid elements at L5S1 to 750 solid elements at T12L1. The tensed muscle state results in up to 16.3% increase of median intra-abdominal pressure (Figure 18). As the muscle activate, there is a ramp up period in change in intra-abdominal pressure. However, approximately 15 ms, the intra-abdominal pressure begins to reach steady state. This is consistent with the 15 ms activation time constant for musculature. After the 30 ms simulation where the tensed activation state is applied to the model, there is not a statistically significant

difference between intra-abdominal pressure by joint level (Figure 19). The box and whisker plot indicate a red dash at the median, with whiskers at the 25th and 75th percentiles. As the notches do not overlap, the pressure by joint levels are not statistically different. Red crosses represent elements that fall outside the 25th and 75th percentiles. While the pressures are not statistically different, there is a larger variance at the lower joint levels. This is likely due to the large geometric variances at the lower joint levels. At L4L5, there is anthropometric differences due to the psoas muscle, while L5S1 is largely constrained by the rigid pelvis. This contrasts to the more superior joints, which are constrained by abdominal musculature, the erectors, and the osteoligamentous spine (Figure 20). This variance may be reduced in the future by using a material card which does not support tension, increasing the time over which the mean intra-abdominal pressure is applied, and increasing the simulation time for tensing the muscles. This may result in less variance in the steady-state values across the cut planes.

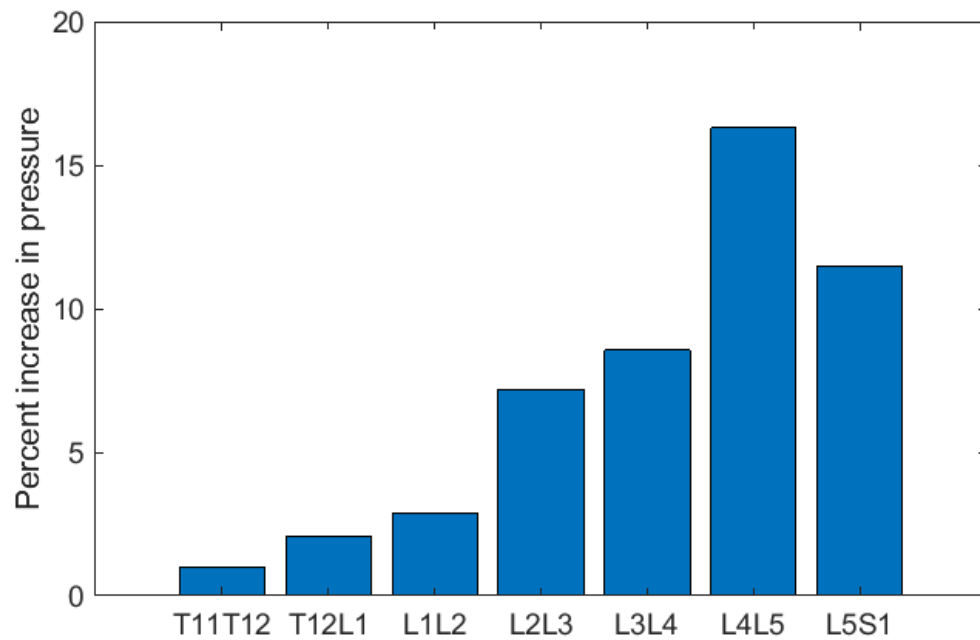


Figure 18. Percent increase in intra-abdominal pressure by joint level over the 30 ms of tensed muscle activation.

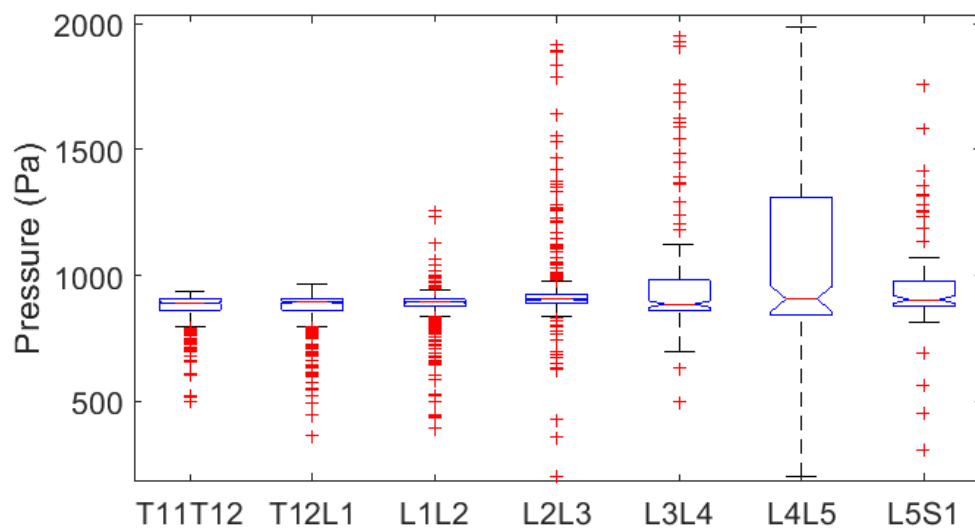


Figure 19. Box and whisker plot of intra-abdominal pressure after tensed activation state. Whiskers represent the 25th and 75th percentile, and the central red dash marks the median. Intra-abdominal pressure does not differ by joint level.



Figure 20. Model transverse cut planes at joint centers of rotation. Left- T12L1, middle- L4L5, right- L5S1. Solid elements in full color, with shell parts outlined.

3.4 Discussion and Limitations

No previous lumbar models with active musculature have been developed for high rate compression loading. Since the material properties of the spine were developed for high rate loading, an active muscle optimization may result in different muscle recruitment and activation levels than in other computational models. A limitation of this study was that optimization results may be non-unique, as well as dependent on both model and optimization constraints (*cf* [86]). While this optimization was limited to motion within the sagittal plane, biological response allows motion in all planes, and would take into account any differences in symmetry between the left and right side of the body. Since the primary lumbar spine response in compressive loading is compression and bending, a sagittal plane motion constraint is sufficient. While other

muscle activation schemes may exist, these optimization schemes present two possible conditions for keeping the torso upright without additional dynamic loading. These schemes are vital inputs to further lumbar spine modeling.

In the relaxed activation state, extensor activations were higher to keep the torso stabilized. In the tensed state, there was co-contraction of both flexors and extensors. This agrees with the results of Dibb, et al. [69], which analyzed the cervical spine stabilization against gravitational loading. In both the lumbar and cervical spine, there is a lordosis of the spine, with the head/torso CG anterior of the spine. Both states keep the spinal forces below the known risk for fracture failure. For the tensed state, the load in the spine is at seven percent risk of failure.

3.5 Conclusion

Muscle activation states were found over 30 ms to maintain an upright posture against gravitational loading. Both activation schemes investigated, torso stability (quantified by torso CG displacement) was most sensitive to external oblique activation. For an unaware subject, activation of the extensor muscles is necessary to maintain an upright torso. In the relaxed state, the largest activation was 1.9 percent, resulting in maximum muscle forces of less than 15 N. Still, extensor activations are 2.4 to 19 times greater than flexor activations. For an aware subject, large co-contraction of both flexors and extensors will maintain an upright torso without fracturing the lumbar spine. Muscle activations vary from 76 to 100 percent for the tensed state. The compressive

force during a tensed activation reaches 50 percent of the estimated failure force, which can exacerbate risk of injury during compressive loading. Muscle activations result in changes in intra-abdominal pressure of up to 16 percent.

4 Sensitivity analysis of the male model

4.1 Introduction

The work proposed investigates differences in male and female biomechanical response due to differences in stature, mass distribution, and muscle activation.

However, it is possible that while differences might arise in these simulations, they could be due to the specific conditions and parameters chosen. For example, Hansen et al. found that changes in muscle line-of-actions affected model outputs [87]. Therefore, a sensitivity analysis is needed to determine the realistic range of responses. The importance of model input parameters for underbody blast loading with active musculature was analyzed via a sensitivity analysis using LS-OPT (LSTC, Livermore, CA).

4.2 Methods

4.2.1 Sensitivity analysis methods

A sensitivity analysis was conducted by varying parameters within plus and minus one standard deviation as reported in literature (Table 11). Both geometric model parameters and material properties were varied. This was used to determine which parameters had the most effect on model response and injury outcome. In XX, while some parameters are varied over their range such as CG position in meters, others are varied as scale factors, such as vertebral mass scale factor. Here, scale factors are defined as

$$SF_{min} = \frac{mean - STD}{mean} \quad (4)$$

$$SF_{max} = \frac{mean + STD}{mean} \quad (5)$$

Vertebral bodies anteroposterior positions were varied independently. Vertebral masses and inertias were varied jointly. Muscle origin/insertions were varied jointly in x/y/z. Muscular cross-sectional areas scale factors were varied the same for all muscle strands.

Spine and torso parameters included the anteroposterior position of the vertebral bodies and upper torso mass, the axial position of the upper torso mass, and vertebral mass and inertial scale factors. Initial intra-abdominal pressure values were the mean male intra-abdominal pressure of hospitalized patients.

Scale factors for both the active and passive muscle components were generated. For the passive muscle, the passive muscle stiffness standard deviation was assumed to be the same as that applied to the cervical model [58]. The active beam elements were varied geometrically by their cross-sectional area, and origin and insertion points. Parameters affecting muscle response such as peak isometric stress, maximum shortening strain rate, and force velocity scale factor were included in the sensitivity analysis.

Joint stiffnesses were scaled for tension/compression, flexion/extension, and shear. Additionally, the translational and rotational dampers used in parallel with the springs were varied in accordance with the methodology used by Dibb, et al. [38].

Finally, the energy loss ratio for the lumbar spine was assumed to match that for the cervical spine, and was varied across its standard deviation.

Table 11. Sensitivity analysis variables and input ranges by category. SF= Scale factor

	Variable Description	Variable Name	Value	Min	Max	Source
Spine and Torso	L1 X CG Position (m)	CGL1	-0.0084	-0.0167	-0.0001	[50]
	L2 X CG Position (m)	CGL2	0.0036	0.0162	-0.009	[50]
	L3 X CG Position (m)	CGL3	0.0174	0.0044	0.0393	[50]
	L4 X CG Position (m)	CGL4	0.0262	0.0131	0.0393	[50]
	L5 X CG Position (m)	CGL5	0.0162	0.012	0.0204	[50]
	T11 X CG Position (m)	CGT11	-0.0195	-0.0364	-0.0026	[50]
	T12 X CG Position (m)	CGT12	-0.0158	-0.0302	-0.0014	[50]
	Torso CG X Disp (m)	torsox	0	-0.099	0.099	[20]
Abdomen	Torso CG Z Disp (m)	torsoz	0	-0.218	0.218	[20]
	Vertebral Mass Scale Factor	VmassSF	1	0.757	1.243	Duke cadaveric data, n=9
	Vertebral Inertial Scale Factor	InertSF	1	0.695	1.305	MRI/CT imaging study, n=9
Abdomen	Initial Intra-abdominal Pressure (Pa)	IAPinit	933.26	466.63	1400	[23]
Muscles	Max Isometric Stress (Pa)	IsostressSF	500000	250000	750000	[44]
	Muscle PCSA Scale Factor	PCSASF	1	0.732	1.268	[88]
	Max Shortening Strain Rate (s ⁻¹)	edotmax	0.5	0.25	0.75	[45]
	Maximum Relative Force	fvml	1.5	1.1	1.8	[89]
	Force Velocity Scale Factor	fvsh	0.3	0.2	0.3999	[45]
	Passive Stiffness SF	PassStiffSF	1	0.712	1.303	[58]
	Energy Loss Ratio SF	ELR	1	0.838	1.162	[90]
	Origin/Insertion X Disp SF	dispSFx	1	0.81884	1.18116	[91]
	Origin/Insertion Y Disp SF	dispSFy	1	0.81884	1.18116	[91]
	Origin/Insertion Z Disp SF	dispSFz	1	0.81884	1.18116	[91]
Force Length Shape Factor	sk	0.4	0.179	0.59428	[45]	
Joints	Tension/Compression Stiffness Scale Factor	ComSF	2	1.4997	2.5003	[4]
	Flexion/Extension Stiffness Scale Factor	BendSF	1	0.616	1.384	[54-56]
	Shear Stiffness SF	ShearSF	1	0.178	3.915	[38]
	Translational Damper SF	DMPtSF	1	0.5	2	[38]
	Rotational Damper SF	DMPrSF	1	0.5	2	[38]

Model inputs were varied using Latin Hypercube point selection for 44 cases (the default number of cases for linear order without interactions for 28 independent variables). Metamodel sampling settings included fitting the lumbar spine model responses to a polynomial metamodel with linear order. Time history outputs included force histories for each of the muscle strands, vertebral joint compressive and shear histories, abdominal pressure time histories, and torso kinematics. Sensitivity analysis responses for comparison with input parameters were based on the maximum or minimum value of the time history responses.

4.2.2 Model simulation methods

The simulated condition that was used for the sensitivity analysis was the Duke unpublished UBB subfailure test. These tests were whole spine osteoligamentous compression tests meant to simulate underbody blast. The spine was potted in a fixed-fixed end condition in a posture representative of a seated soldier [85]. The caudal end was loaded via displacement control to nominal loading rates of 200, 400, and 600 N/ms, and then to failure. This sensitivity analysis used the 200 N/m subfailure test to investigate model response to input parameters. The mean axial displacement profile from the experimental tests (Figure 21) was applied to the sacrum of the model. The *BOUNDARY_PRESCRIBED_RIGID_MOTION card in LS-DYNA was used to apply axial displacement. As in the experimental test, T12 was held fixed, the sacrum free in Z

displacement, and the remaining vertebral bodies restricted to movement in the sagittal plane.

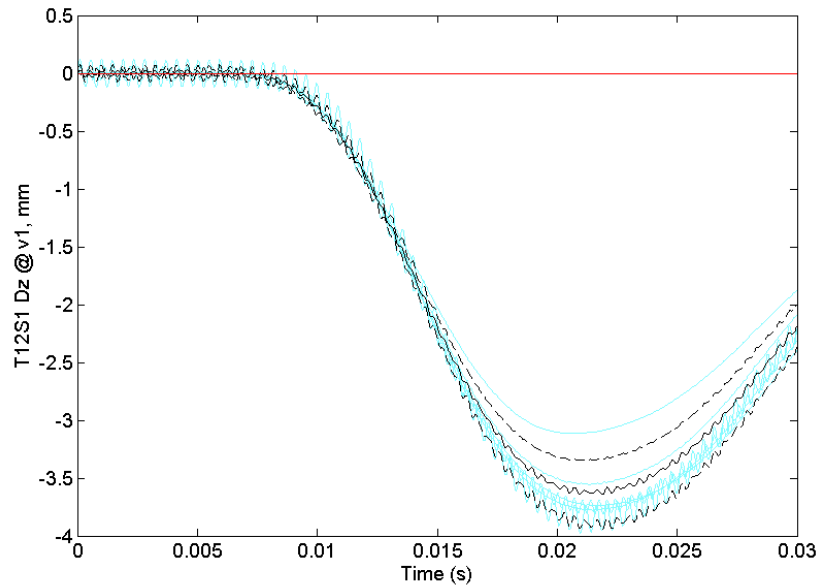


Figure 21. Experimental axial displacement for subfailure test (Duke, unpublished data)

4.3 Results

The peak intra-abdominal pressure in the upper lumbar spine (T12/L1) was most sensitive to axial stiffness, muscular cross-sectional area, and initial intra-abdominal pressure (Figure 22). Axial stiffness and initial intra-abdominal pressure are negatively correlated with peak intra-abdominal pressure. In the sensitivity analysis, peak intra-abdominal pressure is reported as a negative value, while the parameter intra-abdominal pressure is a positive value. Therefore, as axial stiffness and initial intra-abdominal pressure increase, so does the maximum intra-abdominal pressure. It is expected that if the mean initial pressure increases, so should the response. As axial

stiffness increases, the model shifts more of the load to the abdomen, increasing intra-abdominal pressure as a result. As muscular cross-sectional area increases, peak intra-abdominal pressure decreases. This is a result of more of the axial load being borne by musculature, instead of the abdominal viscera.

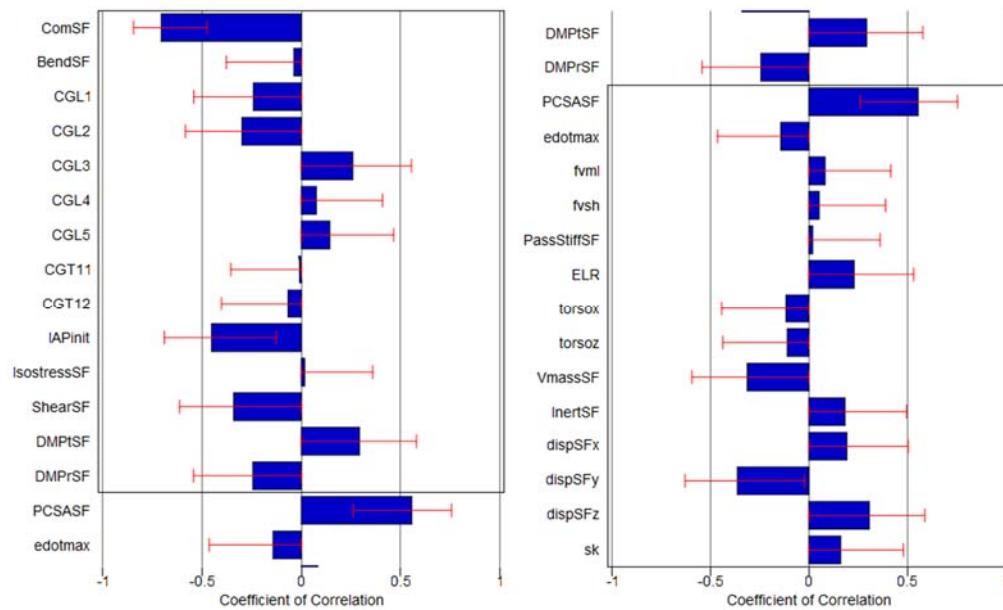


Figure 22. Coefficients of correlation for intra-abdominal pressure at the T12/L1 joint level with 95% confidence intervals in red

The peak intra-abdominal pressure in the lower lumbar spine (L5/S1) was most sensitive to bending and shear stiffness (Figure 23). Of those with the strongest correlation, bending and shear have a positive correlation. In the lower lumbar spine, as bending and shear stiffnesses increase, there is increased loading placed on the abdomen from the spine. This leads to increased intra-abdominal pressure.

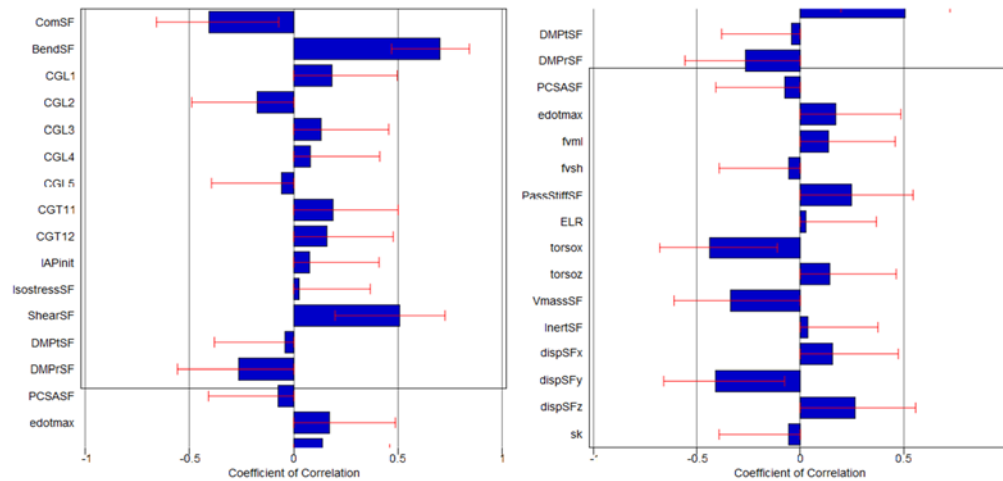
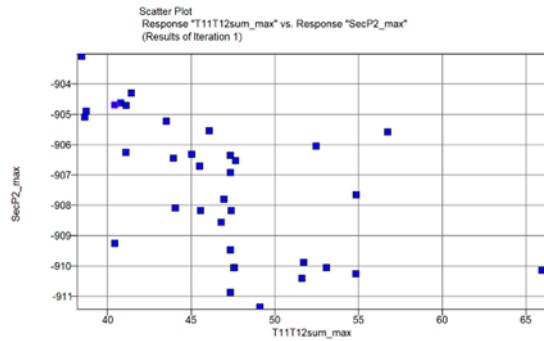


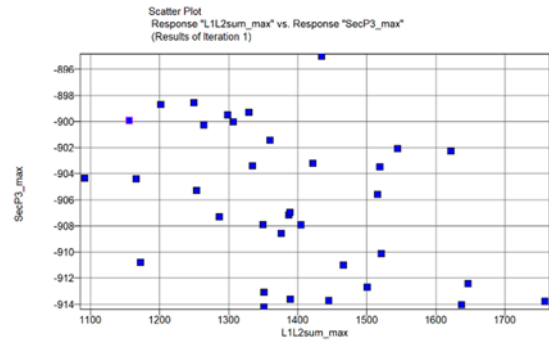
Figure 23. Coefficients of correlation for intra-abdominal pressure at the L5/S1 joint level with 95% confidence intervals in red

There was much stronger correlation to torso and muscle geometric parameters (torso CG x displacement, muscle origin/insertion scale factors) when compared to the upper lumbar spine. This means as the torso CG moves posterior, peak intra-abdominal pressure increases. In the L5/S1 joint, as the muscles origin/insertions move more anterior or superior, intra-abdominal pressure decreases. But as the origin/insertions move farther away from the spine laterally, intra-abdominal pressure increases.

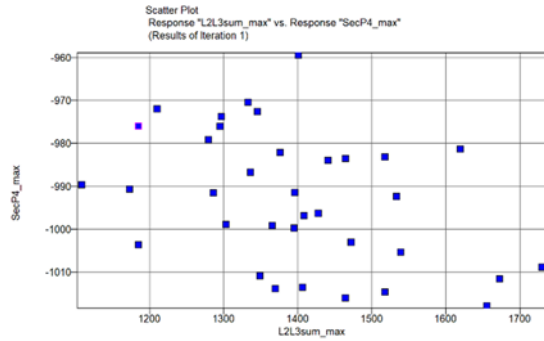
Peak spinal compressive force was more strongly correlated with peak intra-abdominal pressure at higher joint levels (Figure 24), with poor correlation at the L5/S1 joint level.



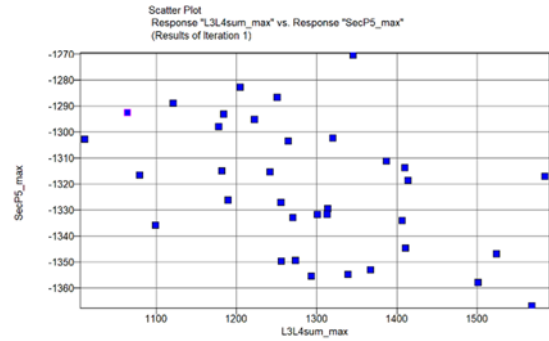
(a)



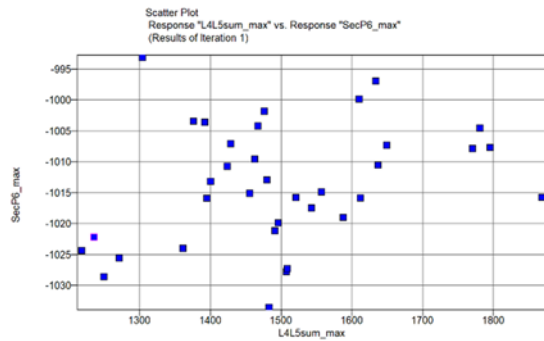
(b)



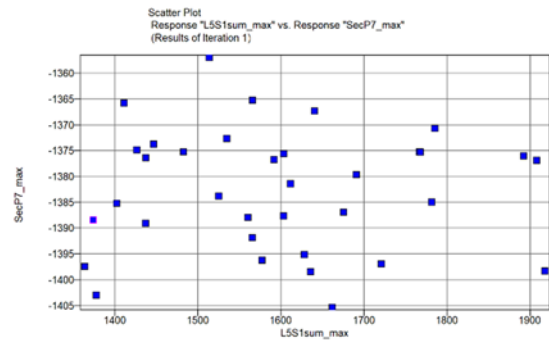
(c)



(d)



(e)



(f)

Figure 24. Peak spinal compressive force has a stronger correlation with peak intra-abdominal pressure at more superior joint levels. Plots indicate peak intra-abdominal pressure vs. peak axial intervertebral disc load for (a) T12L1 (b) L1L2 (c) L2L3 (d) L3L4 (e) L4L5 and (f) L5S1.

Figure 25 shows the linear interpolation of peak intra-abdominal pressure compared to the spinal stiffness parameters in the sensitivity analysis. While overall, these were of the top parameters affecting intra-abdominal pressure response, the strength of the correlation of each parameter is dependent on joint level.

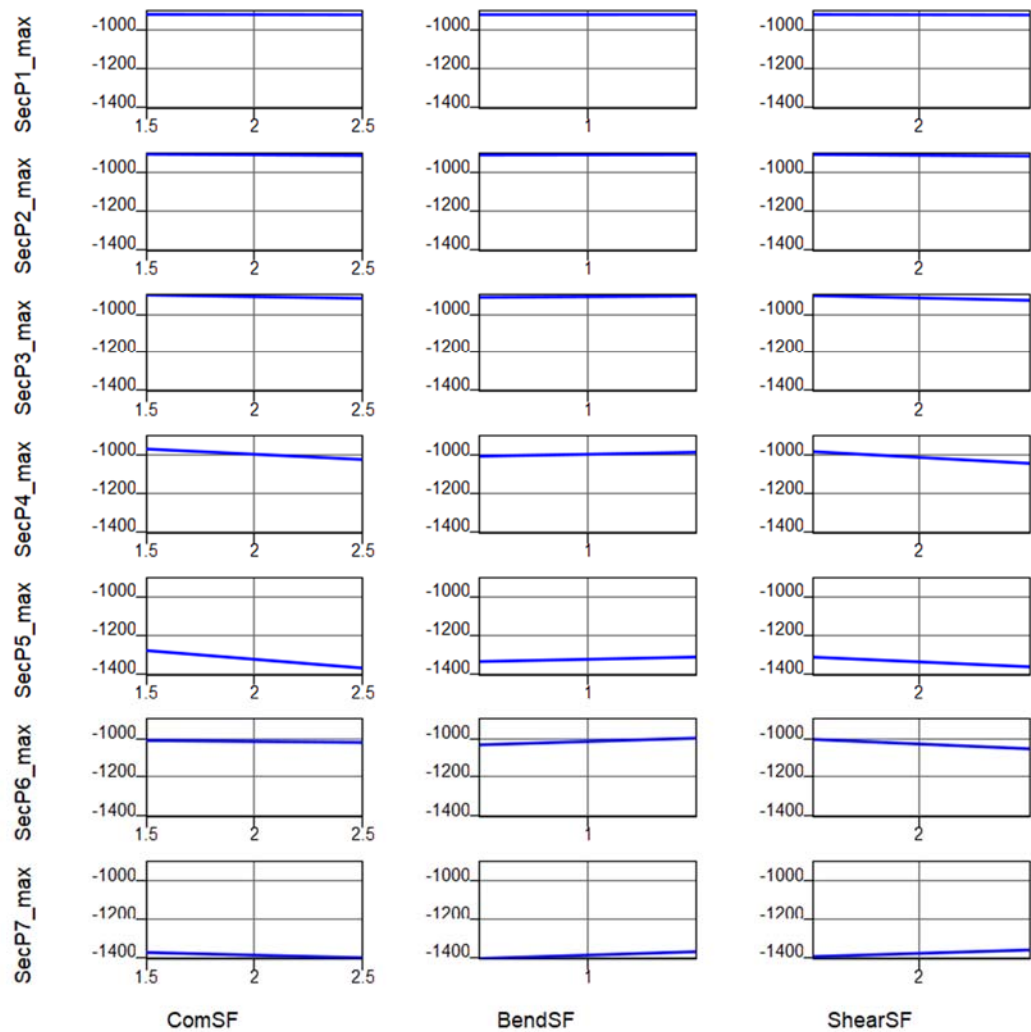


Figure 25. Spine axial (left), bending (middle), and shear (right) stiffness scale factors were of the parameters having the greatest overall effect on peak intra-abdominal pressure (Pa). However, the strength of the correlation for each parameter depended on joint level.

4.4 Discussion and limitations

In general, geometric and material muscular parameters along with spinal stiffness parameters, correlated more strongly with peak intra-abdominal pressure response for both the upper and lower lumbar spine. However, intra-abdominal pressure was most sensitive to axial stiffness in the upper lumbar spine, but most sensitive to bending stiffness in the lower lumbar spine. This is likely due to the increased non-linearity of the L5/S1 bending stiffness compared to the rest of the lumbar spine (Figure 9 in Chapter 2). Other parameters which affect spine bending response include muscle origin and insertion points. These parameters affect the moment arm of the muscle with respect to the spine. Origin and insertion muscle scale factors were found to be more strongly correlated in the lower lumbar spine. Therefore, while the upper lumbar spine response is most sensitive to factors affecting compressive stiffness of the joints, the lower lumbar spine is most sensitive to factors affecting the bending response of the spine.

The intra-abdominal pressure and spinal compressive force were dependent on one another, even while varying muscle related parameters. Higher muscle cross-sectional areas led to higher spinal forces and intra-abdominal pressure in T12/L1. In L5/S1, varying the origin and insertion points of the muscles affect their moment arms, and also the peak spinal forces and intra-abdominal pressure. This supports the

hypothesis that active musculature affects intra-abdominal pressure and its stabilization of the lumbar spine.

Some limitations of this sensitivity analysis were that posture was not investigated, but instead the anteroposterior position of the vertebral bodies were varied in space. This allowed for investigation of the influence of vertebral bodies independently, but not a more flexed or extended posture where these bodies' positions would be dependent on one another. Additionally, the standard deviation of the muscular origin and insertions scale factor was based on the maximum distance to the spine, instead of the displacements in each dimension. This gives a conservative estimate of the influence of muscle origin/insertion, since the maximum distance is larger than the distance in any particular direction. Also, the scale factor was averaged across all muscles. This caused a larger scale factor for some muscles, and smaller for others. Muscle cross-sectional areas were also varied jointly for all muscles. In future work, muscle origin/insertions will be varied by their individual standard deviations. Additionally, a future sensitivity analysis will look at linear order metamodels with interaction effects.

4.5 Conclusions

The interplay between the three components (osteoligamentous spine, abdominal pressure, and active musculature) is complex and both intra-abdominal pressure and active musculature are needed to capture spinal response. While both

muscular cross-sectional area and intra-abdominal pressure affect the model osteoligamentous response, there are interdependences between muscular force or contraction and intra-abdominal pressure. Computational modeling of the lumbar spine should include both intra-abdominal pressure, as well as active musculature. A difference in sensitivity between the upper and lower lumbar spine suggests that modeling efforts need to consider the region of interest in the spine, and acknowledge that level specific properties are important. Future sensitivity analyses will include individual varied muscle cross-sectional areas and origin/insertion variations. This will allow for further understanding of the sensitivity of the model to local model parameters.

5 Computational modeling of underbody blast

5.1 Introduction

A current area of interest in lumbar injury is vertical impact loading. This includes underbody blast (UBB), high speed planing boat impacts, and high-speed aircraft ejection (e.g.[92-96]). Lumbar spine fractures occur in 18% of all wounded in action injuries and 26% of soldier skilled in action exposed to UBB [97]. Of all military musculoskeletal injuries, lumbar spine injuries accounted for 20 percent [98]. Additionally, the lumbar spine is likely the primary load path for injuries to the head and neck in vertical impact loading conditions. Typically, these impacts happen on the order of a few to a couple hundred milliseconds and 15 g's or higher. Furthermore, the US military has moving towards including women in all combat roles, including as the Special Forces beginning in January 2016 [99]. Even after scaling stresses using surface anthropometry, men and women exhibit differences [5]. It is unknown how women will respond biomechanically in these loading conditions.

Recent research has investigated underbody blast both experimentally (e.g. [93 100 101]) and computationally [102]. The US Army has focused efforts on the development of an anthropometric test device (ATD) called the Warrior Injury Assessment Manikin (WIAMan) for underbody blast loading [103 104]. While experimental research has driven determination of biomechanical properties of the WIAMan ATD, a computational model can provide insight without the need for many

cadaveric tests. Additionally, a lumbar computational model for UBB that can be scaled to different sizes and sexes may provide useful understandings for the future direction of experimental research. While many lumbar models were available, no previously developed model was appropriate for high-rate vertical impact loading with both intra-abdominal pressure and active musculature included. While it is known that the lumbar spine is viscoelastic, the properties at high-rates, such as those experienced during UBB events, have only recently been investigated [105]. To this end, a computational lumbar model was created to investigate high-rate loading. The scope of this project is to investigate lumbar spine response to single accelerative loading impacts (3G-15G), such as those seen in military settings- high speed craft impacts, ejection seats, underbody blast.

It is hypothesized that the use of active musculature decreases injury tolerance in compressive loading. A tensed muscle response may contribute 40% or more of the compressive tolerance of the adult and pediatric neck [69]. This hypothesis is tested using two sets of simulations. First, the model force and moment response from the Duke UBB failure simulations will be compared to against the experimental corridors (see Figure 27 and Figure 37) from cadaveric tests currently being conducted at Duke University. It is hypothesized that the muscle activations will increase pre-compression in the osteoligamentous spine. Therefore, the simulations with muscle activations will lie farther from the experimental corridor (which have no active musculature). They

should also lie closer to the injury risk threshold, due to pre-compression in the osteoligamentous spine.

5.2 Methods

5.2.1 Experimental data collection

The osteoligamentous portion of the 50th percentile male model is validated using high rate vertical impact loading tests conducted at Duke University (unpublished data). These tests are whole spine osteoligamentous compression tests meant to simulate underbody blast. The spine was potted in a fixed-fixed end condition in a posture representative of a seated soldier [85] with a neutral lordotic posture. The caudal end was loaded via displacement control to nominal loading rates of 200, 400, and 600 N/ms, and then to failure. Six degree of freedom load cells were used to acquire upper (T12/L1) and lower (L5/S1) lumbar force and moment responses. Also captured was sacral displacement via an LVDT, and upper, lower, and mid lumbar accelerations with a three degree of freedom accelerometer.

5.2.2 Osteoligamentous model validation and active musculature simulations

The mean axial displacement profile from the experimental tests (Figure 26) was applied to the sacrum of the model. As in the experimental test, T12 was held fixed in both translation and rotation. The sacrum was free to move axially, but not in along the anteroposterior and lateral axes. Rotation was restricted for all degrees of freedom. The

remaining vertebral bodies (L1 through L5) were restricted to movement in the sagittal plane.

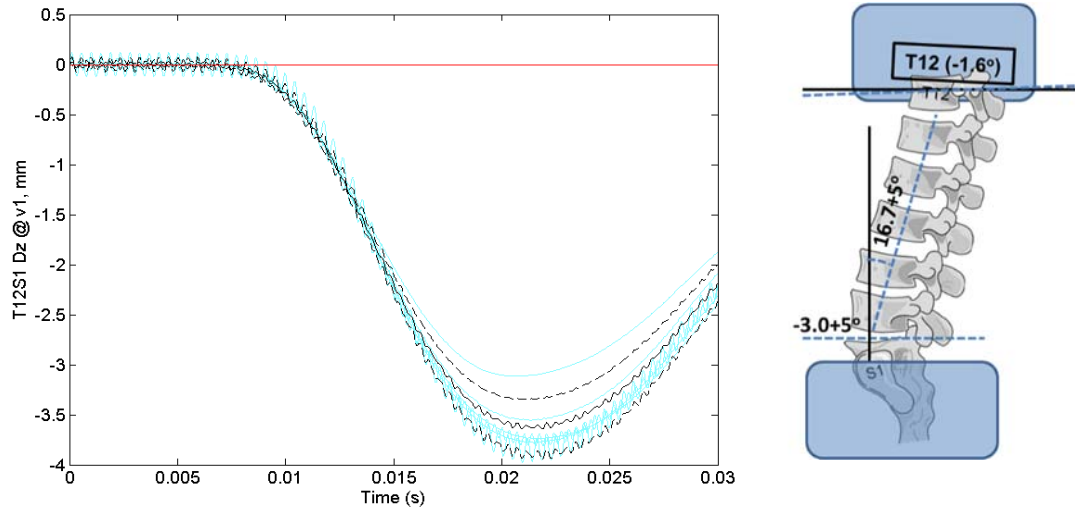


Figure 26. Experimental axial displacement for subfailure test (Duke, unpublished data) (left), and experimental setup (right).

First, the osteoligamentous model was chosen for model validation. The lower rate (200 N/ms) test was validated against the T12/L1 axial force corridor (Figure 27).

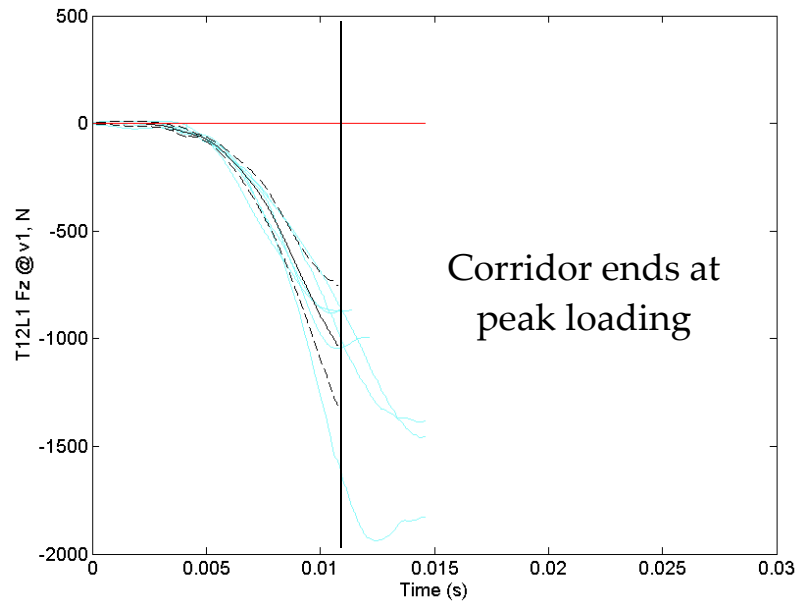


Figure 27. T12/L1 axial force corridor for 200 N/ms underbody blast loading (Duke, unpublished data). Compression is negative.

This corridor was developed from the mean plus or minus a standard deviation from the upper lumbar spine load cell. The corridor ends at peak force, as the loading region is of particular interest. The T12/L1 joint load cell was chosen for validation over the lower lumbar load cell because no mass compensation was needed for the experimental results. This results in a higher confidence in the experimental data for T12/L1. The failure test was validated against a force-energy curve (Figure 28), and the injury risk curve detailed in Chapter 3 (Figure 12).

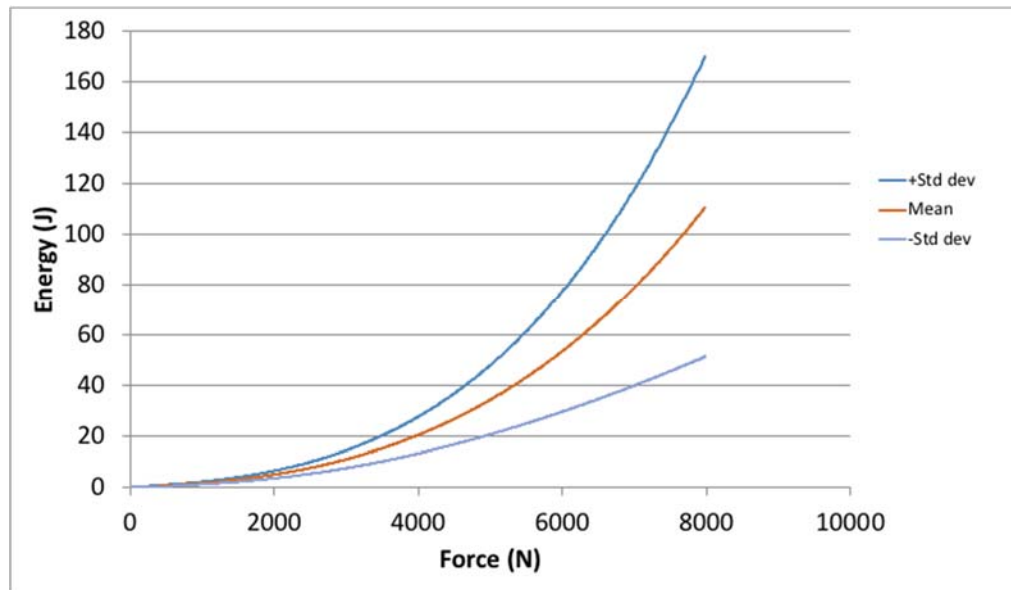


Figure 28. Strain energy as a function of force for 29 cadaveric lumbar failure tests. Lumbar spines were potted in a neutral lordotic posture plus/minus one standard deviation, and loaded axially through displacement control of the sacrum (Duke, unpublished data).

The force-energy curve was generated from the mean and plus or minus one standard deviation from 29 experimental lumbar tests. Energy was calculated as the integral of the T12/L1 axial force with respect to sacral displacement (Equation 6), and so represents the strain energy of the lumbar spine.

$$E = \int F_z dz \quad (6)$$

The mean and standard deviation curves were calculated across the curves for all spines extended through the mean injury load of 4929 N. Figure 29 shows the 50th percentile male strain energy response to force, and two scaled female responses. This response shows the 85th percentile female is a comparable model to the 50th male. Force

was scaled by area while compressive strain energy was scaled by the product of vertebral area and length.

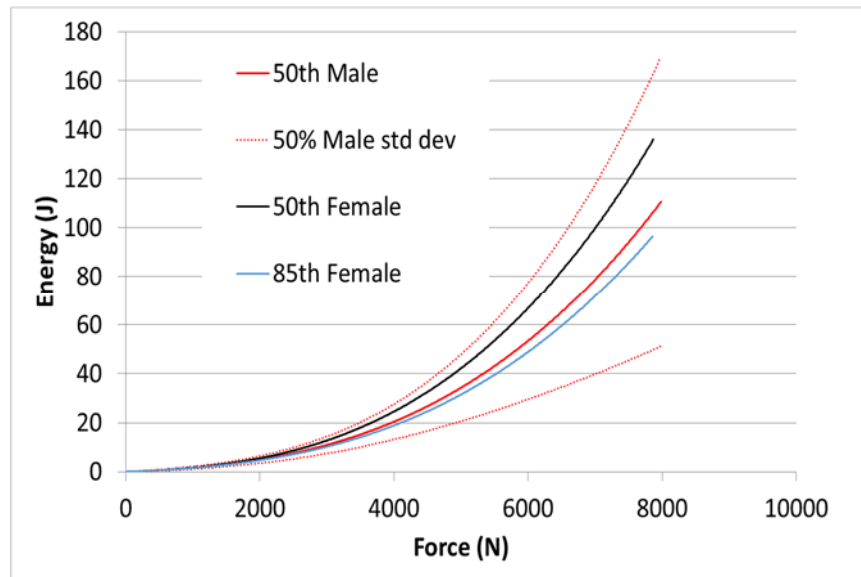


Figure 29. Compression energy with respect to force for 50th percentile male, 50th percentile female, and 85th percentile female (Bass, unpublished data)

An injury risk curve for lumbar spinal fracture from axial loading (Figure 12) was generated from underbody blast failure tests for a nominal posture plus or minus a standard deviation of the posture (Duke unpublished data). The force at failure for these 29 lumbar spine experiments were used to create a survival plot from T12/L1 axial force at fracture using a Weibull fit.

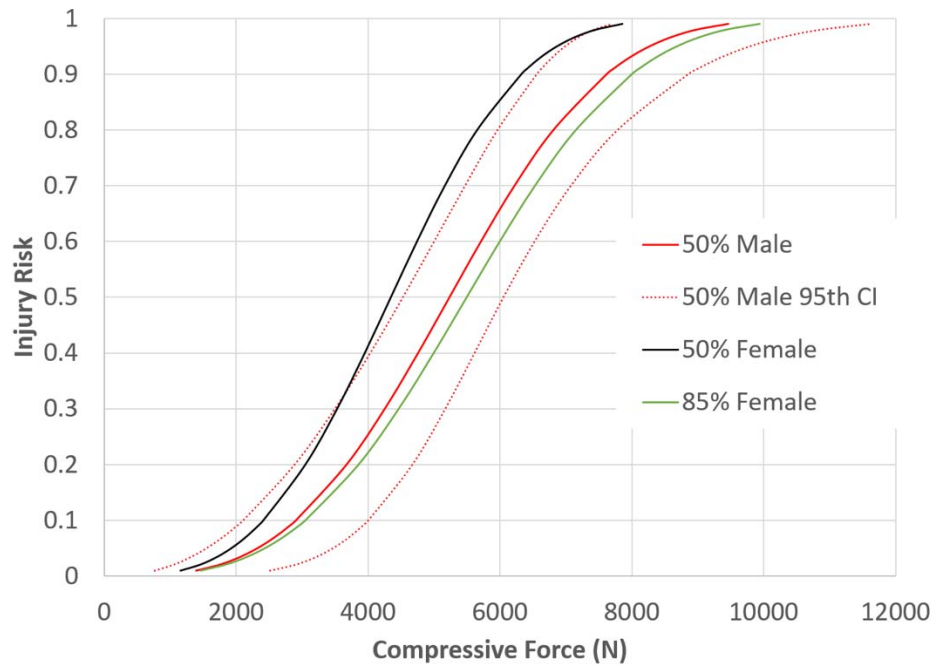


Figure 30. Injury risk curve for 50th percentile male, 50th percentile female, and 85th percentile female. Confidence intervals not included for 50th and 85th female for clarity (Bass, unpublished data).

Figure 30 shows the injury risk for a 50th percentile male, 50th percentile female, and 85th percentile female. The curves demonstrate that while the risk for the 50th female and 50th male differ considerably, the injury risk for the 85th percentile female is closer to the 50th percentile male due to closer dimensions of these two demographics. Force scaled by vertebral area. Schmidt, et al. [5] was used to obtain the 50th percentile female vertebral loading area from 50th percentile male dimensions and the 85th percentile female was found using the normal population area regression from Korpinen, et al. [106]. This regression model yielded a vertebral area for the 85th female which was very

close in size to the 50th male. Male and female response can be compared to their respective injury risk curves.

Finally, the relaxed and tensed muscle activation states were simulated for both the 200 N/ms and failure loading conditions. The relaxed and tensed muscle activations were detailed in Chapter 3. The dynamic lumbar spine responses are compared by activation state, or lack thereof. Finally, an 85th percentile female model was simulated in the low rate case using the male relaxed activation state. The creation of the 85th percentile female model is detailed in Chapter 2.

5.3 Results

5.3.1 Validation

In the subfailure underbody blast simulation, peak compressive force in the T12/L1 joint was 924 N, and occurs at 0.012 s. While the validation corridor is for only T12/L1, computational modeling gives insight into the loads seen between those that can be measured experimentally. For example, in the experimental setup, only T12/L1 and L5/S1 axial force could be measured. But here, the axial force in L1/L2 through L4/L5 are also determined.

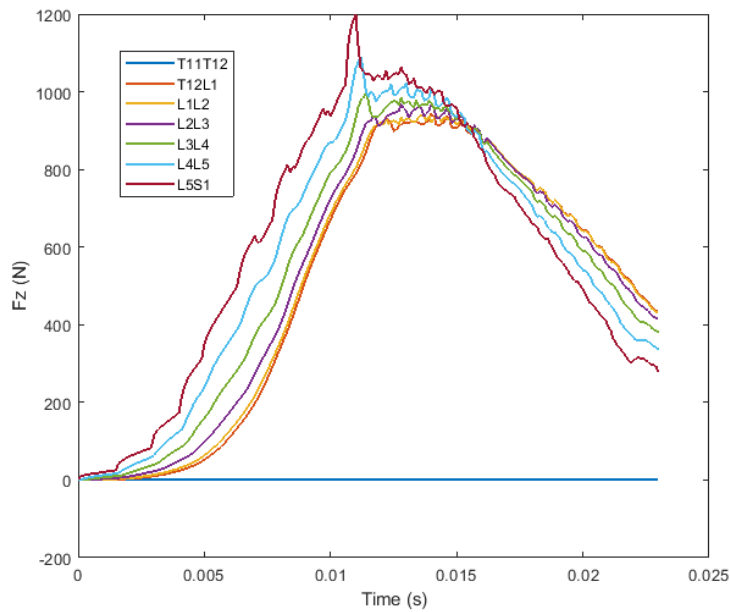


Figure 31. Compressive forces in the lumbar spine for an approximately 3 mm sacral impact are between 930 and 1200 N. Compressive force increases from the superior to inferior direction.

This peak compressive force is within the experimental corridor, indicating the model is valid for lower rate (200 N/ms) vertical impact simulations. Figure 32 shows the axial force/displacement curves for this subfailure simulation. While sacral displacement is on the order of 3 mm, each vertebral joint compress approximately 10 percent of the total spinal compression. There is slightly more compression (.05 mm) in the L5S1 joint.

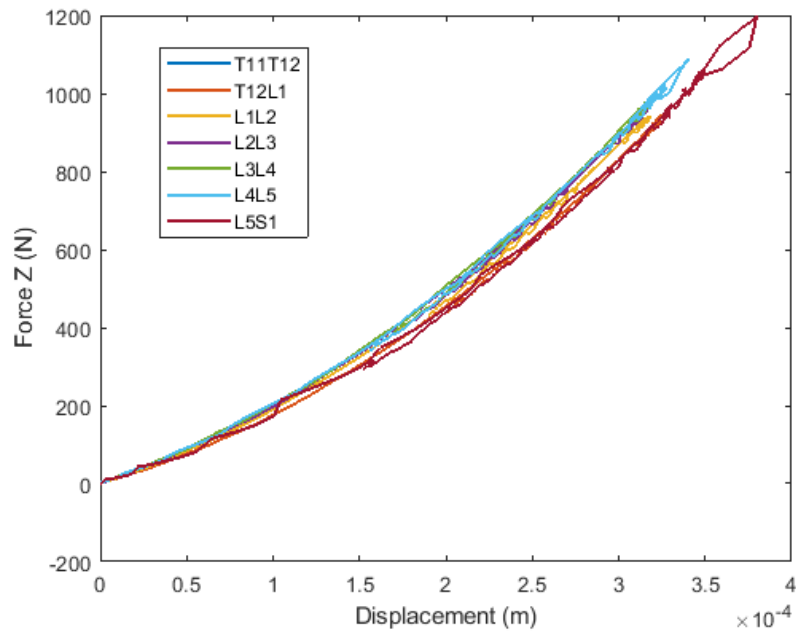


Figure 32. Axial force displacement curves of the intervertebral joints during subfailure underbody blast.

For failure response, strain energy as a function of axial force is a better indicator of model response to experimental data than model force over time. It decouples the response from time, and paints a picture of lumbar displacement coupled with force. The failure energy corridor in Figure 30 was developed from 29 failure tests of cadaveric lumbar spines in a neutral posture plus or minus one standard deviation. The 50th percentile male model energy response lies within the corridor, but slightly above the mean response.

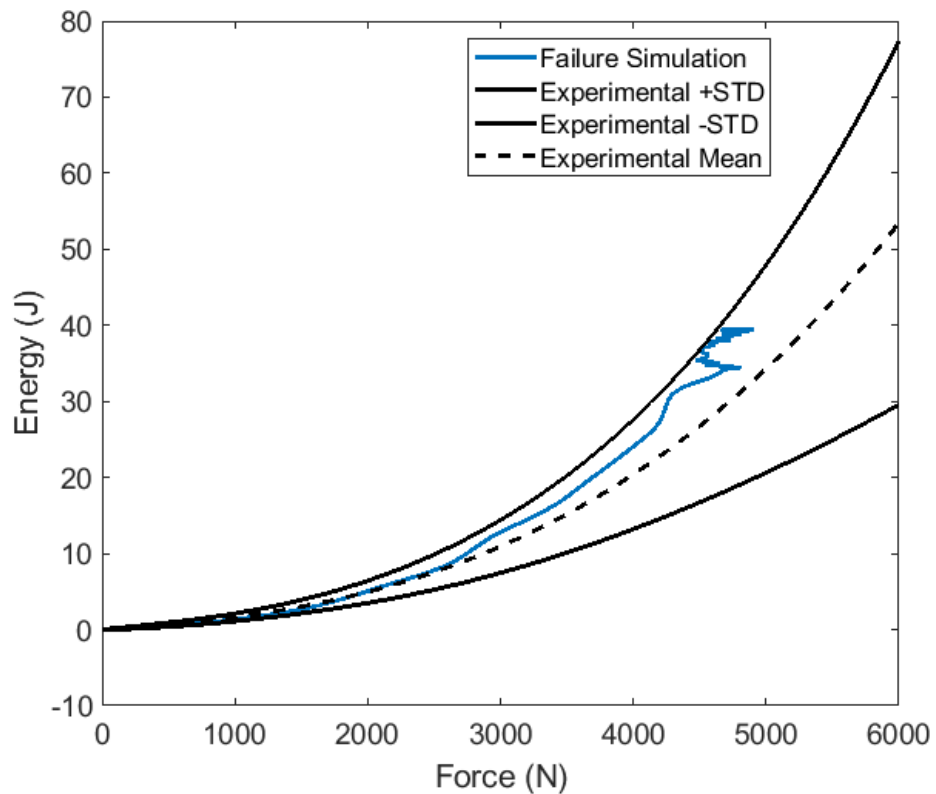


Figure 33. Model simulation strain energy response compared to experimental corridors shows the lumbar model can be used for modeling failure .

Peak model strain energy occurs at 4809 N and 34.5 J. When compared to the 50th percentile male injury risk curve, this represents a 41% risk of spinal fracture, but within the 95th confidence intervals for a 50th percentile risk of injury. The compressive force time histories for all vertebral joints is shown in Figure 34. Compressive force increases as you move inferiorly down the lumbar spine. Of interest for this study is the loading portion of the underbody blast profile, up to maximum force. Here, forces decrease after approximately 12 ms because the sacrum begins to return to its initial position (see Figure 26).

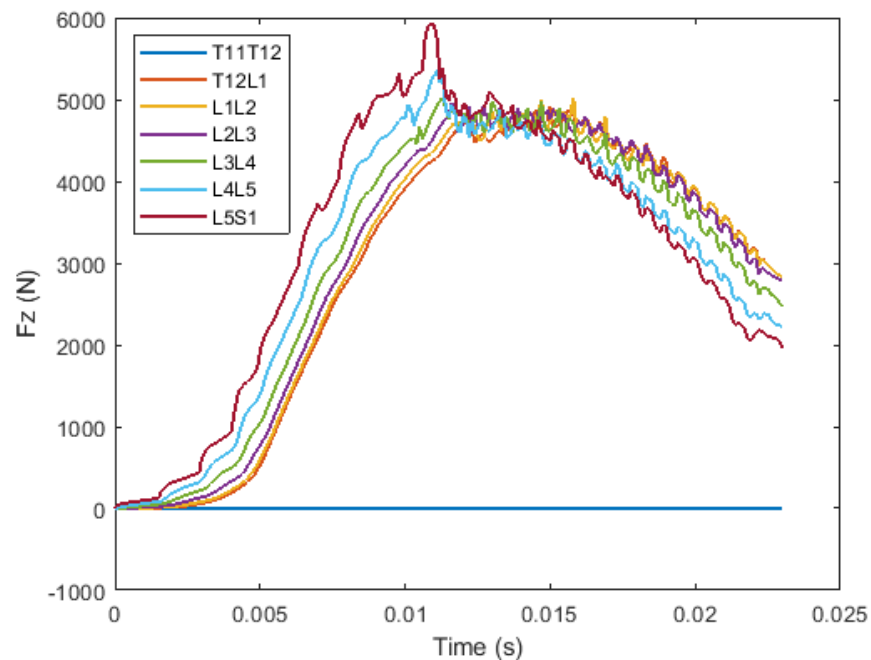


Figure 34. Underbody blast failure simulation axial compressive force by joint level. T11/T12 was held fixed, and compressive force in the spine increases in the caudal direction.

Failure shear loads were also highest for the lower lumbar spine joints (Figure 35), reaching peaks of 1600 N in L5/S1. There are phasing differences between the intervertebral joints in shear, and magnitude does not increase with each subsequent joint level while traveling inferiorly. The L4/L5 joint, as well as the L5/S1 joint first move into anterior (positive) shear, and then cross into posterior (negative) shear. All other joints are in posterior shear for the entire loading profile.

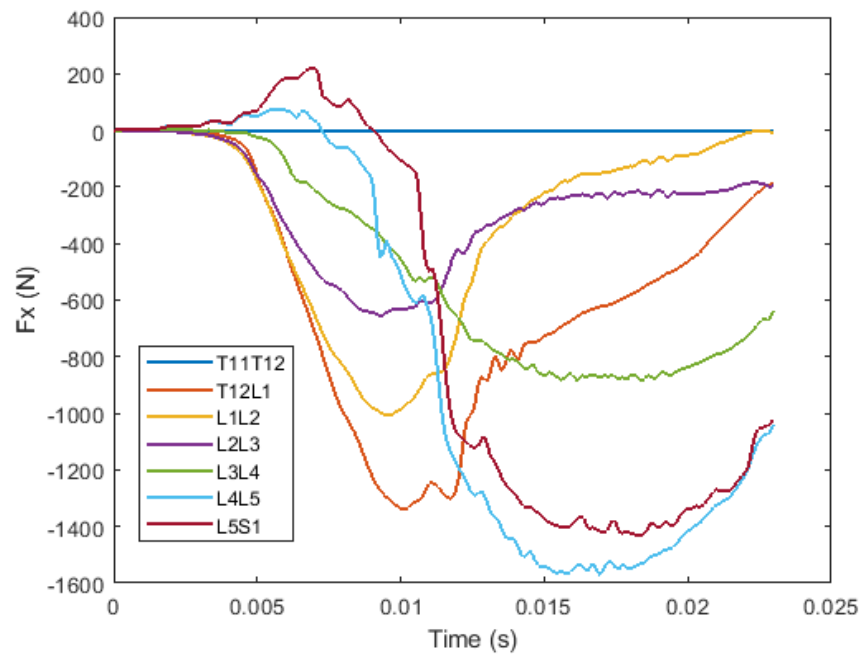


Figure 35. There is a phase lag between the shear responses of the intervertebral joints. The two lowest FSUs first go into anterior (positive) shear, while all other joints immediately go into posterior (negative) shear.

The bending moments (Figure 36) for all joint levels are low (<1 Nm), and are less than the moments seen in the experimental tests (Figure 37). T12/L1, L1/L2, and L5/S1 have a slight extension bending moment, while L2/L3 through L4/L5 have a small flexion bending moment. Overall, there is minimal bending in the model during underbody blast.

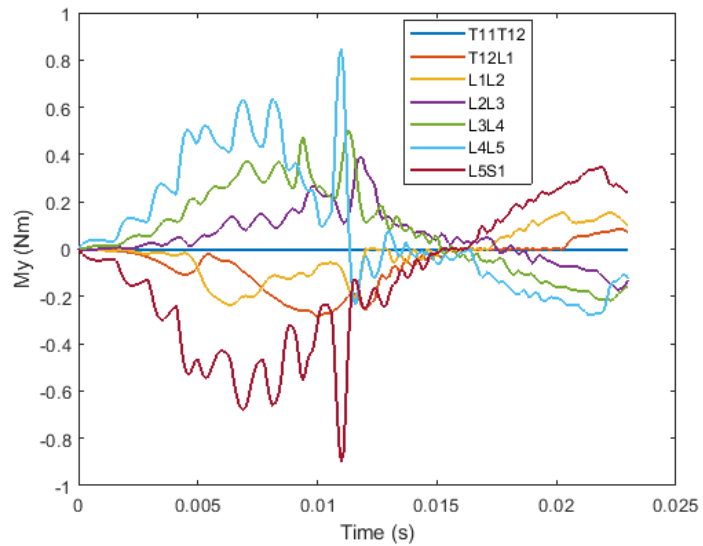


Figure 36. Bending moments at the joints' CORs for the lumbar spine are small during vertical impact. Upper lumbar spine segments and L5/S1 move into extension (negative), while the mid lumbar spine segments (L2/L3 to L4/L5) moves into flexion (positive).

However, the experimental tests have a very wide corridor and were found to be very sensitive to the position where the moment was taken, since moments had to be translated from the load cell to joint centers.

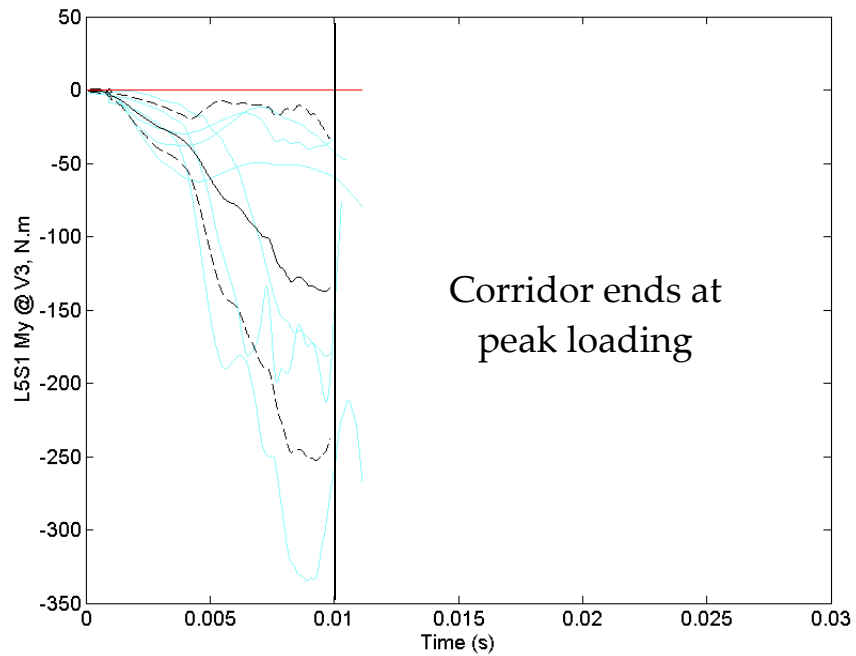
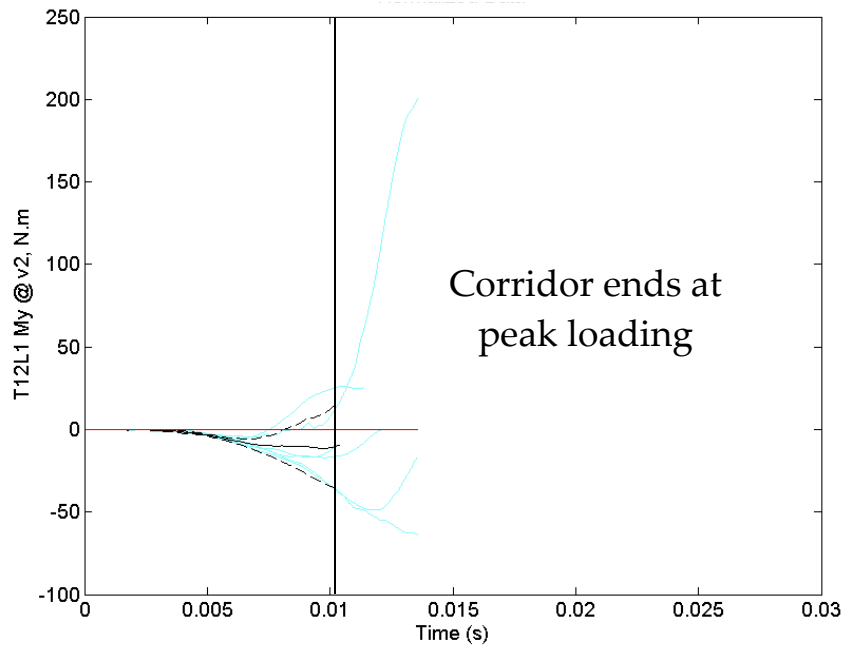


Figure 37. Experimental underbody blast moment response for the upper lumbar spine (top), and lower lumbar spine (bottom). The upper lumbar spine corridor runs close to zero, while the lower lumbar spine has a negative response with a wide corridor (Duke, unpublished data).

5.3.2 Muscle activations and sex comparisons

The inclusion of active musculature, and the abdominal pressure decrease the compressive force in the spine (Figure 38). This is because the inclusion of the soft tissue allows for an alternative load path. Additionally, loading occurs earlier in time. Peak compressive loads occur at 9.2 ms versus 11 ms for the osteoligamentous spine.

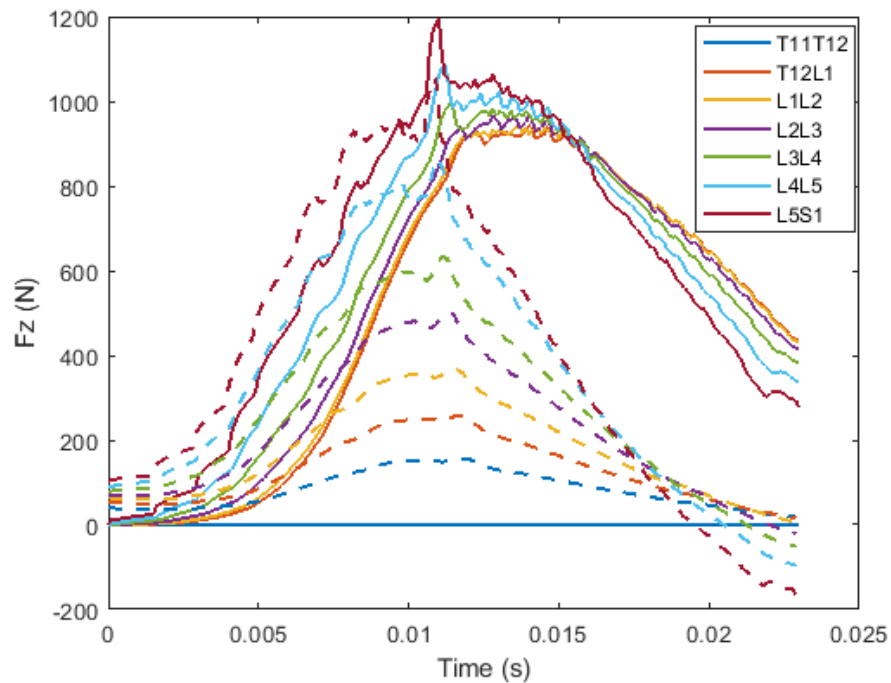


Figure 38. Full lumbar model with active muscles decrease the axial compressive load of the lumbar spine. Solid lines represent the osteoligamentous model, while dashed lines are the full model with relaxed activated muscles.

When comparing the relaxed to tensed activation states, spinal axial forces increase dramatically. Peak T12/L1 force in the tensed activation simulation is 2487 N, compared to 245 N in the relaxed case. This is a 10x increase in spinal force. In the

tensed case, the T12/L1 spinal force is 47 percent of the estimated compressive failure load. This agrees with results for a tensed case in the cervical spine, which saw 45 percent of compressive preloads [69].

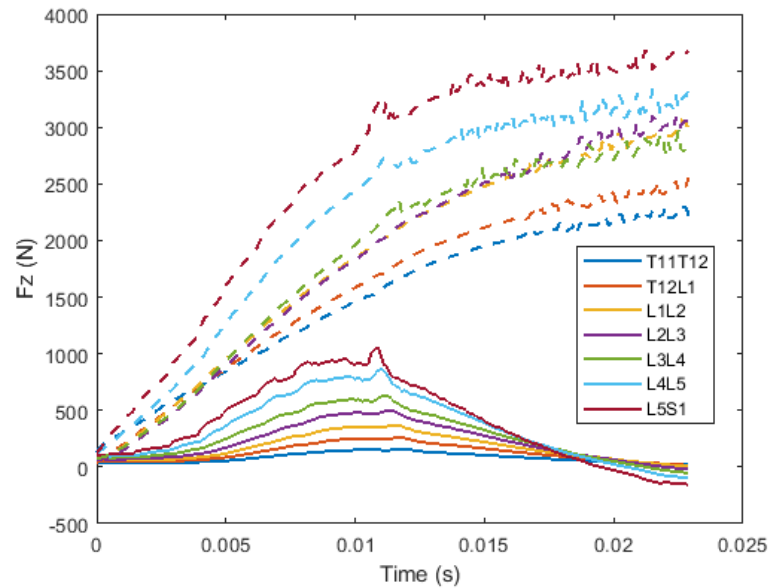


Figure 39. Tensed activations (dashed) result in substantially higher axial forces in the lumbar spine compared to non-tensed (solid) activations.

A preliminary female 85th percentile model was compared to the 50th percentile male model for the 200 N/ms loading condition with relaxed muscles. The female model resulted in higher spinal loads for the same loading condition (Figure 40). Peak T12/L1 force for the female model (1266 N) was almost five times higher than the male model (258 N). These differences were greater at lower lumbar spine levels. For both models, these results are subinjurious (less than 1 percent risk of injury from Figure 29).

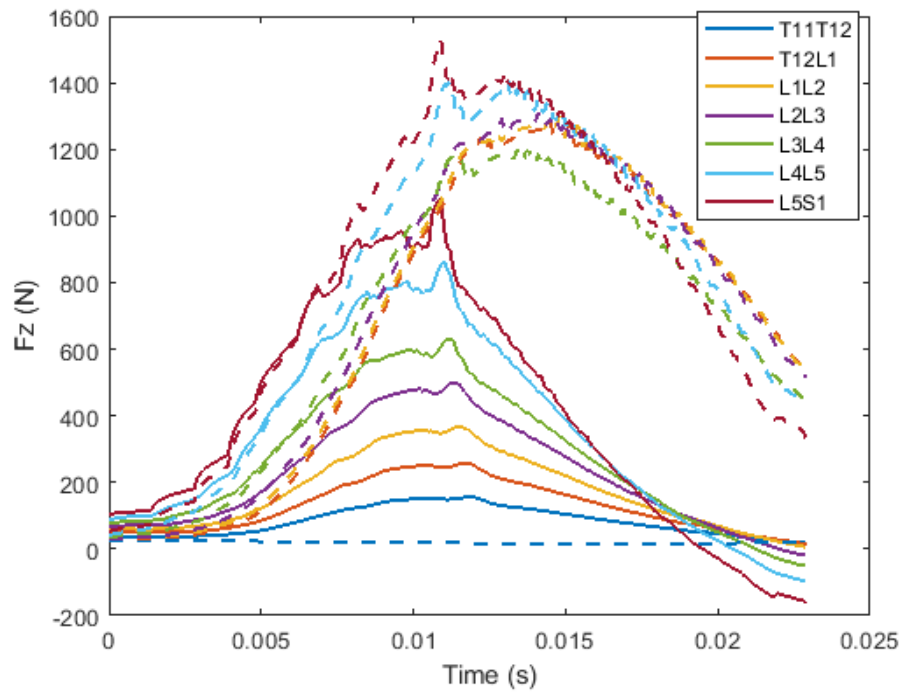


Figure 40. Comparison of male (solid) and female (dashed) models of matched mass and including active musculature. Compressive forces in the lumbar spine are higher in the female model.

5.4 Discussion and limitations

At lower forces, the model stays closer to the mean strain energy (Figure 33). However, at higher force levels, the lumbar model increases in energy at a higher rate than the mean experimental data. While the model is still validated against experimental response for a neutral lordotic posture for axial force and strain energy, this may result high spinal displacement at higher spinal forces relative to the force/displacement ranges investigated here. A sensitivity analysis of the model posture

would better indicate over what range of positions in which this model is valid. This was outside the scope of this dissertation, which only focused on neutral posture. The lumbar model may slightly underpredict lumbar spine injury based on experimental data. However, the injury risk for the computational lumbar results in a risk that falls within the 95th confidence intervals for a 50th percentile risk of injury. Therefore, this model is valid from low rate vertical impacts up to high rate tests, and failure loading.

The bending moments for all joint levels are low (<1 Nm), and are less than the moments seen in the experimental test. However, the experimental tests have a very wide response corridor and were found to be sensitive to the position where the moment was taken, since moments had to be translated from the load cell to joint centers. Therefore, lumbar bending moment is not recommended for a validation criterion. While bending response is of interest in the lumbar spine, the lumbar spine is more of a stacked column than the cervical spine. Therefore, lumbar loading should have more axial compression and less sagittal bending than the cervical spine.

The female model used in this study used lines of action scaled from the male model. A 50th percentile male relaxed activation state was applied to the 85th percentile female model. The difference in response between the two sexes suggests that muscle recruitment for women is different than men. An optimization for a female relaxed and tensed case should be performed separately in future efforts. Additionally, while only a sub-failure simulation was compared, there was still an order of magnitude difference

between the peak male and female response. For higher rate tests, this may result in the female model reaching fracture injury threshold prior to the male model for the same input.

A full lumbar spine model including intra-abdominal pressure and active musculature decreases compressive loads in the spine when compared with an osteoligamentous model. Increasing muscle activation from the relaxed to the tensed states increases the axial load in the lumbar spine when only looking at a whole lumbar/abdominal model.

5.5 Conclusions

The lumbar osteoligamentous model developed in this dissertation was validated for both sub-failure and failure loading conditions in vertical impact loading. A relaxed lumbar spine model has decreased vertebral joint axial loads compared to the osteoligamentous model. However, when looking at a human response instead of a cadaveric response, increasing muscle activations increased the compressive load in the intervertebral joints an order of magnitude for the tensed case over the relaxed case. Peak compressive force in the subinjurious simulation increased from a less than 1% risk of injury to a 6% risk of injury. However, this is a load increase of over 2000 N, and represents 47% of the compressive failure load in T12/L1. This supports the hypothesis that active musculature increases pre-compression in the osteoligamentous spine, and pushes the lumbar axial response closer to the injury risk threshold. The female lumbar

spine had increased spinal compressive loads compared to the male model with the same activation state. Female models with active musculature should be optimized for their own relaxed and tensed states, instead of applying those from a male model.

6 Sex Effects and injury risk for muscle tetanus

6.1 Spinal injury risk from muscle tetanus

The advent of convulsive therapy to treat mental illness in the 1930s - 1950s resulted in spine fractures in numerous cases [16 17]. Typical techniques used to induce convulsions included administration of metrazol[107], insulin [108], or electroconvulsive therapy [109]. Typical side effects included Vertebral body compressive fractures in thoracic spine, most commonly in thoracic vertebrae, T4-T6 [16].

The available multiple-patient epidemiology studies span a period from 1939 to 1955, including studies performed before widespread use of paralytics such as curare for convulsive therapy (e.g. Bennett, 1940) [110]. Without a paralytic, typical full torso and other muscle activation is seen, inducing vertebral fractures and muscle tearing [111]. Of the 23 epidemiological studies of spinal fractures that were identified from convulsions, including fractures resulting from epileptic seizures (grand mal), 19 investigated the incidence of fracture in electroshock therapy, convulsive therapy with metrazol, or insulin shock, without a muscle relaxant or paralytic. Interestingly, based on raw incidence when men are separated from women in the available studies, spinal fractures from convulsive therapy or seizure occurred in at a higher rate in men ($359/1058 = 33.9\%$) than in women ($230/1204 = 19.1\%$). This may be due, in part, to differential torso muscle cross sectional areas in women relative to men relative to the spinal vertebral cross sectional area.

Table 12. Studies of spinal fracture from convulsive therapy and grand mal epileptic seizures. Dashes indicate missing data. C=cervical, T=thoracic, L=lumbar, m=male,f=female.

Study			Incidence									
Author	Yr	Modality	n	fx	Fx %	C	T	L	m	f	male w fx	f w fx
Androp[112]	1941	Metrazol	30	7	23%	-	-	-	-	-	6	1
Barrett[113]	1942	Electroshock	20	3	15%	0	3	0	10	10	3	0
		Metrazol	20	9	45%	0	9	0	10	10	6	3
		Epilepsy	20	9	45%	0	9	0	10	10	4	5
Bennett, Fitzpatrick[114]	1939	Metrazol	17	8	47%	0	8	0	3	14	1	7
Cummins[115]	1942	Metrazol	122	18	14%	0	18	0				
Dewald[17][20]	1954	ECT (Glissando)	120	23	19%	0	23	0	33	87	11	12
		ECT (direct)	111	25	23%	0	25	0	23	88	13	12
Easton, Sommers[116]	1942	Metrazol	200	46	23%	0	46	0	84	116	24	22
Easton[16][19]	1944	Metrazol	800	209	26%	0	209	0	366	433	136	73
Graves, Pigmataro[117]	1940	Metrazol	187	15	8%	0	15	0	-	-	-	-
Krause[118]	1941	Metrazol	75	32	43%	0	31	1	33	42	19	13
Lingley[119]	1947	Electroshock	230	53	23%	-	-	4	94	136	35	18
Newbury, Etter[120]	1955	ECT	85	23	27%	0	23	0	20	65	4	19
Pederson [121]	1976	Epilepsy	87	14	16%	-	-	-	55	32	9	5
Polatin[122]	1939	Metrazol	51	22	43%	0	22	0	23	35	6	16
Pool, Meschan[123]	1952	Insulin, no prev therapy	46	6	13%	0	6	0	46	0	6	0
		Insulin, prev ECT or metrazol	53	10	18%	0	10	0	53	0	10	0
		Insulin + ECT (no prev)	32	8	25%	0	8	0	32	0	8	0
		Insulin + ECT (prev)	35	6	17%	0	6	0	35	0	6	0
Schatz, Konwaler[124]	1941	Metrazol	66	19	29%	0	19	0	38	28	-	-
		Epilepsy	10	5	50%	4	1	0	10	0	5	0
Smith[125]	1942	Electric Shock	156	5	3%	0	5	0	-	-	-	-
Reed, Dancey[126]	1940	Epilepsy	72	25	35%	0	25	0	32	40	15	10
		Metrazol + Insulin	86	27	31%	0	27	0	36	50	18	9
Vasconcelos [127]	1973	Epilepsy w/o back pain	70	11	16%	0	10	3	38	32	8	3

		Epilepsy w back pain (from 1427 patients)	15	15	100%	0	15	6	12	3	12	3
Worthing, Kalinowsky [128]	1942	Electric Shock	60	0	0	-	-	-	-	-	-	-
		Epilepsy	45	2	4%	-	-	-	-	-	-	-

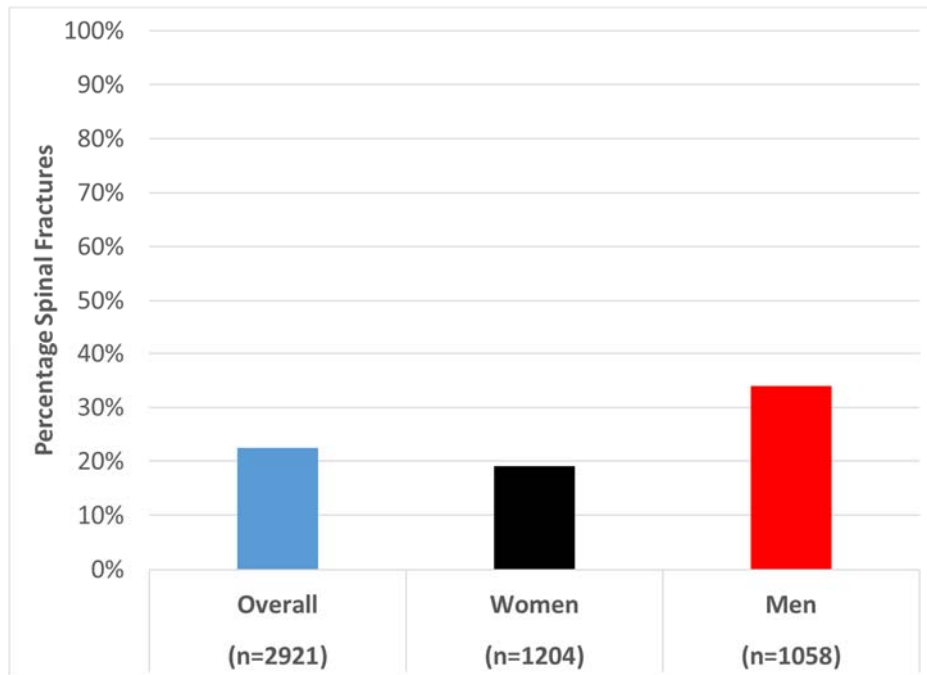


Figure 41. Percentage spinal fractures in patients being given convulsive therapy without a muscle relaxant or paralytic, using metrazol shock, insulin shock, electroshock, or tonic-clonic seizure, overall and by sex.

Where reported (n=2454), the location of spinal fracture in patients was in the thoracic spine (n=558) in the vast majority of patients (Figure 42). Cervical (n=4) and lumbar fractures (n=14) were rarer. Though Vasconcelos (1973) reported a 47% risk of lumbar fractures in a subset of grand mal epilepsy patients (n=15), these were a subset reporting pain selected from a cohort of 1487 patients. Since no other patients were

examined for spinal fractures, the true incidence in this study may be larger than the implied incidence in the study (1%).

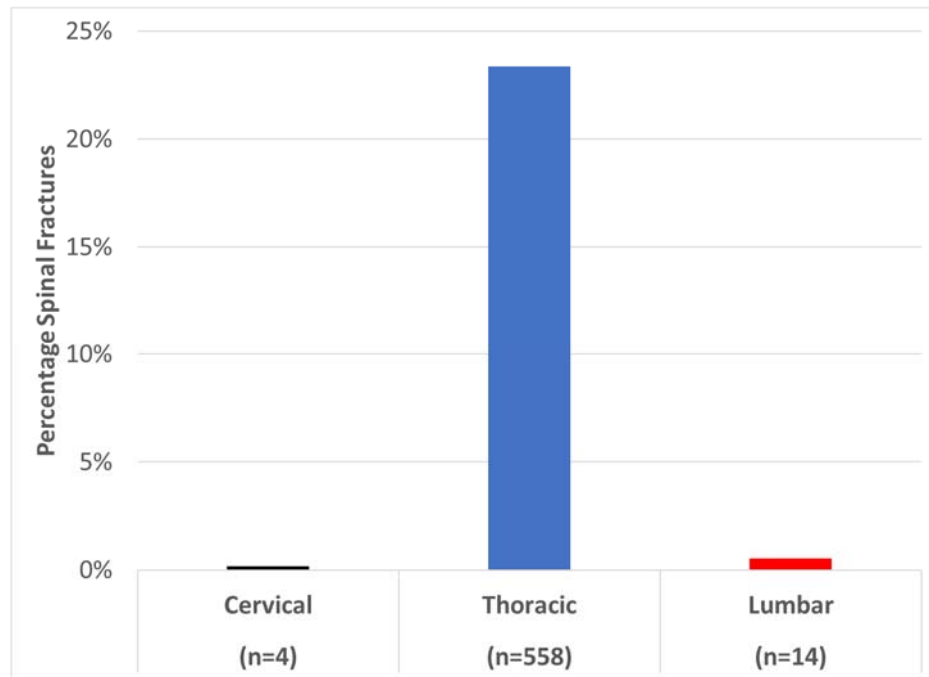


Figure 42. Location of spinal fractures by region in patients being given convulsive therapy without a muscle relaxant or paralytic, using metrazol shock, insulin shock, electroshock, or tonic-clonic. Lumbar fracture numbers include results from Vasconcelos (1973) [127].

6.2 Scaling men and women for date of study

Among the potential causes of the difference between risk of spinal fracture from muscle tetanus reported in the convulsive therapy and epilepsy literature is a relative difference in muscle cross sectional area relative to abdominal and spinal support. Men typically have larger PCSA values than women increasing risk of spinal fracture under full muscle activation, but women have potentially offsetting decreases in spinal disc and vertebral body area and in abdominal cross sectional area relative to men.

One potential confounding factor in using data from the 1940's to assess the current population risk is differences in anthropometry between the two periods. The mean stature in 18 year old men and women is shown in Figure 43. Between 1939 and 2014, the mean stature of men has significantly increased ($p<0.01$) 3.2 ± 1 cm while the mean stature of women has increased 3.1 ± 1 cm. This is a 1.7% difference in stature for men and a 1.8% difference for women. Body mass, too, has increased significantly ($p<0.01$) in the interval between 1940 and 2010 as shown in Figure 44. The mean body mass of men has increased 16.6 ± 0.7 kg while the mean mass of women has increased 17.3 ± 0.6 kg. This is a 19.2% difference in mass for men and a 23.2% difference women. These large differences in mass, and consequent increases in muscle PCSA, may drive increases in risk relative to the smaller increases in structural anthropometry.

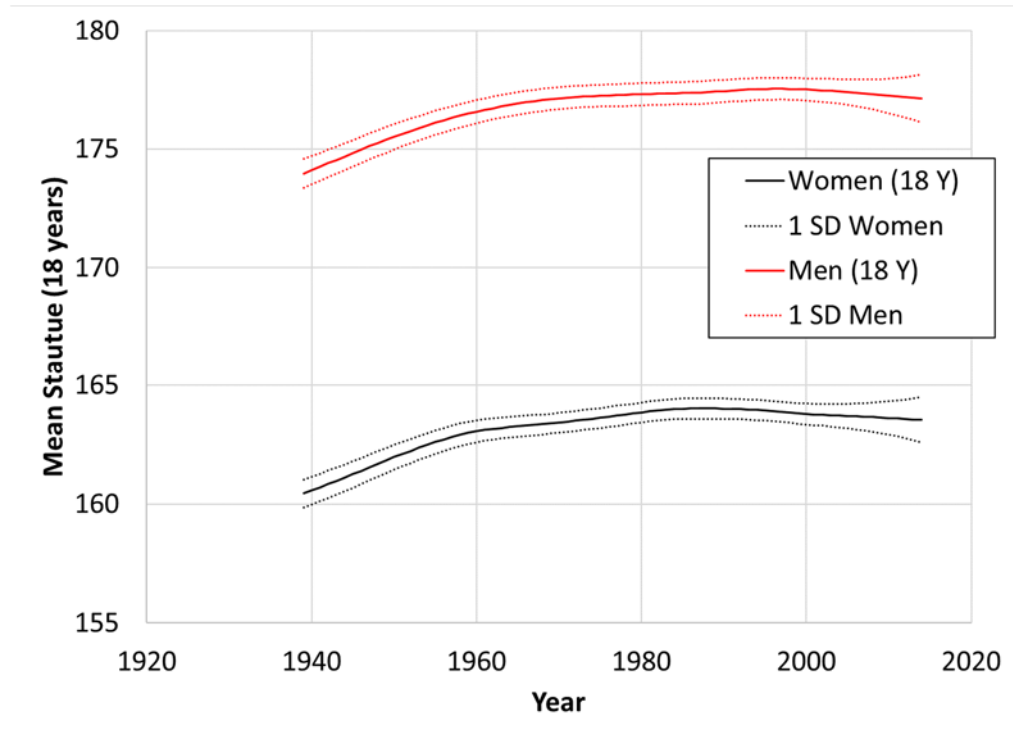


Figure 43. Stature of 18-year-old men and women by age from 1939-2014 [129] shows that the average stature of men has increased 1.7% from 1939 to 2014. The average stature of women has increased 1.8% from 1939 to 2014.

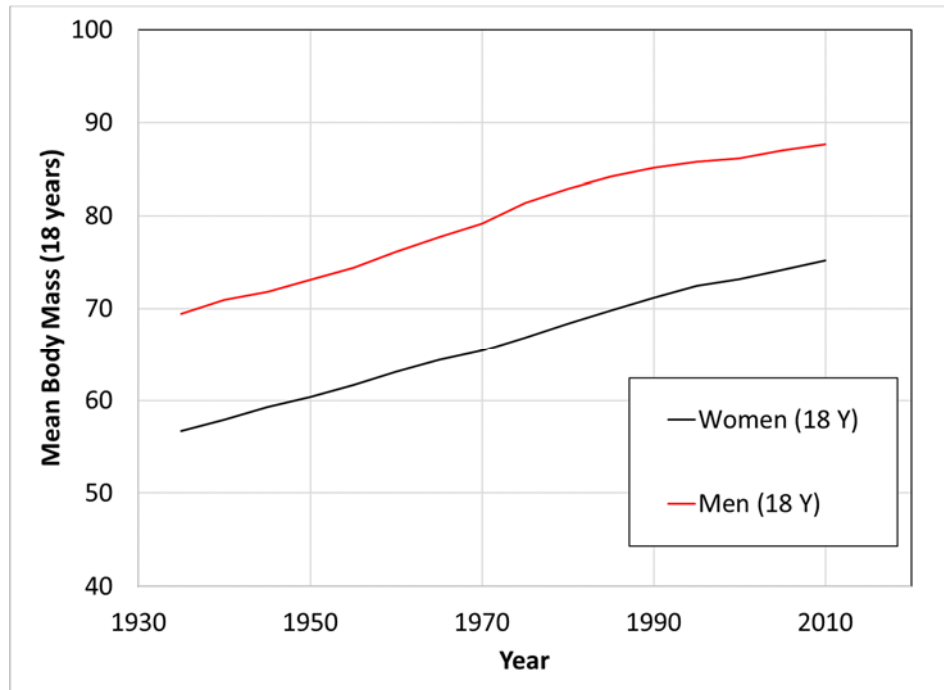


Figure 44. Body mass of 18-year-old men and women by age from 1940-2010 (NCDRisk, 2020 for stature, [130] Komlos, 2011 for BMI, Population demographics from Census, 1975[131]). The average mass of men has increased 19.2% from 1940 to 2010. The average mass of women has increased 23.2%.

6.3 Muscle and spinal characteristics

To determine the effect of muscle characteristics on scaling the injury risk from the 1939-1955 time period, regressions are used that relate body mass to muscle PCSA in the torso. Marras et al (2001) [61] provide regressions for large abdominal muscles based on combinations of BMI, height, weight, and combinations of height and weight. These are tabulated in

Table 13 for the 50% male and female comparing 1939 values to 2014 values. As discussed above, the largest differences are attributable to mass differences between the demographics. For example, it is striking that a 2014 50% female has a larger body mass than a 1939 50% male. The regressions for the muscles listed in this table show increases in body size are correlated with an average 23.3% increase in the PCSA for mid-sized women over the time period and 19.0% increase in mid-sized men. This estimated increase potentially increases the full activation forces by the increased PCSA acting in the direction of the lumbar spinal support in the absence of abdominal pressure support. In particular the full effect of changes to posterior musculature such as erector spinae increased area will likely be felt in the spine when the torso muscles are fully activated, as opposed to the anterior musculature in which the spine may be shielded by abdominal support.

Using the PCSA regressions from Marras (2001) [61] in terms of height and body mass and the vertebral body cross sectional area (VBCSA) regressions from Korpinen (2019) [106] in terms of body mass, the percentage change in PCSA and VBCSA are shown for men in Figure 45 and women in Figure 46. Based on trends in the relative areas, the ratio between PCSA and VBCSA is approximately the same for women from 1940 to 2010, but shows a substantial decrease in the ratio for men based on the relative increase in the regression for PCSA by demographics. The ratio of PCSA/VBCSA has increased for women relative to men over the time investigated. In 1940, women's ratios

were approximately 90% men suggesting they had lower average risk than men. By 2010, the risks are similar. Based on the relative torso masses between men and women and the influence of the relative spinal cross sectional areas, this is not unexpected. For example, Schmidt, 2012 [132] found that there were fundamental differences in injury risk between men and women outside vertebral area/stress contributions alone, but that these differences were compensated by decreased torso mass distribution in women, leading to similar injury risk between men and women before adding torso borne protective equipment. Presumably, the remodeling adaptation for both PCSA and VBCSA that led to this result occur across the population for normal physiological stresses, and the regressions of Marras et al. and Korpinen et al. implicitly include these effects. The PCSA/VBCSA ratio for men and women was used to adjust force estimates from earlier studies for risk analysis below.

Table 13. Demographic characteristics of mid-size female and males in 1939 and 2014 (NCDRisk, 2020, CDC, 2020[62]) and PCSA values for selected muscles from regressions of Marras et al. (2001). Based on the calculated regressions, the demographic changes are correlated with an increase in weighted PCSA of 19.0% from 1939 to 2014, while the PCSA for women has increased an average of 23.3%. These estimated changes are largely attributable to body mass differences.

	50% Female		50% Male	
	Year		Year	
Year	1939	2014	1939	2014
BMI (kg/m ²)	23.45	28.12	23.41	27.92
Height (cm)	160.45	163.54	173.96	177.13
Weight (kg)	60.36	75.22	70.83	87.61
HTWT (m kg)	96.85	123.01	123.22	155.18
HTDWT (cm/kg)	2.66	2.17	2.46	2.02
WTDHT (kg/cm)	0.38	0.46	0.41	0.49
-				
Muscle PCSA (cm ²)				
R. erector spinae	18.40	25.57	23.59	28.38
L. erector spinae	17.12	23.18	23.34	28.70
R. rectus abdominis	7.10	9.03	7.89	10.08
L. rectus abdominis	7.49	9.63	7.77	10.07
R. internal oblique	6.81	8.10	9.23	11.17
L. quadratus lumborum	2.82	3.41	4.54	5.82

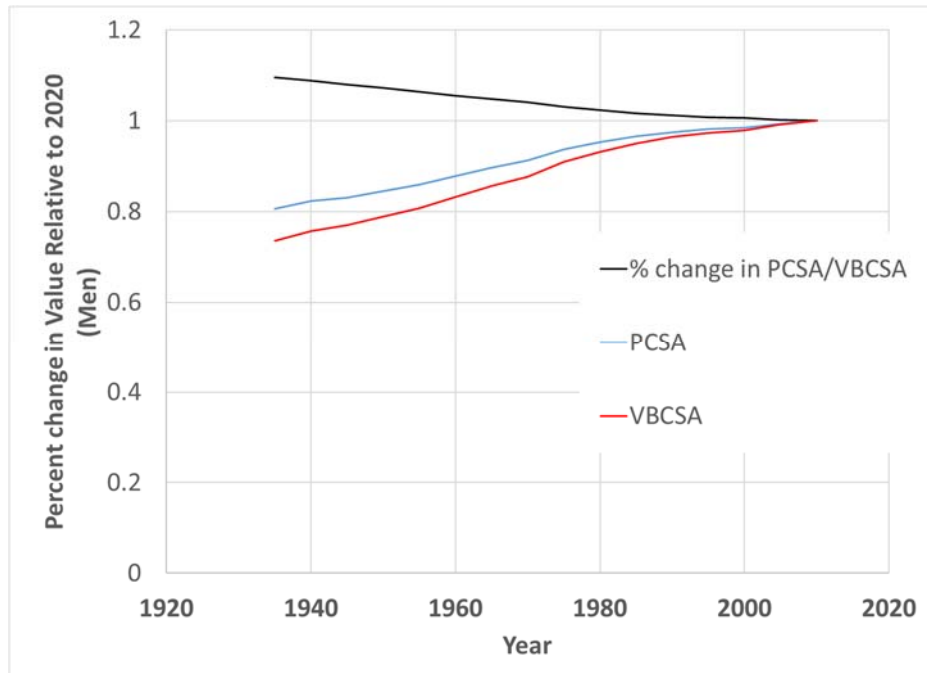


Figure 45. Percentage change in PCSA and vertebral body cross sectional area (VBCSA) by year in young men. PCSA estimates were based on erector spinae area regressions by height and weight (Marras et al., 2001), and VBCSA estimates are based on population regressions by body mass for men (Korpinen, 2019). Ratio of the change of PCSA to VBCSA shows that the body mass and stature effect makes mean 1940's men at less risk of spinal fracture from full muscle activation than 2010 men.

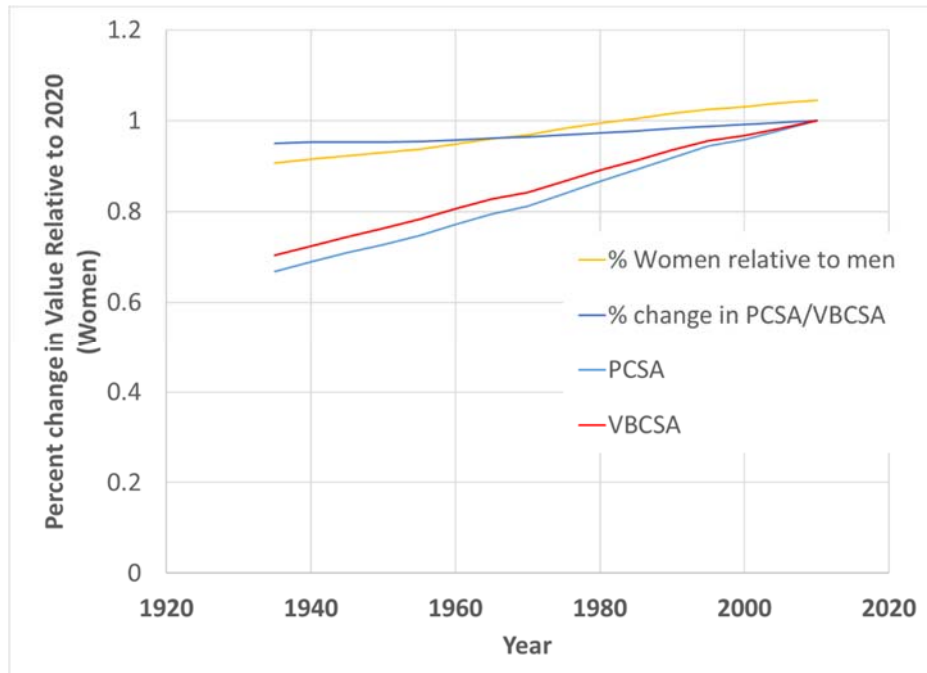


Figure 46. Percentage change in PCSA and vertebral body cross sectional area (VBCSA) by year in young women. PCSA estimates were based on erector spinae area regressions by height and weight (Marras et al., 2001), and VBCSA estimates are based on population regressions by body mass for women (Korpinen, 2019). Ratio of the change of PCSA to VBCSA shows that the body mass and stature effect makes mean 1940's women have approximately the same risk of spinal fracture from full muscle activation than 2010 women. The relative values between men and women have changed over this time, with women's risk values increasing relative to men.

6.4 Weibayes analysis

The previous estimate for 50th percentile male lumbar spinal fracture in terms of axial force (Figure 30) can be used as a basis for an estimate of the thoracic and lumbar injury risk for full muscle activation. Uncorrected injury risk for full muscle activation for males and females across the available studies is shown in Figure 41. Since the input

force is unknown, even though the outcome measure (injury/no injury) is available, several simplifying assumptions have been made.

1. The major effect on lumbar axial force in full activation may be approximated by differences in the erector spinae alone. As noted above, these are not offset by abdominal pressure effects in the tensed state.
2. Spinal loading across the relevant time period may be scaled using Figure 45 for men and Figure 46 for women.
3. Force values implied in all cases represented fully activated muscles.
4. The form of the lumbar osteoligamentous risk curve maintains its slope in a Weibull distribution and the slope is the same as that given for 50% risk of lumbar spinal fracture given above for males and females for both the thoracic and lumbar spine (Weibayes assumption, cf. Abernethy, 1983[133]).
5. The demographic characteristics of the patients from a given time period may be approximated by a sampling a Gaussian distribution about the mean height and mass by sex and that the mean height and mass in the general population is the same as the patient population, and this sampling distribution may be corrected for the ratio of percentage change PCSA to VBCSA over the time period of the studies.

The breakdown of thoracic and lumbar injuries by sex is shown in Table 14.

Using these assumptions, a scaled Weibayes analysis was performed using Minitab 19 (Minitab, Inc). Based on the lumbar spine injury data, the male 2010 risk curve was scaled to a male 1945 risk curve and the resulting Weibull scale was calculated using the lumbar injury risk data from the studies. These were translated to females using the regression equations discussed above and a new 1945 injury risk assessment was calculated, again assuming a Weibull distribution with a fixed slope. These values were then scaled to 2010 values using the assumptions and regressions above. The resulting Weibull coefficients are shown in Table 15.

Table 14. Breakdown of thoracic and lumbar injuries by sex in the 19 studies in Table 12.

	Thoracic Spine		Lumbar Spine	
	n	fx	n	fx
Men	1204	359	1204	10
Women	1058	230	1058	4

Table 15. Weibull coefficients for the statistical models by sex and year.

	Year	Shape	Scale
Men	1945	3.199±0.037	6340±449
	2010	3.199±0.037	5873±416
Women	1945	3.199±0.037	5851±415
	2010	3.199±0.037	6127±434

Using the assumptions above, the thoracic injury risk values from the dataset may be used to assess the derived force ratios for men to women at relatively high risk. In Figure 47, the ratio of PCSA to VBCSA to the relative risk of spinal fractures in the thoracic spine from the dataset is compared for values scaled to 1945. The two force ratios are comparable, suggesting that the ratio of PCSA to VBCSA is likely a good correlate for injury risk among men and women, and that the injury risk Weibull values derived above are suitable for assessing spinal fracture from large muscle action.

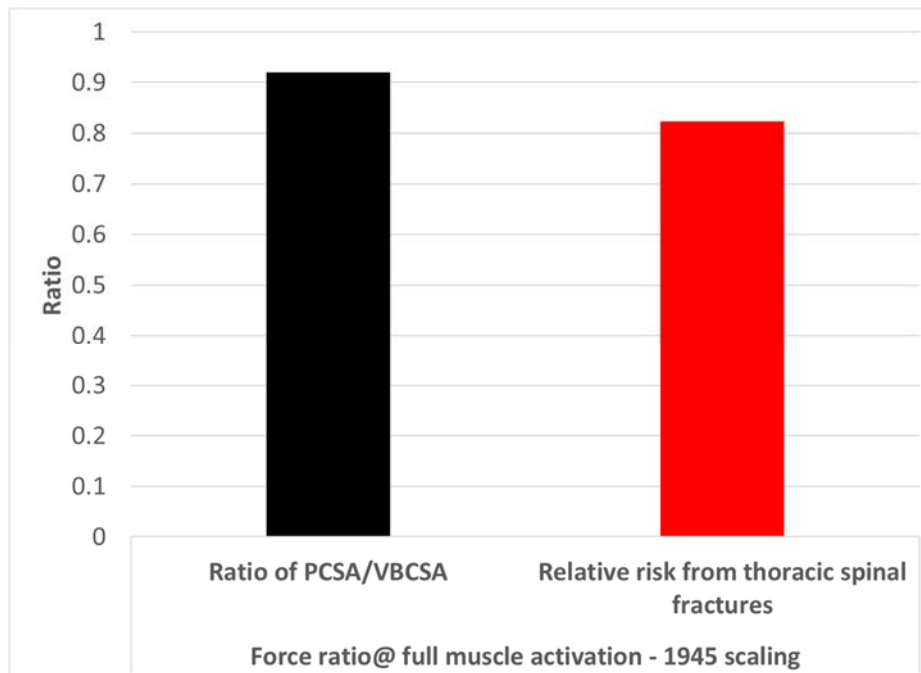


Figure 47. Ratio of VBSA/VBCSA for men and women compared with relative risk from thoracic spinal fractures scaled to 1945 values. Based on the assumptions in the models, these are in relatively close agreement with the injury risk assessments from PCSA/VBCSA of approximately 0.92 from men to women with thoracic spinal fractures estimated as 0.82 on a common force basis accounting for differences in PCSA and VBCSA.

6.5 Conclusions

Based on the analysis of spinal fractures from convulsive therapy and grand mal epileptic seizures, injury risk functions for injury risk to the lumbar spine for full activation for men and women were developed. Since much of the data was gathered in the 1940s before the widespread use of paralytics for convulsive therapy, scaling principles were developed to correct for population differences across the time period. The injury risk assessments are consistent with frequent thoracic injury risk seen in these

settings. This concordance suggests that the differences in injury risk between men and women are largely in structural anthropometry and PCSA.

6.6 Limitations

Based on the assumptions and limitations in the dataset, there are a number of important information. The analysis is based on demographic and anthropometric principles alone. Many of the regressions used in this analysis are based on demographic characteristics and imaging findings from a population at a given time, not across time periods. It is uncertain if these regressions hold across time periods.

The effects of nutrition and fitness are not considered here. It is likely these are somewhat offsetting; there is likely improved fitness because of more physical activity in the 1940s reducing risk from the 1940s relative to the current period. However, improved nutrition in the current period likely improves bone strength. As a stark example, pellagra (niacin) deficiency still caused substantial mortality in the 1940s, but was almost completely eliminated by 1950 [134].

The Weibayes analysis assumptions present substantial limitations since there is no underlying knowledge of the force to fail in any of the patients. This could be further mitigated using population reconstructions with a validated lumbar and thoracic spine model.

7 Conclusions and contributions to science

Women are moving into new positions in the work force that have different physical demands than those previously investigated in biomechanics. In particular, they are being exposed to vertical impacts, such as those seen in underbody blast. As the military has transitioned to including women in all combat roles, it is vital to understand how women's risk of injury differs from men's. This dissertation investigated anatomical differences between men and women and their role in sex-based variances in biomechanical response. Furthermore, this dissertation investigated the role of active musculature in lumbar spine kinetics during vertical impact loading. This study gives insight into sex-based differences in the lumbar spine during realistic combat exposures. Sub-failure response with active musculature were investigated for both different sexes, and different muscle activation strategies. By better understanding the female lumbar spine response, new safety measures can be developed. This work could inform the design of new protective personal equipment, or guide permissible exposure limits and risk of injury.

A 50th percentile male hybrid multibody/finite element model was developed for use in high rate vertical impact loading. This model is unique in that it includes intra-abdominal pressure, active musculature, and an osteoligamentous spine validated for underbody blast. Previously, there were no underbody blast models that included active musculature and intra-abdominal pressure. Previous models that included active

musculature and intra-abdominal pressure were not developed, or validated in underbody blast.

Relaxed and active muscle activations were developed to in stabilizing the torso during gravitational loading, which are then applied during dynamic loading conditions. In the relaxed activation state, all activations were below 10 percent and resulted in axial forces of less than 15 N per muscle. Extensor contraction was required to keep the torso upright against gravity. In the tensed activation state, activations varied between 75 and 100 percent, resulting in a peak T12/L1 compressive force of 2623 N, corresponding to a seven percent risk of failure.

A sensitivity analysis of model parameters revealed the interplay between intra-abdominal pressure, active musculature, and the osteoligamentous spine is complex, and all three are needed to capture spinal response. This is a major contribution of this dissertation. Higher muscle cross-sectional areas lead to both higher peak intra-abdominal pressures, as well as peak spinal compressive forces. Peak intra-abdominal pressure was most sensitive to axial stiffness of the spine, muscular cross-sectional area, and initial intra-abdominal pressure.

The osteoligamentous portion of the 50th percentile male model was validated against novel strain energy vs force corridors, generated from experimental data. Also developed for this dissertation were T12/L1 spinal fracture injury risk functions for the 50th percentile male, which were then scaled to the 50th percentile female and 85th

percentile female. During failure loading (as seen from experimental tests), the osteoligamentous spine model predicts a 41% risk of failure. While the model slightly underpredicts the risk of injury, the peak compressive load in T12/L1 lies within the 95th percentile confidence intervals for the 50th percentile risk of injury. Therefore the model is validated for use in injurious underbody blast loading conditions.

When comparing the relaxed to tensed activation states during 200 N/ms underbody blast loading, there was a 10x increase in spinal force for the tensed state. The peak T12/L1 axial force was 2487 N, which is 47 percent of the estimated compressive failure load. This is similar to the compressive preloads in a tensed state for a cervical model [69]. A comparison of a preliminary 85th percentile female model to the 50th percentile male model predicts higher axial loads due to changes in musculature.

It was hypothesized that men and women do not have the same risk of injury on a stress basis. This hypothesis was supported by comparing mass-matched male and female hybrid multibody/finite element models during failure and subfailure loading conditions. It was also hypothesized that the use of active musculature decreases injury tolerance in compressive loading. This hypothesis was supported by comparing model intervertebral axial loads to both experimental (underbody blast) and epidemiological (electroconvulsive therapy) loading conditions. Finally, a sensitivity analysis was performed to help guide future research efforts and to ensure hypotheses results are valid for a range of model parameters encompassing human variance.

This dissertation provides the following contributions to the field of injury biomechanics:

1. This research produced a high-rate lumbar hybrid multibody/finite element model validated for vertical impact loading with relatively rapid run times. By including active musculature, the model can be used to further understand live human response to realistic vertical impact loading conditions.
2. This research produced mass matched male and female scaling relationships, and a preliminary 85th percentile female hybrid multibody/finite element model. It demonstrates women are more vulnerable than men to lumbar spine injury on an effective stress basis through finite element modeling. It provides insight that changes in muscle cross-sectional areas and lines of action contribute to variance in force response when matched for mass.
3. This research demonstrates higher muscle activations increase risk of lumbar spine injury in vertical impact loading. A tensed activation state contributes 48 percent of the compressive load estimated to fracture the lumbar spine during underbody blast. While this corresponds to a low risk of injury (<10%), this could exacerbate risk of injury during additional compressive loading. This can inform bracing strategies during potential vertical impact loading scenarios such as underbody blast

References

1. Compressive strength of lumbar spine elements related to age, gender, and other influencing factors. Anderson P, Hobart d, danoff J. Electromyographical kinesiology: proceedings of the 8th Congress of the International Society of Electrophysiological Kinesiology; 1990.
2. Hansson T, Roos BR, Nachemson A. The bone mineral content and ultimate compressive strength of lumbar vertebrae. *Spine* 1980;5(1):46-55
3. Cooper C, Atkinson EJ, MichaelO'Fallon W, Melton JL. Incidence of clinically diagnosed vertebral fractures: A population-based study in rochester, minnesota, 1985-1989. *Journal of Bone and Mineral Research* 1992;7(2):221-27
4. Brinckmann P, Biggemann M, Hilweg D. Prediction of the compressive strength of human lumbar vertebrae. *Clinical Biomechanics* 1989;4:iii-27
5. Schmidt AL, Paskoff G, Shender BS, Bass CR. Risk of lumbar spine injury from cyclic compressive loading. *Spine* 2012;37(26):E1614-21 doi: 10.1097/BRS.0b013e3182752a19[published Online First: Epub Date] |.
6. Adams MA, Freeman BJC, Morrison HP, Nelson IW, Dolan P. Mechanical initiation of intervertebral disc degeneration. *Spine* 2000;25(13):1625-36 doi: Doi 10.1097/00007632-200007010-00005[published Online First: Epub Date] |.
7. Mcgill SM, Patt N, Norman RW. Measurement of the Trunk Musculature of Active Males Using Ct Scan Radiography - Implications for Force and Moment Generating Capacity About the L4/L5 Joint. *Journal of Biomechanics* 1988;21(4):329-& doi: Doi 10.1016/0021-9290(88)90262-X[published Online First: Epub Date] |.
8. Shirazi-Adl A, El-Rich M, Pop D, Parnianpour M. Spinal muscle forces, internal loads and stability in standing under various postures and loads-application of kinematics-based algorithm. *Eur Spine J* 2005;14(4):381-92 doi: 10.1007/s00586-004-0779-0[published Online First: Epub Date] |.

9. Dibb AT, Cox CA, Nightingale RW, et al. Importance of Muscle Activations for Biofidelic Pediatric Neck Response in Computational Models. *Traffic Inj Prev* 2013;**14**:S116-S27 doi: 10.1080/15389588.2013.806795[published Online First: Epub Date] | .

10. Wong C, Gehrchen PM, Darvann T, Kiaer T. Nonlinear finite-element analysis and biomechanical evaluation of the lumbar spine. *Ieee T Med Imaging* 2003;**22**(6):742-46 doi: 10.1109/Tmi.2003.814783[published Online First: Epub Date] | .

11. Kulak RF, Belytschko TB, Schultz AB, Galante JO. Nonlinear Behavior of Human Intervertebral-Disk under Axial Load. *Journal of Biomechanics* 1976;**9**(6):377-86 doi: Doi 10.1016/0021-9290(76)90115-9[published Online First: Epub Date] | .

12. Simon BR, Wu JSS, Carlton MW, Evans JH, Kazarian LE. Structural Models for Human Spinal Motion Segments Based on a Poroelastic View of the Intervertebral-Disk. *J Biomech Eng-T Asme* 1985;**107**(4):327-35 doi: Doi 10.1115/1.3138565[published Online First: Epub Date] | .

13. Gilsanz V, Boechat MI, Gilsanz R, Loro ML, Roe TF, Goodman WG. Gender differences in vertebral sizes in adults: biomechanical implications. *Radiology* 1994;**190**(3):678-82

14. Maughan R, Watson JS, Weir J. Strength and cross-sectional area of human skeletal muscle. *The journal of physiology* 1983;**338**:37

15. Janssen I, Heymsfield SB, Wang Z, Ross R. Skeletal muscle mass and distribution in 468 men and women aged 18–88 yr. *Journal of applied physiology* 2000;**89**(1):81-88

16. Easton NL, Sommers J. VERTEBRAL FRACTURES IN METRAZOL THERAPY WITH AND WITHOUT THE USE OF CURARE AS A SUPPLEMENT. *The Journal of Nervous and Mental Disease* 1944;**99**(3):256-63

17. Dewald PA, Margolis NM, Weiner H. Vertebral fractures as a complication of electroconvulsive therapy. *Journal of the American Medical Association* 1954;**154**(12):981-84
18. Effects of torso-borne mass and loading severity on early response of the lumbar spine under high-rate vertical loading. IRCOBI; 2013.
19. McConville JT, Clauser CE, Churchill TD, Cuzzi J, Kaleps I. Anthropometric relationships of body and body segment moments of inertia: DTIC Document, 1980.
20. NASA Man-Systems Integration Standards. NASA-STD-3001 Space Flight Human-System Standard, 1995.
21. Enoka RM. *Neuromechanics of human movement*: Human kinetics, 2008.
22. Grenier SG, McGill SM. Quantification of lumbar stability by using 2 different abdominal activation strategies. *Archives of physical medicine and rehabilitation* 2007;**88**(1):54-62
23. Sanchez NC, Tenofsky PL, Dort JM, Shen LY. What is normal intra-abdominal pressure?/Discussion. *The American surgeon* 2001;**67**(3):243
24. Standardization IOf. ISO 2631-5:2004 Mechanical vibration and shock. Evaluation of human exposure to whole-body vibration- Part 5: Method for evaluation of vibration containing multiple shocks, 2004.
25. Code of Federal Regulations. Title 14- Aeronautics and Space; Chapter I- Federal Aviation Administration, Department of Transportation; Subchapter C- Aircraft; Part 25- Airworthiness Standards: Transport Category Airplanes, 2016.
26. Code of Federal Regulations. Title 49- Transportation; Part 751- Federal Motor Vehicle Safety Standards; Standard No. 208- Occupant crash protection, 2011.

27. MADYMO Quality Report - Active Human 50th Facet Q Model version 1.1 (R7.5): TASS International, 2013.
28. Miller MZ, Mosher SE. Test configuration and data acquisition system for the investigation of human response to varied +gz impact duration and amplitude (HGZ study) test program. Wright-Patterson AFB, Ohio: DynCorp Scientific Support Division, 1989.
29. Global Human Body Models Consortium L. User Manual: M50 Occupant. Version 4.4 for LS-DYNA: Elemance, LLC, 2015.
30. Total Human Model for Safety - THUMS -About. Secondary Total Human Model for Safety - THUMS -About 2011. <http://www.lstc.com/thums>.
31. Dreischarf M, Zander T, Shirazi-Adl A, et al. Comparison of eight published static finite element models of the intact lumbar spine: Predictive power of models improves when combined together. *Journal of biomechanics* 2014;**47**(8):1757-66
32. Abouhossein A, Weisse B, Ferguson SJ. A multibody modelling approach to determine load sharing between passive elements of the lumbar spine. *Computer methods in biomechanics and biomedical engineering* 2011;**14**(06):527-37
33. Pintar FA, Yoganandan N, Myers T, Elhagediab A, Sances A. Biomechanical properties of human lumbar spine ligaments. *Journal of biomechanics* 1992;**25**(11):1351-56
34. de Jager MKJ. *Mathematical head-neck models for acceleration impacts*, 1996.
35. Yoshimura T, Nakai K, Tamaoki G. Multi-body dynamics modelling of seated human body under exposure to whole-body vibration. *Industrial health* 2005;**43**(3):441-47
36. de Zee M, Hansen L, Wong C, Rasmussen J, Simonsen EB. A generic detailed rigid-body lumbar spine model. *J Biomech* 2007;**40**(6):1219-27

37. Oñate E, Oliver J, A. H, eds. The influence of muscle modeling methods and paths on head and neck response. WCCM XI; 2014; Barcelona, Spain. ICNME.
38. Dibb AT, Cutcliffe HC, Luck JF, et al. Pediatric Head and Neck Dynamics in Frontal Impact: Analysis of Important Mechanical Factors and Proposed Neck Performance Corridors for Six and Ten year old ATDs. *Traffic Injury Prevention* 2014;**15**(4):386-94 doi: 10.1080/15389588.2013.824568[published Online First: Epub Date] |.
39. Iatridis JC, Kumar S, Foster RJ, Weidenbaum M, Mow VC. Shear mechanical properties of human lumbar annulus fibrosus. *Journal of orthopaedic research* 1999;**17**(5):732-37
40. Keaveny TM, Morgan EF, Yeh OC. Bone mechanics. Standard handbook of biomedical engineering and design 2004
41. Panjabi MM, Chen NC, Shin EK, Wang J-L. The cortical shell architecture of human cervical vertebral bodies. *Spine* 2001;**26**(22):2478-84
42. Carter DR, Caler WE, Spengler DM, Frankel VH. Fatigue behavior of adult cortical bone: the influence of mean strain and strain range. *Acta Orthopaedica Scandinavica* 1981;**52**(5):481-90
43. Galante J, Rostoker W, Ray R. Physical properties of trabecular bone. *Calcified tissue research* 1970;**5**(1):236-46
44. Winters JM, Stark L. Estimated mechanical properties of synergistic muscles involved in movements of a variety of human joints. *Journal of biomechanics* 1988;**21**(12):1027-41
45. Winters JM. How detailed should muscle models be to understand multi-joint movement coordination? *Human Movement Science* 1995;**14**(4):401-42
46. Chancey VC, Nightingale RW, Van Ee CA, Knaub KE, Myers BS. Improved estimation of human neck tensile tolerance: reducing the range of reported

tolerance using anthropometrically correct muscles and optimized physiologic initial conditions: SAE Technical Paper, 2003.

47. Gordon C, Blackwell C, Bradtmiller B, et al. Anthropometric survey of US Army personnel (ANSUR II): Methods and summary statistics. Natick, MA: U.S. Army Natick Research, Development and Engineering Center, 2012.
48. Benson DJ, Hallquist JO. A Simple Rigid Body Algorithm for Structural Dynamics Programs. *Int J Numer Meth Eng* 1986;**22**(3):723-49 doi: DOI 10.1002/nme.1620220313[published Online First: Epub Date] |.
49. Zatsiorsky V. Methods of determining mass-inertial characteristics of human body segments. *Contemporary Problems of Biomechanics* 1990
50. Stokes IA, Gardner-Morse M. Quantitative anatomy of the lumbar musculature. *Journal of biomechanics* 1999;**32**(3):311-16
51. Dibb AT. Pediatric head and neck dynamic response: A computational study [Ph.D. Thesis]. Duke University, 2011.
52. Brinckmann P, Biggemann M, Hilweg D. Fatigue fracture of human lumbar vertebrae. *Clinical biomechanics* 1988;**3**:i-S23
53. Shea M, Edwards W, White A, Hayes W. Variations of stiffness and strength along the human cervical spine. *Journal of biomechanics* 1991;**24**(2):95-107
54. Adams M, Dolan P. A technique for quantifying the bending moment acting on the lumbar spine in vivo. *Journal of biomechanics* 1991;**24**(2):117-26
55. Adams M, McNally D, Chinn H, Dolan P. The clinical biomechanics award paper 1993 posture and the compressive strength of the lumbar spine. *Clinical Biomechanics* 1994;**9**(1):5-14

56. Adams MA, Hutton W. The effect of posture on the role of the apophysial joints in resisting intervertebral compressive forces. *The Journal of bone and joint surgery. British volume* 1980;**62**(3):358-62
57. The influence of muscle modeling methods and paths on head and neck response. 11th World Congress on Computational Mechanics (WCCM XI); 2014; Barcelona, Spain.
58. On the structural and material properties of mammalian skeletal muscle and its relevance to human cervical impact dynamics. *Proceedings: Stapp Car Crash Conference*; 1995. Society of Automotive Engineers SAE.
59. Hedenstierna S, Halldin P. How does a three-dimensional continuum muscle model affect the kinematics and muscle strains of a finite element neck model compared to a discrete muscle model in rear-end, frontal, and lateral impacts. *Spine* 2008;**33**(8):E236
60. CDC. Clinical Growth Charts. Secondary Clinical Growth Charts June 16, 2017. https://www.cdc.gov/growthcharts/clinical_charts.htm#Set1.
61. Marras W, Jorgensen M, Granata K, Wiand B. Female and male trunk geometry: size and prediction of the spine loading trunk muscles derived from MRI. *Clinical Biomechanics* 2001;**16**(1):38-46
62. Valverde E, Casinos A, Alba-Fernández C, Del Río L. Lumbar ontogenetic allometry and dimorphism in humans. A case for comparison between interspecific and intraspecific scaling. *European journal of morphology* 2005;**42**(4):185-92
63. Adams M, Hutton W, Stott J. The resistance to flexion of the lumbar intervertebral joint. *Spine* 1980;**5**(3):245-53
64. Adams M, Dolan P. Time-dependent changes in the lumbar spine's resistance to bending. *Clinical Biomechanics* 1996;**11**(4):194-200

65. Gordon CC, Blackwell CL, Bradtmiller B, et al. 2012 anthropometric survey of US army personnel: methods and summary statistics: Army Natick Soldier Research Development and Engineering Center MA, 2014.
66. LaVelle M. Natural selection and developmental sexual variation in the human pelvis. *American Journal of Physical Anthropology* 1995;**98**(1):59-72
67. Tague RG. Variation in pelvic size between males and females. *American Journal of Physical Anthropology* 1989;**80**(1):59-71
68. Hallquist JO. LS-DYNA theory manual. Livermore software Technology corporation 2006;**3**:25-31
69. Dibb AT, Cox CA, Nightingale RW, et al. Importance of Muscle Activations for Biofidelic Pediatric Neck Response in Computational Models. *Traffic Injury Prevention* 2013;**14**(sup1):S116-S27 doi: 10.1080/15389588.2013.806795[published Online First: Epub Date] |.
70. Chancey VC, Nightingale RW, Van Ee CA, Knaub KE, Myers BS. Improved estimation of human neck tensile tolerance: reducing the range of reported tolerance using anthropometrically correct muscles and optimized physiologic initial conditions. *Stapp Car Crash Journal* 2003;**47**:135-53
71. Vasavada AN, Danaraj J, Siegmund GP. Head and neck anthropometry, vertebral geometry and neck strength in height-matched men and women. *Journal of biomechanics* 2008;**41**(1):114-21
72. New model of lumbar spine biomechanics with the use of simulation analysis. MATEC Web of Conferences; 2019. EDP Sciences.
73. Patwardhan AG, Meade KP, Lee B. A frontal plane model of the lumbar spine subjected to a follower load: implications for the role of muscles. *J. Biomech. Eng.* 2001;**123**(3):212-17

74. Hwang J, Knapik GG, Dufour JS, et al. A biologically-assisted curved muscle model of the lumbar spine: model structure. *Clinical Biomechanics* 2016;**37**:53-59
75. Bruno AG, Boussein ML, Anderson DE. Development and validation of a musculoskeletal model of the fully articulated thoracolumbar spine and rib cage. *Journal of biomechanical engineering* 2015;**137**(8)
76. Cholewicki J, McGill SM. Mechanical stability of the in vivo lumbar spine: implications for injury and chronic low back pain. *Clinical biomechanics* 1996;**11**(1):1-15
77. Cholewicki J, Juluru K, McGill SM. Intra-abdominal pressure mechanism for stabilizing the lumbar spine. *Journal of biomechanics* 1999;**32**(1):13-17
78. Christophy M, Senan NAF, Lotz JC, O'Reilly OM. A musculoskeletal model for the lumbar spine. *Biomechanics and modeling in mechanobiology* 2012;**11**(1-2):19-34
79. Gagnon D, Larivière C, Loisel P. Comparative ability of EMG, optimization, and hybrid modelling approaches to predict trunk muscle forces and lumbar spine loading during dynamic sagittal plane lifting. *Clinical Biomechanics* 2001;**16**(5):359-72
80. Ignasiak D, Dendorfer S, Ferguson SJ. Thoracolumbar spine model with articulated ribcage for the prediction of dynamic spinal loading. *Journal of biomechanics* 2016;**49**(6):959-66
81. Panjabi M. The intersegmental and multisegmental muscles of the lumbar spine. A biomechanical model comparing lateral stabilizing potential, 1991.
82. Han K-S, Zander T, Taylor WR, Rohlmann A. An enhanced and validated generic thoraco-lumbar spine model for prediction of muscle forces. *Medical engineering & physics* 2012;**34**(6):709-16
83. Pedotti A, Krishnan V, Stark L. Optimization of muscle-force sequencing in human locomotion. *Mathematical Biosciences* 1978;**38**(1-2):57-76

84. Sanchez NC, Tenofsky PL, Dort JM, Shen LY. What is normal intra-abdominal pressure?/Discussion. *The American surgeon* 2001;**67**(3):243
85. Reed MP, Ebert SM. The seated soldier study: posture and body shape in vehicle seats. 2013
86. Newell RS, Blouin J-S, Street J, Cripton PA, Siegmund GP. The neutral posture of the cervical spine is not unique in human subjects. *Journal of biomechanics* 2018;**80**:53-62
87. Hansen L, De Zee M, Rasmussen J, Andersen TB, Wong C, Simonsen EB. Anatomy and biomechanics of the back muscles in the lumbar spine with reference to biomechanical modeling. *Spine* 2006;**31**(17):1888-99
88. Reid JG, Costigan P. Geometry of adult rectus abdominis and erector spinae muscles. *Journal of Orthopaedic & Sports Physical Therapy* 1985;**6**(5):278-80
89. Zajac FE. Muscle and tendon: properties, models, scaling, and application to biomechanics and motor control. *Critical reviews in biomedical engineering* 1989;**17**(4):359-411
90. Dibb AT, Nightingale RW, Luck JF, Chancey VC, Fronheiser LE, Myers BS. Tension and Combined Tension-Extension Structural Response and Tolerance Properties of the Human Male Ligamentous Cervical Spine. *Journal of Biomechanical Engineering* 2009;**131**(8):081008-11
91. Han J, Ahn J, Goel V, McGowan D. CT-based geometric data of human spine musculature. Part I. Japanese patients with chronic low back pain. *Clinical Spine Surgery* 1992;**5**(4):448-58
92. Yoganandan N, Stemper BD, Baisden JL, Pintar FA, Paskoff GR, Shender BS. Effects of acceleration level on lumbar spine injuries in military populations. *The Spine Journal* 2015

93. Stemper BD, Storvik SG, Yoganandan N, et al. A new PMHS model for lumbar spine injuries during vertical acceleration. *Journal of biomechanical engineering* 2011;**133**(8):081002
94. Peterson R, Pierce E, Price B, Bass C. Shock mitigation for the human on high speed craft: development of an impact injury design rule: DTIC Document, 2004.
95. Jamison D, Cannella M, Pierce EC, Marcolongo MS. A comparison of the human lumbar intervertebral disc mechanical response to normal and impact loading conditions. *Journal of biomechanical engineering* 2013;**135**(9):091009
96. Stemper B, Yoganandan N, Paskoff G, et al. Thoracolumbar spine trauma in military environments. *Minerva Ortopedica E Traumatologica* 2011;**62**(5):397
97. Alvarez JG. Injuries of Concern & Medical Research Plan for Warrior Injury Assessment Manikin (WIAMan), 2011.
98. Hauret KG, Jones BH, Bullock SH, Canham-Chervak M, Canada S. Musculoskeletal injuries: description of an under-recognized injury problem among military personnel. *American journal of preventive medicine* 2010;**38**(1):S61-S70
99. Dempsey ME, Panetta LE. Memorandum for secretaries of the military departments acting under secretary of defense for personnel and readiness chiefs of the military services, Subject: Elimination of the 1994 Direct Ground Combat Definition and Assignment Rule. In: Defense Do, ed., 2013.
100. Bailey AM, Christopher JJ, Brozoski F, Salzar RS. Post mortem human surrogate injury response of the pelvis and lower extremities to simulated underbody blast. *Annals of biomedical engineering* 2015;**43**(8):1907-17
101. Yoganandan N, Moore J, DeVogel N, et al. Human lumbar spinal column injury criteria from vertical loading at the base: Applications to military environments. *Journal of the Mechanical Behavior of Biomedical Materials* 2020:103690

102. Lei J, Zhu F, Jiang B, Wang Z. Underbody blast effect on the pelvis and lumbar spine: A computational study. *Journal of the Mechanical Behavior of Biomedical Materials* 2018;**79**:9-19
103. Pietsch HA, Bosch KE, Weyland DR, et al. Evaluation of WIAMan technology demonstrator biofidelity relative to sub-injurious PMHS response in simulated under-body blast events: SAE Technical Paper, 2016.
104. Reed MP. Development of Anthropometric Specifications for the Warrior Injury Assessment Manikin (WIAMan): MICHIGAN UNIV ANN ARBOR TRANSPORTATION RESEARCH INST, 2013.
105. Viscoelasticity of the Lumbar Spine; 2015; Tampa, Florida. Biomedical Engineering Society Annual Symposium.
106. Korpinen N, Keisu A, Niinimäki J, et al. Body mass estimation from dimensions of the fourth lumbar vertebra in middle-aged Finns. *Legal Medicine* 2019;**40**:5-16
107. Low A, Sonenthal I, Blaurock M, Kaplan M, Sherman I. Metrazol shock treatment of the functional psychoses. *Archives of Neurology & Psychiatry* 1938;**39**(4):717-36
108. Ross JR, Malzberg B. A review of the results of the pharmacological shock therapy and the metrazol convulsive therapy in New York State. *American Journal of Psychiatry* 1939;**96**(2):297-316
109. Shorter E, Healy D. *Shock therapy: a history of electroconvulsive treatment in mental illness*: Rutgers University Press, 2007.
110. Bennett AE. Preventing traumatic complications in convulsive shock therapy by curare. *Journal of the American Medical Association* 1940;**114**(4):322-24
111. Pacella BL. Sequelae and complications of convulsive shock therapy. *Bulletin of the New York Academy of Medicine* 1944;**20**(11):575

112. ANDROP S, MARGOLIN ES, MARSHALL JH, RITTENHOUSE M. Vertebral compression fractures sustained during convulsions. Archives of Surgery 1941;**42**(3):550-56
113. BARRETT JE, FUNKHOUSER JB, BARKER WA. Spinal injuries in shock and epileptic convulsions. American Journal of Psychiatry 1942;**99**(3):387-90
114. Bennett BT, Fitzpatrick CP. Fractures of the spine complicating metrazol therapy. Journal of the American Medical Association 1939;**112**(22):2240-44
115. Cummins J. Metrazol complications as affected by the use of curare. Canadian Medical Association Journal 1942;**47**(4):326
116. EASTON NL, SOMMERS J. The significance of vertebral fractures as a complication of metrazol therapy. American Journal of Psychiatry 1942;**98**(4):538-43
117. Graves C, Pignataro F. Injuries sustained during the course of metrazol shock therapy. Psychiatric Quarterly 1940;**14**(1):128-34
118. Krause GR, Langsam CL. Fractures of the vertebrae following metrazol therapy. Radiology 1941;**36**(6):725-30
119. Lingley JR, Robbins LL. Fractures following electroshock therapy. Radiology 1947;**48**(2):124-28
120. NEWBURY CL, ETTER LE. Clarification of the problem of vertebral fractures from convulsive therapy: I. Incidence. AMA Archives of Neurology & Psychiatry 1955;**74**(5):472-78
121. Pedersen KK, Christiansen C, Ahlgren P, Lund M. Incidence of fractures of the vertebral spine in epileptic patients. Acta neurologica Scandinavica 1976;**54**(2):200-03

122. Polatin P, Friedman MM, Harris MM, Horwitz WA. VERTEBRAL FRACTURES PRODUCED BY METRAZOL-INDUCED CONVULSIONS: IN THE TREATMENT OF PSYCHIATRIC DISORDERS. *Journal of the American Medical Association* 1939;**112**(17):1684-87
123. POOL CS, MESCHAN I. Fractures of the spine during insulin shock therapy. *AMA Archives of Neurology & Psychiatry* 1952;**67**(6):797-807
124. Schatz I, Konwaler B. Spine injuries following convulsions from metrazol and from idiopathic epilepsy. *The Journal of Nervous and Mental Disease* 1941;**93**(2):169-75
125. Smith L, Hughes J, Hastings D, Alpers B. Electroshock treatment in the psychoses. *American Journal of Psychiatry* 1942;**98**(4):558-61
126. Reed GE, Dancey TE. Compression fractures of the vertebral bodies following induced and "idiopathic" convulsions. *Canadian Medical Association Journal* 1940;**42**(1):38
127. VASCONCELOS D. Compression fractures of the vertebrae during major epileptic seizures. *Epilepsia* 1973;**14**(3):323-28
128. Worthing HJ, Kalinowsky LB. The question of vertebral fractures in convulsive therapy and in epilepsy. *American Journal of Psychiatry* 1942;**98**(4):533-37
129. NCD-RisC. Data Downloads. Secondary Data Downloads 2017. <http://www.ncdrisc.org/data-downloads.html>.
130. Komlos J, Brabec M. The trend of BMI values of US adults by deciles, birth cohorts 1882–1986 stratified by gender and ethnicity. *Economics & Human Biology* 2011;**9**(3):234-50
131. Census USBot. *Historical statistics of the United States, colonial times to 1970*: US Department of Commerce, Bureau of the Census, 1975.

132. Schmidt AL, Paskoff G, Shender BS, Bass CR. Risk of lumbar spine injury from cyclic compressive loading. *Spine* 2012;**37**(26):E1614-E21

133. Abernethy RB, Breneman J, Medlin C, Reinman GL. Weibull analysis handbook: Pratt and Whitney West Palm beach fl Government Products DIV, 1983.

134. Miller D. Pellagra deaths in the United States. *The American Journal of Clinical Nutrition* 1978;**31**(4):558-58

Biography

Courtney A. Cox has her deepest roots in Georgia. She studied biomedical engineering as an undergraduate at Mercer University in Macon, Georgia. During that time, an outreach trip to Vietnam to help fit amputees with a low-cost, universal prosthetic reinforced for Courtney the way that biomedical engineering could help improve the lives of human beings. After graduating with her bachelor's degree summa cum laude in 2011, she began graduate school at Duke University in the Injury Biomechanics Laboratory of Cameron "Dale" Bass, with the goal of helping to find ways to prevent or lessen the impact of traumatic spinal injuries. En route to her PhD at Duke she finished her master's degree in 2015, and authored three peer-reviewed publications as well as numerous conference papers and presentations, listed below. She also received multiple grants and scholarships such as the prestigious Whitaker International Program Summer Grant.

Degrees

PhD, Duke University, Department of Biomedical Engineering, 2020

MS, Duke University, Department of Biomedical Engineering, 2015

BSE, Mercer University, Department of Biomedical Engineering, 2011

Awards

IRCOBI Asia Travel Grant (May 2016)

Whitaker International Program Summer Grant (Summer 2014)

Peer-Reviewed Publications

Wood, G. W., Panzer, M. B., Cox, C. A., & Bass, C. R. (2018). Interspecies scaling in blast pulmonary trauma. *Human Factors and Mechanical Engineering for Defense and Safety*, 2(1), 3.

Dibb AT, Cutcliffe HC, Luck JF, **Cox CA**, Myers BS, Bass CR, Nightingale RW (2014) Proposed Neck Performance Corridors for the Six and Ten Year Old in Frontal Impacts. *Traffic Injury Prevention* 15(4), 386-394.

Dibb, AT, **Cox CA**, Nightingale RW, Luck JF, Cutcliffe HC, Myers BS, Arbogast KB, Seacrist T, Bass CR. (2013) Importance of Muscle Modeling for Biofidelic Pediatric Neck Response in Computational Models. *Traffic Injury Prevention*, 14(sup1), S116-S127.